The Lattice Boltzmann Method for Complex Flows

Tim Reis [1]
Supervised by Professor T.N. Phillips

August 3, 2007

[1]School of Mathematics, Cardiff University, CF24 4AG, United Kingdom

Acknowledgements

I am indebted to my supervisor, Professor Tim Phillips, for his advice, guidance and understanding throughout the course of my studies - it has been a pleasure to work with you and all your help over the years is very much appreciated. I would like to thank Cardiff University's School of Mathematics for providing a stimulating and enjoyable academic environment, particularly the fluids group for their many helpful discussions. Thanks go to Professor Care, Doctor Bollada and Doctor Davidson for agreeing to examine this thesis. I am also grateful for the useful suggestions I have received from the members of the lattice Boltzmann mailing list. Finally, I would like to express my sincere love and gratitude to my family for their continuing support and encouragement - I don't tell you often enough how important you are.

Declaration

This work has not previously been accepted in substance for any degree and is not concurrently submitted in candidature for any degree.

Signed..... Date.....

Statement 1

This thesis is being submitted in partial fulfillment of the requirements for the degree of PhD.

Signed..... Date.....

Statement 2

This thesis is the result of my own independent work/investigation, except where otherwise stated. Other sources are acknowledged by explicit references.

Signed..... Date.....

Statement 3

I hereby give consent for my thesis, if accepted, to be available for photocopying and for inter-library loan, and for the title and summary to be made available to outside organisations.

Signed..... Date.....

Statement 4

I hereby give consent for my thesis, if accepted, to be available for photocopying and for inter-library loans after expiry of a bar on access approved by the Graduate Development Committee.

Signed..... Date.....

Abstract

This thesis presents the extension of the lattice Boltzmann equation (LBE) to several well-known flows. First, the flow over a cylinder is studied using the LBE and the numerical predictions are shown to compare well with those obtained using a stylised finite volume method. A clear and formal perturbation analysis of the generalised LBE is also presented. A LBE for axisymmetric flows is developed, the precise form of which is derived through a Chapman-Enskog analysis so that the additional axisymmetric contributions to the Navier-Stokes equation are furnished when written in the cylindrical polar coordinate system. Stokes' flow over a sphere is studied and excellent agreement is found between the numerical and analytical predictions. A lattice Boltzmann model for immiscible binary fluids with variable viscosities and density ratio is developed. In the macroscopic limit this model is shown to recover the Navier-Stokes equations for two phase flow. A theoretical expression for surface tension is determined. The validity of this analysis is confirmed by comparing numerical and theoretical predictions of surface tension as a function of density. A number of numerical simulations are presented and shown to be in good agreement with analytical results. Finally, an axisymmetric multiphase lattice Boltzmann model has been proposed. This model is easy to implement and some test cases have been performed to demonstrate its capabilities. A review of the extension of the lattice Boltzmann equation to viscoelasticity is also presented.

Contents

List of Figures

List of Tables

Chapter 1

Introduction

The lattice Boltzmann method (LBM) is an efficient, parallel algorithm for simulating single and multi-phase fluid flows. Unlike conventional numerical schemes based on the discretisation of macroscopic continuum equations, the LBM is a discrete kinetic theory approach that features a mesoscale description of the microstructure of the fluid.

The fundamental philosophy of the LBM is to construct simplified kinetic type models that preserve the conservation laws and necessary symmetries so that the macroscopic averaged properties obey the desired continuum equations of motion. These simplified models are sufficient since it is known that the macroscopic dynamics are not sensitive to the underlying details of microscopic physics. This thesis intends to discuss the theory of the lattice Boltzmann equation and analyse its extension to complex hydrodynamics.

1.1 Modelling Fluid Flow

A fluid is a collection of particles that move freely among themselves. To describe the fluid mathematically, one could model the motion of individual particles and their interactions, or alternatively consider the ensemble of particles and assume the fluid can be modelled as a smoothly varying continuum. Both levels of description have an associated characteristic length scale. At the macroscopic level there may be a number of such lengths; for example

the width of a channel or the diameter of cylinder, denoted by L_1 and L_2 in Figure 1.1, respectively. These are examples of geometric lengths but more intrinsic flow properties, such as the size of vortex shedding in turbulence, may also be considered. The smallest of these hydrodynamic length scales will be denoted by L_H. At the particle, or microscopic level, the characteristic length scale is generally taken to be the mean free path, L_{mfp}, i.e. the average distance particles travel between collisions. A basic hypothesis underlying continuum fluid mechanics is that the macroscopic description holds whenever $L_H \gg L_{mfp}$, or alternatively

$$\epsilon = L_{mfp}/L_H \ll 1, \tag{1.1}$$

where ϵ is referred to as the Knudsen number.

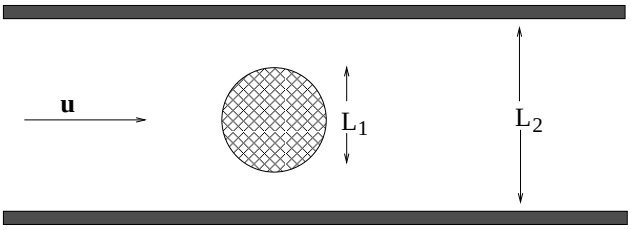

Figure 1.1: Examples of characteristic length scales in the continuum approach.

Consider a collection of N particles of mass m moving in a volume V at time t, each with position vector $\mathbf{x}_i, \quad i = 1 \ldots N$. Let them move freely under the influence of a force $\mathbf{F}_i$. The particles are described by the two Hamiltonian equations of motion:

$$\frac{d\mathbf{x}_i}{dt} = \frac{\mathbf{j}_i}{m}, \tag{1.2}$$

$$\frac{d\mathbf{j}_i}{dt} = \mathbf{F}_i \tag{1.3}$$

where $\mathbf{j}_i$ is the momentum of particle i. If initial conditions and boundary conditions are specified, the two Hamiltonian equations can, in principle, be solved in time to give full knowledge of the state of the system. However,

since the number of particles N in V is exceptionally large (generally of the order of the Avogrado number, $A_v \sim 10^{23}$), this is an infeasible task.

The macroscopic approach does not consider the internal structure of V but instead considers it to be an arbitrary material volume fixed in space with a mass ρ and momentum $\rho\mathbf{u}$, which are assumed to satisfy the conservation laws of Newtonian mechanics, i.e.

$$\frac{\partial}{\partial t}\int_V \rho dV = 0, \tag{1.4}$$

$$\frac{\partial}{\partial t}\int_V \rho\mathbf{u} dV = \int_S \mathbf{n}\cdot\boldsymbol{\sigma} dS + \int_V \rho\mathbf{b} dV, \tag{1.5}$$

where $\boldsymbol{\sigma}$ is a stress tensor, S is a surface element with outward normal $\mathbf{n}$ and $\mathbf{b}$ is a body force. Application of the divergence and Reynolds transport theorems to equations (1.4) and (1.5) yields, upon the assuming all integrands are continuous and the fluid is incompressible, the macroscopic equations of motion for a fluid:

$$\nabla\cdot\mathbf{u} = 0, \tag{1.6}$$

$$\rho\frac{D\mathbf{u}}{Dt} = \nabla\cdot\boldsymbol{\sigma} + \rho\mathbf{b}, \tag{1.7}$$

where

$$\frac{D}{Dt} = \frac{\partial}{\partial t} + \mathbf{u}\cdot\nabla \tag{1.8}$$

is the material derivative. In order to derive an explicit form of the stress tensor we write the components $\sigma_{\alpha\beta}$ of $\boldsymbol{\sigma}$ in the form

$$\sigma_{\alpha\beta} = -P\delta_{\alpha\beta} + T_{\alpha\beta}, \tag{1.9}$$

where $\delta_{\alpha\beta}$ is the Kronecker delta function:

$$\delta_{\alpha\beta} = \begin{cases} 1, & \text{if } \alpha = \beta, \\ 0, & \text{if } \alpha \neq \beta, \end{cases} \tag{1.10}$$

and we define P, the pressure, to be the negative average of the diagonal

stress components, i.e.

$$P = -\frac{1}{3}\sigma_{\alpha\alpha}. \tag{1.11}$$

A constitutive equation is needed to relate the extra stress tensor, $\mathbf{T}$, to the rate of strain, $\dot{\boldsymbol{\gamma}}$. If these two tensors are proportional, i.e.

$$\mathbf{T} = \eta\dot{\boldsymbol{\gamma}}, \tag{1.12}$$

the fluid is said to be Newtonian. The constant of proportionality, η, is known as the viscosity and the rate of strain tensor is defined to be

$$\dot{\boldsymbol{\gamma}} = \nabla\mathbf{u} + (\nabla\mathbf{u})^{\dagger}, \tag{1.13}$$

where $\dagger$ denotes the matrix transpose. With $\mathbf{T}$ defined in (1.12), we obtain the equation of motion for a Newtonian fluid, namely the Navier-Stokes equations:

$$\rho\frac{D\mathbf{u}}{Dt} = -\nabla P + \eta\nabla^2\mathbf{u} + \rho\mathbf{b}, \tag{1.14}$$

$$\nabla\cdot\mathbf{u} = 0. \tag{1.15}$$

In the macroscopic approach, the underlying system is viewed as a smoothly varying continuum, despite the fact that the underlying physical system may be genuinely discrete (containing a fixed number of particles). Therefore, the concept of a continuum is an idealisation, an approximation of the physical reality of fluids. Furthermore, the partial differential equation (1.14) is highly nonlinear and analytic solutions are rarely available. Therefore, numerical solutions become necessary and accurate and efficient algorithms for solving the system of equations are sought.

An intermediate level of description is provided by kinetic theory, which connects the small-scale (L_{mfp}) microscopic picture with the large-scale (L_H) macroscopic properties. Rather that consider individual particles, kinetic theory features a statistical (mesoscopic) description of a fluids microstructure and defines the physical observables (such as density, velocity and temperature) to be averages over a large number of molecular histories. The

primary variable in kinetic theory is not the position of a particle or the macroscopic velocity, but instead the distribution function, f, which contains information regarding the expected number of particles at a position $\mathbf{x}$ with velocity $\boldsymbol{\xi}$ at time t. In 1872, Ludwig Boltzmann derived an equation to describe the evolution of this distribution function in terms of micro-dynamic interactions, which reads:

$$\partial_t f + \boldsymbol{\xi} \cdot \nabla f = C(f) \tag{1.16}$$

where $f = f(\mathbf{x}, \boldsymbol{\xi}, t)$ is the single particle distribution function, $\boldsymbol{\xi}$ is the microscopic velocity, and $C(f)$ is a collision operator. The right-hand side of equation (1.16) is often chosen to be the Bhatnagar-Gross-Krook (BGK) operator:

$$C(f) = -\frac{1}{\lambda}(f - f^{(e)}), \tag{1.17}$$

which represents a simplified description of a particles relaxation to a local equilibrium state due to collisions. In equation (1.17), λ is the relaxation time due to collisions and $f^{(e)}$ is the Boltzmann-Maxwellian distribution function:

$$f^{(e)} = \frac{\rho}{(2\pi RT)^{D/2}} \exp\left(-\frac{(\xi - \mathbf{u})^2}{2RT}\right), \tag{1.18}$$

where R is the ideal gas constant, D is the dimension of space, and ρ, $\mathbf{u}$ and T are the macroscopic density, velocity and temperature, respectively. In the derivation of equation (1.16), Boltzmann assumes that particles entering collisions are uncorrelated. The macroscopic observables are defined by the moments of the distribution function:

$$m \int f d\boldsymbol{\xi} = \rho, \tag{1.19}$$

$$m \int f \boldsymbol{\xi} d\boldsymbol{\xi} = \rho \mathbf{u}, \tag{1.20}$$

$$m \int f \boldsymbol{\xi}^2 d\boldsymbol{\xi} = 2\rho e, \tag{1.21}$$

where e is the energy.

The link between kinetic theory and hydrodynamics is provided by the Chapman-Enskog analysis, which separates the different spacial and temporal scales within a fluid. If the hydrodynamic assumption (1.1) holds, the distribution function can be expanded as

$$f = f^{(0)} + \epsilon f^{(1)} + \epsilon^2 f^{(2)} + \ldots, \tag{1.22}$$

and the space and time variables as

$$\mathbf{x} = \epsilon^{-1}\mathbf{x}_1 + \ldots, \quad t = \epsilon^{-1}t_1, \tag{1.23}$$

where $f^{(0)} = f^{(e)}$, $\mathbf{x}_1$ and t_1 describe the linear (sound wave) regime, and t_2 describes the change in long-term (viscous) dynamics. The end result of this Chapman-Enskog analysis on Boltzmann's equation (1.16) is the Navier-Stokes equations (1.14) and (1.15).

1.2 CFD, LGCA and LBE

The primary task of a mathematical modeller is to construct models that are able to predict phenomena which are observed in the laboratory or the physical world. The level of sophistication of the model is dictated by the analytical and numerical techniques (not to mention computational resources) at the disposal of the modeller. The tension between the level of sophistication of a model and its analytical or computational tractability is particularly strong in fluid dynamics where the quest is to derive a model that is as simple as possible, involving the minimum number of parameters, and yet which has the capability to predict the behaviour of the flow. Traditionally, most of the effort expended in the field of computational fluid dynamics (CFD) has been directed at pursuing a macroscopic approach to numerical predictions, that is solving the system of partial differential equations (1.6) and (1.7) using either finite difference, finite volume or finite element methods (which are local methods) or spectral elements (a global method). In many situations this approach is sufficient to provide a qualitative description of the impor-

tant flow phenomena. However, numerical approximations to these equations can sometimes prove difficult to obtain. For example, there may be truncation errors and numerical instabilities due to the necessary discretisation process, irregular boundary conditions can be difficult to incorporate (particularly with the finite difference method), a Poisson solver is often required for the pressure term, unresolved theoretical problems concerning compatibility conditions to ensure a well-posed discrete problem (finite and spectral element methods), and the nonlinearity can make the discrete system computationally intensive. Extra difficulties arise when simulating multi-phase flows since the interface that exists between two fluids has to be tracked in time - a computationally demanding task that is not easily accomplished by continuum-based methods. If the fluid is non-Newtonian and has a complex constitutive equation for the stress which includes a polymeric contribution $\mathbf{T}$, care must be taken to avoid additional numerical instabilities and spurious oscillations when dealing with the convective term, $\mathbf{u} \cdot \nabla \mathbf{T}$. Furthermore, situations arise in which the predictions using these models fail to give quantitative agreement with experimental measurements and observations. Therefore, given the increased computational resources available today, finer levels of description that can incorporate more sophisticated physics can be contemplated.

The lattice gas cellular automaton (LGCA) and the lattice Boltzmann equation (LBE) are discrete kinetic models for simulating hydrodynamics. These approaches are radically different from traditional CFD techniques since they abandon the concept of the continuum. The LGCA can be viewed as a vastly simplified description of molecular dynamics with a limited number of particle velocities. The development of the model was motivated by the fact that large scale macroscopic properties are not particularly sensitive to the underlying particle motion. Although the LGCA neglects the fine details of microscopic physics, it is nonetheless sufficiently detailed to mimic the correct generic macroscopic behaviour. Since the primary goal of kinetic theory is to derive macroscopic equations from microscopic dynamics by means of statistics, an alternative kinetic approach to CFD would feature a mesoscopic description of the fluid's microstructure. This motivated the

development of the lattice Boltzmann equation, which can either be viewed as a statistical adaptation of the LGCA or a direct discretisation of equation (1.16), and this equation is the focus of this thesis.

The lattice Boltzmann equation can be classified as an explicit, Langrangian, finite-hyperbolic approximation to the Navier-Stokes equation that has been derived within the framework of statistical mechanics. As a numerical tool for fluid mechanics it offers a number of interesting properties that are potentially advantageous compared to its continuum rivals. These include a linear streaming operator, unconditional linear stability, geometric flexibility, a simple and efficient algorithm, and being fully local in space and time allowing for very powerful parallel processing. With reference to multi-phase flows, the moving boundary between fluids should emerge spontaneously from the underlying particle dynamics, which is physically more realistic and computationally less intensive than the tracking procedures used by continuum models. The particle nature also allows the modeller to incorporate sophisticated statistical physics relatively simply into the LBE framework. This is particularly useful for the simulation of viscoelastic fluids since modern theoretical rheology is often concerned with finding constitutive equations for the stress based on the fluid's microstructure.

1.3 Thesis Outline

The purpose of Chapter 2 is to gently introduce the fundamental principles of the LGCA that are also relevant to the development of the LBE, particularly the 'stream-and-collide' algorithm, averaged macrodynamics and the importance of symmetry and the equilibrium function. This is achieved by considering two different models, namely the HPP and FHP lattice.

Chapter 3 develops a more general description of the LGCA microdynamics which is then used in Chapter 4 to describe the equilibrium statistical mechanics of the lattice gas. It is shown that the LGCA converges to an equilibrium solution and that this solution satisfies a Fermi-Dirac distribution function.

The lattice Boltzmann equation and its historical development, including

the derivation of the Navier-Stokes equations, are presented in Chapter 5. We then discuss a perturbation analysis for the LBE dispersion equation and show how to obtain the desired transport coefficients. A journal article to describe this approach has been submitted for publication [51]. A review of different boundary condition treatments is given and their validity is confirmed with laminar Poiseuille flow. Flow over a cylinder is also studied and a large data set is obtained and compared with existing results. A journal article containing this material is currently in preparation [52].

An axisymmetric LBE is developed in Chapter 6 and shown to recover the correct equations of motion in the macroscopic limit. Some benchmark simulations are presented and compared with analytical results. A journal article containing the theoretical developments of the model has been published in Physical Review E [55] and a separate article on the numerical evaluation of the model is being prepared for publication [53].

Chapter 7 reviews existing lattice Boltzmann equations for multi-phase flows and develops a model that can approximate the desired continuum equations of motion. The theoretical aspects of the model are discussed and a number of simulations are performed. This work has been published in Journal of Physics A: Mathematical and Theoretical [54].

Finally, Chapter 8 discusses the extension of the LBE to viscoelastic flows and reviews the current models. Concluding remarks are made in Chapter 9.

Chapter 2

The Lattice Gas Cellular Automaton

In 1973 Hardy, de Pazzis and Pomeau [20] constructed a discrete and massively simplified representation of the molecular motion in a fluid and created the first generation of lattice gas cellular automaton (LGCA). Unfortunately, this model (which was christened HPP after the authors initials) cannot recover the correct equations of motion (neither Euler nor Navier-Stokes) for fluid flow and thus is not considered to be a valid numerical tool for such problems. However, in 1986 Frisch, Hasslacher and Pomeau [12] showed that a similar microscopic model with a different discretisation of phase space could in fact reproduce the desired hydrodynamic equations on a macroscopic level. This *FHP* cellular automaton was greeted with much enthusiasm in the CFD community and spawned a great deal of interest and research. Since 1986 the FHP model has evolved to encompass simulations involving complex boundaries and/or multi-component fluids [39, 58], has become just one member of a whole family of possible phase-space discretisations consistent with the hydrodynamic laws of isotropy [67] and has even inspired the development of another independent numerical tool, namely the Lattice Boltzmann Method (LBM) [9]. In this chapter we introduce the lattice gas cellular automaton via the HPP and FHP models before showing its relationship to equilibrium statistical mechanics and hydrodynamics. The Lattice Boltzmann Method

is discussed in Chapter 5.

2.1 The HPP Model

Consider a regular square lattice such that each lattice site $\mathbf{r}$ is connected to its four nearest neighbours by the lattice link vectors $\mathbf{c}_i, \quad i = 1, 2, 3, 4$. This configuration is known as the HPP lattice and an illustration is given in Figure. 2.1. The *particles* of a simple fluid live on this rectangular domain

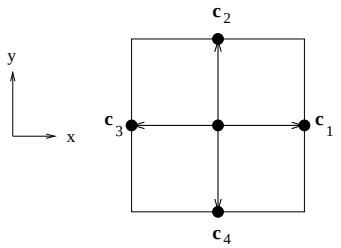

Figure 2.1: The HPP lattice.

and their motion is dictated by a simple two-step process. Particles that enter the same node interact and change their momentum according to a set of pre-determined collision rules. Each particle then hops to the one of its nearest neighbours according to its new momentum. This two-fold evolution of collision and propagation occurs in one single discrete time step Δt, which is usually set to unity. The lattice velocities and lattice link vectors thus have different dimensions but the same numerical value. It is assumed that all particles have unit mass and we exclude the possibility of two or more *indistinguishable* particles travelling along a lattice link at any given time.

It is convenient to define the *occupation variables* $n_i(\mathbf{r}, t)$ to indicate the number of particles moving from node $\mathbf{r}$ to node $\mathbf{r} + \mathbf{c}_i$ at time t. The LGCA evolution can now be described by the equation

$$n_i(\mathbf{r} + \mathbf{c}_i, t + 1) - n_i(\mathbf{r}, t) = \Omega_i(\mathbf{n}), \tag{2.1}$$

where Ω_i is the collision operator that acts on all particles $\mathbf{n} = (n_1, n_2, n_3, n_4)$

entering node $\mathbf{r}$. The collision operator Ω_i must conserve mass, i.e.

$$\sum_i \Omega_i = 0, \tag{2.2}$$

and momentum, i.e.

$$\sum_i \Omega_i \mathbf{c}_i = 0. \tag{2.3}$$

The only particle configurations that alter due to collisions are shown in Figure 2.2 and the collision operator is defined by

$$\Omega_i(\mathbf{n}) = \bar{n}_i \bar{n}_{i+2} n_{i-1} n_{i+1} - n_i n_{i+2} \bar{n}_{i-1} \bar{n}_{i+1}, \tag{2.4}$$

where $\bar{n}_j = 1 - n_j$.

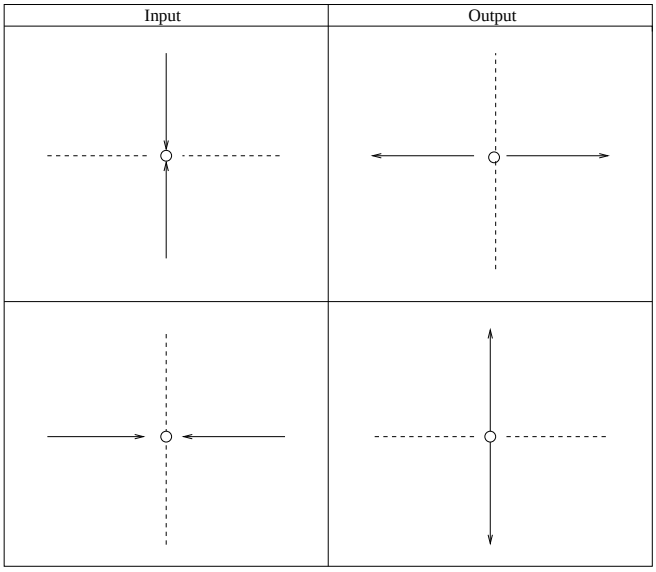

Figure 2.2: The collision rules for the HPP model. Dashed lines represent empty links.

2.2 Coarse Graining

Central to the development of macroscopic quantities in LGCA theory are the mean occupation numbers $N_i, \quad i = 1, 2, 3, 4$. They represent the probability of finding a particle at a given node with velocity in the direction of $\mathbf{c}_i$ and, in lattice gas simulations, they are calculated by averaging n_i in a suitable manner. In practice it is usually most convenient to average over a sub-domain $\mathbf{x}$ containing j neighbouring nodes:

$$N_i(\mathbf{x}, t) = \langle n_i(\mathbf{r}_j, t) \rangle \, . \tag{2.5}$$

The region in which this spatial averaging takes place must be small compared to a typical macroscopic length scale of the flow. Other forms of averaging such as time and ensemble averaging may also be used (ensemble averaging is particularly important in theoretical developments) but this is often restricted by computational performance. The mean occupation numbers are used to calculate the (coarse grained average) macroscopic density (which is a scalar), momentum (a vector) and momentum flux tensor which are defined respectively by

$$\rho(\mathbf{x}, t) = \sum_{i=1}^{4} N_i(\mathbf{x}, t), \tag{2.6}$$

$$\rho u_\alpha(\mathbf{x}, t) = \sum_{i=1}^{4} N_i(\mathbf{x}, t) c_{i\alpha}, \tag{2.7}$$

$$\Pi_{\alpha\beta}(\mathbf{x}, t) = \sum_{i=1}^{4} N_i(\mathbf{x}, t) c_{i\alpha} c_{i\beta} \tag{2.8}$$

where u_α is the α component of velocity. In the above equations, and throughout this thesis, Greek indices assign the Cartesian components of a tensor and, unless otherwise stated, Einstein's summation convention over repeated Greek indices should be assumed.

2.2.1 Equilibrium Distribution and the Equations of Motion

The theoretical development of a homogeneous equilibrium distribution on a lattice will be addressed in Chapter 4. Here however we will just assume that repeated applications of collision and propagation force the averaged occupation variables to reach an equilibrium state, regardless of the initial conditions. By means of a simple series expansion of the equilibrium function $N_i^{(e)}$ in $u = |\mathbf{u}|$, which is assumed to be small, and then exploiting the conservation laws (2.6) and (2.7) and lattice symmetries:

$$\sum_{i=1}^{4} c_{i\alpha} = 0, \tag{2.9}$$

$$\sum_{i=1}^{4} c_{i\alpha} c_{i\beta} = 2\delta_{\alpha\beta}, \tag{2.10}$$

where $\delta_{\alpha\beta}$ is the Kronecker delta function:

$$\delta_{\alpha\beta} = \begin{cases} 1 & \text{if } \alpha = \beta \\ 0 & \text{if } \alpha \neq \beta, \end{cases} \tag{2.11}$$

the equilibrium function $N_i^{(e)}$ for the HPP model is found (to second order) to be [50]

$$N_i^{(e)} = g\left[1 + 2u_\alpha c_{i\alpha} + 2\frac{1-2g}{1-g}\left(c_{i\alpha}c_{i\beta} - \frac{1}{2}\delta_{\alpha\beta}\right)u_\alpha u_\beta\right], \tag{2.12}$$

where $g = \rho/4$ is the density per link.

The hydrodynamic equations of motion can be obtained via a Chapman-Enskog expansion of the distribution functions and this multi-scale analysis is the subject of later chapters. Here we will just state that such a procedure produces the following form of the inviscid Euler equation [50]:

$$\partial_t(\rho u_\alpha) + \partial_x(\Pi_{\alpha\beta}) = 0, \tag{2.13}$$

where

$$\Pi_{\alpha\beta} \begin{cases} 2g\left[1+\frac{1-2g}{1-g}\left(2u_\alpha - u^2\right)\right], & \text{if } \alpha = \beta \\ 0 & \text{otherwise} \end{cases} \tag{2.14}$$

is the momentum flux tensor. We have introduced the shorthand notation for derivatives $\partial_{(\cdot)} = \frac{\partial}{\partial(\cdot)}$ which will be used throughout this thesis.

A tensor is said to be isotropic if its components remain unchanged under an arbitrary change of basis. We will see in Section 5.2 that lattice gas and lattice Boltzmann models require fourth-order isotropy to ensure the correct form of the momentum flux tensor, i.e:

$$\Pi_{\alpha\beta} = f u_\alpha u_\beta + g\delta_{\alpha\beta}, \tag{2.15}$$

where f and g are functions. Clearly equation (2.14) is not isotropic[1] and it should be stressed that this cannot be fixed by going to finer space-time resolutions.

2.3 The FHP Model

The FHP model was proposed in 1986 and its founders showed that their configuration can yield the correct Euler and Navier-Stokes equations in the macroscopic limit. The seminal paper by Frisch, Hasslacher and Pomeau [12] marks the true genesis of lattice models for problems in fluid dynamics[2].

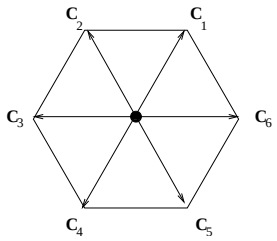

Figure 2.3: The FHP lattice.

[1] An expression for the viscous Navier-Stokes equation on the HPP lattice can also be shown to be plagued by this lack of isotropy [58].

[2] The theoretical foundations of the hexagonal lattice were developed independently by Wolfram [68]

The FHP lattice, which is shown in Figure 2.3, has hexagonal symmetry and associated with each node are the 6 six link vectors defined by

$$\mathbf{c}_i = \left(\cos \frac{i\pi}{3}, \sin \frac{i\pi}{3} \right), \quad i = 1, \ldots, 6, \tag{2.16}$$

and $|\mathbf{c}_i| = 1$ for all i. The FHP propagation phase proceeds in the same way as for the HPP model but the collision phase, which was totally deterministic on the HPP lattice, is now a partially stochastic process. Indeed, a head-on two body collision will rotate the incoming particles by either $+\left(\frac{\pi}{3}\right)$ or $-\left(\frac{\pi}{3}\right)$ with probabilities p and $1-p$, respectively. Frisch et al. [12] also introduced the possibility of deterministic collisions involving three particles and the set of all collisions that scatter momentum, excluding those that can be easily obtained by rotational transformations, is illustrated in Figure 2.4.

Since its introduction the FHP model has evolved to incorporate more elaborate collision rules involving rest particles and 4-way impacts. With the same assumptions used in the HPP model above, the FHP evolution equation can be written in the same general form as equation (2.1) with the collision operator now defined to be

$$\begin{aligned} \Omega_i(\mathbf{n}) \;=\; & n_{i+1} n_{i+3} n_{i+5} \bar{n}_i \bar{n}_{i+2} \bar{n}_{i+4} \\ & - n_i n_{i+2} n_{i+4} \bar{n}_{i+1} \bar{n}_{i+3} \bar{n}_{i+5} \\ & + \xi n_{i+1} n_{i+4} \bar{n}_i \bar{n}_{i+2} \bar{n}_{i+3} \bar{n}_{i+5} \\ & + \bar{\xi} n_{i+2} n_{i+5} \bar{n}_i \bar{n}_{i+1} \bar{n}_{i+3} \bar{n}_{i+4} \\ & - n_i n_{i+3} \bar{n}_{i+1} \bar{n}_{i+2} \bar{n}_{i+4} \bar{n}_{i+4}, \end{aligned} \tag{2.17}$$

where $\mathbf{n} = \{n_i : i = 1, \ldots, 6\}$ and $\xi(\mathbf{x}, t)$ denotes a Boolean random variable equal to one with probability p ($1-p$ for $\bar{\xi}$).

2.3.1 Macrodynamics on the Hexagonal Lattice

The equilibrium function $N_i^{(e)}$ for the FHP model is of the same form as that of the HPP model (equation (2.12)) but the density per link is now

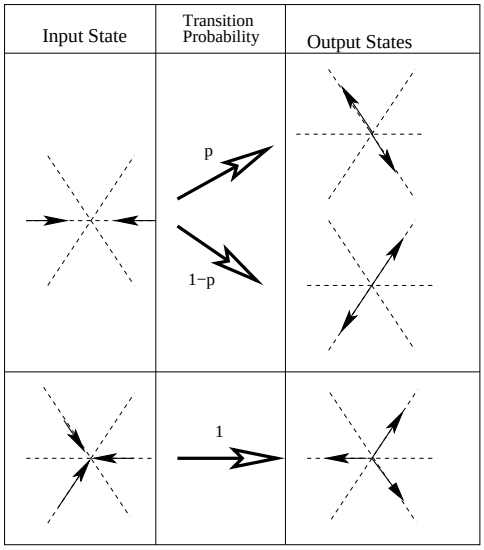

Figure 2.4: The collision rules on the FHP lattice. The numbers on the open arrows are the transition probabilities. The most common choice for p is $1/2$.

$g = \rho/6$ with the index i running from 1 to 6. The full derivation of the hydrodynamic equations for LGCA models mimics the procedure described in Chapter 5 for lattice Boltzmann models and it can be shown [56] that the FHP lattice gas, and indeed many other lattice gas models, can give rise to the full equations of motion for a real isotropic fluid. To understand the failure of the HPP model and the success of the FHP we need to examine lattice symmetry groups, and this subject is addressed in Section 5.2.1.

Chapter 3

LGCA Microdynamics

We now develop a general description of the LGCA microdynamics. This will allow us to determine the instantaneous state of a system and, provided the underlying lattice is sufficiently symmetric, the general lattice gas hydrodynamics.

3.1 Cellular Automata

Automata are systems with a finite set Q of discrete states that evolve deterministically from one state $s \in Q$ to another at each discrete time step Δt [58]. Thus, there exists a functional $\mathcal{F}$ such that

$$s(t + \Delta t) = \mathcal{F}\left[s(t)\right]. \tag{3.1}$$

The time step Δt is usually set to 1 and the automaton is invertible if $\mathcal{F}$ is invertible.

A cellular automaton (CA) is a set of synchronised identical finite automata with identical update rules. The automata act in cells which can be imagined to be positioned at the integer points in the D-dimensional space $\mathbb{Z}^D$. The local state of a cell at $\mathbf{r} = (i, j, k, \ldots)$ depends only on a prescribed local neighbourhood $V_{\mathbf{r}} \subset \mathbb{Z}^D$. There is no notion of distance or angle between cells in a cellular automaton.

3.2 Lattice Gas Cellular Automata

A lattice gas cellular automaton (LGCA) can be viewed as a special case of CA that has a definite geometrical structure and evolves according to a more physical two-step process of propagation and collision. The automata are fixed to the nodes of a D-dimensional lattice $\mathcal{L} \subset \mathbb{R}^D$ which are labelled by a position vector $\mathbf{r}$. Each node $\mathbf{r}$ has m nearest neighbours $\mathbf{r}_k \in V_{\mathbf{r}}$, $k = 1, \ldots, m$. There exists a finite set $\mathcal{I}$ of possible *particle* cells at each node. A mapping $\mathbf{c} : \mathcal{I} \to \mathcal{L}$ associates a velocity vector $\mathbf{c}_i$ with values in a lattice neighbourhood $V_{\mathbf{r}}$ of the origin to each particle cell $i \in \mathcal{I}$. The exclusion principle allows at most one particle per cell at any given node. Therefore, we define an *occupation variable* $n_i(\mathbf{r}, t) \in Q = \{0, 1\}$ to indicate the presence or absence of a particle in i at node $\mathbf{r}$ and time t.

We denote the local state of a node by the $|\mathcal{I}|$ bit word[1]

$$\mathbf{s}(\mathbf{r}) = \{s_i : i \in \mathcal{I}\} \in Q^{\mathcal{I}} \tag{3.2}$$

and the set γ of the $2^{|\mathcal{I}|}$ possible states defines the (discrete) local phase space. Similarly, the instantaneous state of an entire lattice consisting of $\mathcal{N}$ nodes is given by the global configuration $\tilde{\mathbf{s}} = \{s_i(\mathbf{r}) : \mathbf{r} \in \mathcal{L}, i \in \mathcal{I}\} \in Q^{\mathcal{L}\times\mathcal{I}}$ and the set Γ of the $2^{\mathcal{N}|\mathcal{I}|}$ possible global states defines the discrete phase space. We also define the Boolean field $\tilde{\mathbf{n}}$ as the function mapping all particle cells of all nodes onto the Boolean set Q, i.e. $\tilde{\mathbf{n}} : \mathcal{L} \times \mathcal{I} \to Q$. The difference between $\tilde{\mathbf{n}}$ and $\tilde{\mathbf{s}}$ should be emphasised. The Boolean field is a generic notion, whereas the Boolean configuration is a particular realisation of $\tilde{\mathbf{n}}$.

3.2.1 Observables

An observable is a physical property that can be deduced from an abstract automaton. It is assumed that the amount of a given observable assigned to a particle cell does not depend on the position of the node (i.e. local and homogeneous) [56]. In (isothermal) lattice gas theory, the most important of

[1]Here $|\mathcal{I}|$ represents the cardinality of $\mathcal{I}$.

these physical properties are the microscopic density

$$\rho(\mathbf{r}, t) = \sum_{i \in \mathcal{I}} n_i(\mathbf{r}, t), \tag{3.3}$$

and the microscopic momentum

$$\mathbf{j}(\mathbf{r}, t) = \sum_{i \in \mathcal{I}} \mathbf{c}_i n_i(\mathbf{r}, t). \tag{3.4}$$

3.2.2 The Microdynamic Equation

The lattice gas evolution operator, $\mathcal{E}$, is a functional mapping of Γ onto itself, i.e. $\mathcal{E} : \Gamma \to \Gamma$. This operator has the form $(\mathcal{E})_i = (\mathcal{S} \circ \mathcal{C})_i$, where $\mathcal{S}$ is the propagation (or streaming) operator and $\mathcal{C}$ is the collision operator.

The propagation operator translates the state of cell i from one node to another according to its velocity:

$$(\mathcal{S}n)_i(\mathbf{r}, t) = n_i(\mathbf{r} + \mathbf{c}_i, t + \Delta t). \tag{3.5}$$

To avoid complications caused by lattice boundaries we assume that $\mathcal{L}$ is periodic.

The collision operator acts locally in space and time to determine the change in the local state due to particle interactions. More specifically, the post-collision state $n'_i(\mathbf{r}, t)$ is determined by

$$n'_i(\mathbf{r}, t) = n_i(\mathbf{r}, t) + \mathcal{C}_i(\mathbf{n}), \tag{3.6}$$

where the closed expression for the collision operator satisfies

$$\mathcal{C}_i(\mathbf{n}) = \sum_{\mathbf{s},\mathbf{s}'} (s'_i - s_i) \xi_{\mathbf{s},\mathbf{s}'} \prod_i n_i^{s_i} \bar{n}_i^{\bar{s}_i}, \tag{3.7}$$

and

$$\xi_{\mathbf{s},\mathbf{s}'} = \begin{cases} 1 & \text{if the transition } s \to s' \text{ is allowed} \\ 0 & \text{otherwise.} \end{cases} \tag{3.8}$$

Lattice gas collision rules usually incorporate some stochastic elements (see for example the FHP model of Section 2.3). Therefore, we introduce the local transition probability $A_c(\mathbf{s} \to \mathbf{s}') = \langle \xi_{\mathbf{s},\mathbf{s}'} \rangle$ to express the probability of state $\mathbf{s}$ being transformed to $\mathbf{s}'$ by collision. We now write

$$\xi_{\mathbf{s},\mathbf{s}'} = \begin{cases} 1 & \text{with probability} A_c(\mathbf{s} \to \mathbf{s}') \\ 0 & \text{with probability } 1 - A_c(\mathbf{s} \to \mathbf{s}'). \end{cases} \tag{3.9}$$

In the deterministic case, $A_c(\mathbf{s} \to \mathbf{s}') = \xi_{\mathbf{s},\mathbf{s}'}$ satisfies a *detailed balance condition*:

$$A_c(\mathbf{s} \to \mathbf{s}') = A_c(\mathbf{s}' \to \mathbf{s}), \quad \forall \mathbf{s}, \mathbf{s}' \in \gamma \tag{3.10}$$

and the evolution operator is invertible. Stochastic LGCA must instead satisfy the weaker *semi-detailed balance condition*, which states that

$$\sum_{\mathbf{s} \in \gamma} A_c(\mathbf{s} \to \mathbf{s}') = \sum_{\mathbf{s} \in \gamma} A_c(\mathbf{s}' \to \mathbf{s}) = 1, \quad \forall \mathbf{s}' \in \gamma, \tag{3.11}$$

where we have used the normalisation condition for probabilities.

The composition of propagation and collision gives the microdynamic equation for LGCA, which is usually written in the following form

$$n_i(\mathbf{r} + \mathbf{c}_i, t + \Delta t) = n_i(\mathbf{r}, t) + \mathcal{C}_i(\mathbf{n}). \tag{3.12}$$

The only restrictions on the collision operator (for isothermal LGCA) are the conservation of mass

$$\sum_{i \in \mathcal{I}} \mathcal{C}_i(\mathbf{n}) = 0, \tag{3.13}$$

and momentum

$$\sum_{i \in \mathcal{I}} \mathbf{c}_i \mathcal{C}_i(\mathbf{n}) = \mathbf{0}. \tag{3.14}$$

The lattice gas also has some additional, spurious invariants which can lead to deviations from the hydrodynamic behavior in the macroscopic limit. Details

of this LGCA 'disease' along with techniques of how to cure it can be found in [56, 58, 67].

Chapter 4

Equilibrium Statistical Mechanics

The connection between the microscopic formulation of a lattice gas and the macroscopic equations of motion is provided by equilibrium statistical mechanics. This kinetic level of description relies on the concept of ensemble averaged variables and in this chapter we examine the foundations of LGCA theory in terms of its ability to predict continuum values via these expected quantities.

4.1 Ensemble Averages

It is necessary to develop a statistical description for lattice gases which will allow us to determine averaged quantities. Although there are many ways of defining an average, for theoretical developments it is convenient to follow Gibbs [25] and consider ensemble averages.

4.2 Markov Chains and the Lattice Gas

The *global* collision transition probability $a_c(\tilde{\mathbf{s}} \rightarrow \tilde{\mathbf{s}}')$ is given by

$$a_c(\tilde{\mathbf{s}} \rightarrow \tilde{\mathbf{s}}') = \prod_{\mathbf{r}\in\mathcal{L}} A_c(\mathbf{s} \rightarrow \mathbf{s}'), \tag{4.1}$$

and should obey

$$0 \leq a_c(\tilde{\mathbf{s}} \rightarrow \tilde{\mathbf{s}}') \leq 1 \quad \text{and} \quad \sum_{\tilde{\mathbf{s}}' \in \Gamma} a_c(\tilde{\mathbf{s}} \rightarrow \tilde{\mathbf{s}}') = 1. \tag{4.2}$$

This function depends only on the current configuration $\tilde{\mathbf{s}}$ at time t and has no memory of any previous states at time $t^- \leq t$. A lattice gas cellular automaton can therefore be thought of as a special type of Markov process, and since the streaming operator $\mathcal{S}$ is totally deterministic and $a_c(\tilde{\mathbf{s}} \rightarrow \tilde{\mathbf{s}}')$ is invariant under time shifts, by using laws of conditional probabilities it can easily be shown that the probability $P(\tilde{\mathbf{s}}, t)$ of observing state $\tilde{\mathbf{s}}$ at time t must satisfy a Chapman-Kolmogorov equation[1]:

$$P(\mathcal{S}\tilde{\mathbf{s}}', t+1) = \sum_{\tilde{\mathbf{s}} \in \Gamma} a_c(\tilde{\mathbf{s}} \rightarrow \tilde{\mathbf{s}}') P(\tilde{\mathbf{s}}, t), \quad \forall \tilde{\mathbf{s}}' \in \Gamma. \tag{4.3}$$

The probability distribution function $P(\tilde{\mathbf{s}}, t)$ may be called a 'macrostate' of the lattice and thought of as a function that associates with each microstate $\tilde{\mathbf{s}} \in \Gamma$ a real number between 0 and 1, that is $P : \Gamma \rightarrow [0, 1]$. Equation (4.3) is often refereed to as the *lattice Liouville equation.*

To proceed further we need some definitions:

Definition 4.2.1. *A state $\tilde{\mathbf{s}} \in \Gamma$ is connected to another state $\tilde{\mathbf{s}}' \in \Gamma$ if there is a sequence $\tilde{\mathbf{s}}_1, \tilde{\mathbf{s}}_2, \ldots, \tilde{\mathbf{s}}_k \in \Gamma$ such that $a_c(\tilde{\mathbf{s}} \rightarrow \tilde{\mathbf{s}}_1) > 0, \quad a_c(\tilde{\mathbf{s}}_1 \rightarrow \tilde{\mathbf{s}}_2) > 0, \ldots, a_c(\tilde{\mathbf{s}}_k \rightarrow \tilde{\mathbf{s}}') > 0$. We write $\tilde{\mathbf{s}} \rightarrow \tilde{\mathbf{s}}'$ when $\tilde{\mathbf{s}}$ is connected to $\tilde{\mathbf{s}}'$.*

Definition 4.2.2. *A state $\tilde{\mathbf{s}} \in \Gamma$ is transient if there exists a state $\tilde{\mathbf{s}}' \in \Gamma$ such that $\tilde{\mathbf{s}} \rightarrow \tilde{\mathbf{s}}'$ but not $\tilde{\mathbf{s}}' \rightarrow \tilde{\mathbf{s}}$. A state that is not transient is said to be persistent.*

Definition 4.2.3. *If $\tilde{\mathbf{s}} \in \Gamma$ is a persistent state the set of all states $\tilde{\mathbf{s}}' \in \Gamma$ connected to $\tilde{\mathbf{s}}$, denoted $Z(\tilde{\mathbf{s}})$, is said to be ergodic.*

Definition 4.2.4. *If $\tilde{\mathbf{s}}$ is the only member of $Z(\tilde{\mathbf{s}})$ it is an equilibrium state*

[1]The general derivation of the Chapman-Kolmogorov equation can be found in [46].

It is not difficult to show [46] that the system will eventually reach a persistent state. The long term solutions are thus restricted to the ergodic components and may be shown to be either steady or aperiodic. Here we consider only the steady solutions. For these an important theorem is the following:

Theorem 4.2.1. *For a single ergodic component there is a unique time independent solution $\pi_{\tilde{\mathbf{s}}}$ of equation (4.3).*

A proof of the above theorem can be found in [46]. Having stated the existence and uniqueness of an equilibrium probability distribution $\pi_{\tilde{\mathbf{s}}}$ over each ergodic set $Z(\tilde{\mathbf{s}})$, we now wish to show that any probability distribution $P(\tilde{\mathbf{s}}, t)$ over $Z(\tilde{\mathbf{s}})$ will approach this steady state as $t \to \infty$. This can be achieved by making use of the mathematical theory of convex functions, which also leads to a H-theorem:

Theorem (H-theorem) 4.2.2. *Let $\phi(y)$ be a convex function and assume the semi-detailed balance condition (equation 3.11) holds. Then the function*

$$H(t) = \sum_{\tilde{\mathbf{s}} \in \Gamma} \phi[P(\tilde{\mathbf{s}}, t)] \tag{4.4}$$

is a non-increasing function of time.

Proof. First note that in symbols Theorem 4.2.2 can be written as

$$\sum_{\tilde{\mathbf{s}} \in \Gamma} \phi(P(\tilde{\mathbf{s}}, t)) \geq \sum_{\tilde{\mathbf{s}}' \in \Gamma} \phi(P(\tilde{\mathbf{s}}', t+1)) = \sum_{\tilde{\mathbf{s}}' \in \Gamma} \phi(P(\mathcal{S}\tilde{\mathbf{s}}', t+1)), \tag{4.5}$$

If $\phi(y)$ is a twice differentiable convex function and m_i is a weight associated with the point y_i, then [46]

$$\sum_i m_i \phi(y_i) \geq \sum_i m_i \phi(\bar{y}), \tag{4.6}$$

where

$$\bar{y} = \frac{\sum_i m_i y_i}{\sum_i m_i}, \tag{4.7}$$

$$m_i \geq 0, \quad \forall i. \tag{4.8}$$

To relate this relationship to our probabilistic lattice gas we take the weights m_i to be the transition probability $a_c(\tilde{\mathbf{s}} \to \tilde{\mathbf{s}}')$ and set the argument in ϕ to be $y = P(\tilde{\mathbf{s}}, t)$. When the index i is replaced by $\tilde{\mathbf{s}}$ and the summation is taken over all states $\tilde{\mathbf{s}}$, equation (4.6) reads:

$$\sum_{\tilde{\mathbf{s}} \in \Gamma} a_c(\tilde{\mathbf{s}} \to \tilde{\mathbf{s}}') \phi(P(\tilde{\mathbf{s}}, t)) \geq \sum_{\tilde{\mathbf{s}} \in \Gamma} a_c(\tilde{\mathbf{s}} \to \tilde{\mathbf{s}}') \phi\left(\frac{\sum_{\tilde{\mathbf{s}} \in \Gamma} a_c(\tilde{\mathbf{s}} \to \tilde{\mathbf{s}}') P(\tilde{\mathbf{s}}, t)}{\sum_{\tilde{\mathbf{s}}} a_c(\tilde{\mathbf{s}} \to \tilde{\mathbf{s}}')} \right). \tag{4.9}$$

By virtue of the normalisation and semi-detailed balance conditions, the above equation yields, after summation over all $\tilde{\mathbf{s}}'$,

$$\sum_{\tilde{\mathbf{s}} \in \Gamma} \phi(P(\tilde{\mathbf{s}}, t)) \geq \sum_{\tilde{\mathbf{s}}' \in \Gamma} \phi\left(\sum_{\tilde{\mathbf{s}} \in \Gamma} a_c(\tilde{\mathbf{s}} \to \tilde{\mathbf{s}}') P(\tilde{\mathbf{s}}, t) \right). \tag{4.10}$$

Furthermore, the right hand side of equation (4.10) is recognised to be the right hand side of the Chapman-Kolmogorov equation (4.3) and therefore

$$\sum_{\tilde{\mathbf{s}} \in \Gamma} \phi(P(\tilde{\mathbf{s}}, t)) \geq \sum_{\tilde{\mathbf{s}}' \in \Gamma} \phi\left(P(\mathcal{S}\tilde{\mathbf{s}}', t+1) \right). \tag{4.11}$$

□

The functional H can be interpreted as the statistical entropy for the lattice gas with $\phi(y) = y \ln y$. The H-theorem implies that the entropy of the system can not decrease under the lattice gas evolution operator.

Theorem 4.2.3. *Assuming a semi-detailed balance condition holds, the long term solution of equation (4.3) is a constant probability over each ergodic component, i.e.*

$$\lim_{t \to \infty} P(\tilde{\mathbf{s}}, t) = \pi_{\tilde{\mathbf{s}}}. \tag{4.12}$$

Proof. We first state that a Taylor expansion of a twice differentiable convex function gives

$$\begin{aligned} \phi(y) &= \phi(y_0) + (y - y_0)\dot{\phi}(y_0) + \frac{1}{2}(y - y_0)^2\ddot{\phi}(y_\theta), && (4.13) \\ &\geq \phi(y_0) + (y - y_0)\dot{\phi}(y_0), && (4.14) \end{aligned}$$

where $\dot{\phi}$ and $\ddot{\phi}$ denote the first and second derivatives, respectively, and y_θ is some number between y_0 and y.

Consider a stationary Markov chain with probability distribution $P(\tilde{\mathbf{s}}, t)$ restricted to a single ergodic set $Z(\tilde{\mathbf{s}})$. Define

$$G(t) = \sum_{\tilde{\mathbf{s}} \in Z} \pi_{\tilde{\mathbf{s}}} \phi\left(\frac{P(\tilde{\mathbf{s}}, t)}{\pi_{\tilde{\mathbf{s}}}}\right), \tag{4.15}$$

where $\pi_{\tilde{\mathbf{s}}}$ is the equilibrium distribution function and ϕ is any strictly convex[2] function. From the definition of convexity in equation (4.6) we obtain the following lower bound for G:

$$G(t) \geq \phi(1), \tag{4.16}$$

the two sides being equal when $\pi_{\tilde{\mathbf{s}}} = P(\tilde{\mathbf{s}})$. The excess of G over its lower bound thus measures the deviation of the probability distribution from the equilibrium state. Now, write

$$\begin{aligned} X &= \frac{P(\tilde{\mathbf{s}}, t)}{\pi_{\tilde{\mathbf{s}}}}, \quad \forall \tilde{\mathbf{s}} \in Z, && (4.17) \\ Y &= \frac{P(\mathcal{S}\tilde{\mathbf{s}}', t+1)}{\pi_{\tilde{\mathbf{s}}'}}, \quad \forall \tilde{\mathbf{s}}' \in Z. && (4.18) \end{aligned}$$

With these definitions the Chapman-Kolmogorov equation (4.3) takes the form

$$Y = \sum_{\tilde{\mathbf{s}}} b(\tilde{\mathbf{s}} \to \tilde{\mathbf{s}}')X, \tag{4.19}$$

[2] $\phi(y)$ is strictly convex if $\ddot{\phi}(y_\theta) > 0$.

where

$$b(\tilde{\mathbf{s}} \to \tilde{\mathbf{s}}') = \frac{a_c(\tilde{\mathbf{s}} \to \tilde{\mathbf{s}}')\pi_{\tilde{\mathbf{s}}}}{\pi_{\tilde{\mathbf{s}}'}}, \tag{4.20}$$

and satisfies

$$\sum_{\tilde{\mathbf{s}}'} \pi_{\tilde{\mathbf{s}}'} b(\tilde{\mathbf{s}} \to \tilde{\mathbf{s}}') = \pi_{\tilde{\mathbf{s}}}, \tag{4.21}$$

$$\sum_{\tilde{\mathbf{s}}} b(\tilde{\mathbf{s}} \to \tilde{\mathbf{s}}') = 1. \tag{4.22}$$

With these conditions it is possible to show that [46]

$$G(t) - G(t+1) = \sum_{\tilde{\mathbf{s}}} \sum_{\tilde{\mathbf{s}}'} \pi_{\tilde{\mathbf{s}}'} b(\tilde{\mathbf{s}} \to \tilde{\mathbf{s}}') \left[\phi(X) - \phi(Y) - (X-Y)\dot{\phi}(Y)\right] \geq 0, \tag{4.23}$$

where the last term, which vanishes, is suggested by equation (4.13).

Taking the limit as $t \to \infty$ of both sides of equation (4.23), noting that each term in the sum is non-negative, $\pi_{\tilde{\mathbf{s}}'} > 0$ and applying equation (4.13), we find that

$$\lim_{t\to\infty} b(\tilde{\mathbf{s}} \to \tilde{\mathbf{s}}') \left[\frac{1}{2}(X-Y)^2 \ddot{\phi}(W)\right] = 0, \tag{4.24}$$

where W is a number between X and Y. The strict convexity of ϕ implies that $\ddot{\phi}$ has a positive lower bound on any bounded interval. Following the work of Penrose [46], we denote the lower bound for the interval $0 < y < max(1/\pi_{\tilde{\mathbf{s}}'})$ by a and deduce that

$$\frac{a}{2} \lim_{t\to\infty} b(\tilde{\mathbf{s}} \to \tilde{\mathbf{s}}')(X-Y)^2 = 0. \tag{4.25}$$

Since the possibility $b(\tilde{\mathbf{s}} \to \tilde{\mathbf{s}}') = 0$ is not possible we have, after converting back to the original notation,

$$\lim_{t\to\infty} \left[\frac{P(\tilde{\mathbf{s}}, t)}{\pi_{\tilde{\mathbf{s}}}} - \frac{P(\mathcal{S}\tilde{\mathbf{s}}', t+1)}{\pi_{\tilde{\mathbf{s}}'}}\right] = 0. \tag{4.26}$$

Finally, multiplying the above by $\pi_{\tilde{\mathbf{s}}'}$, summing over $\tilde{\mathbf{s}}'$ and applying the

normalisation condition yields:

$$\lim_{t\to\infty} P(\tilde{\mathbf{s}}, t) = \pi_{\tilde{\mathbf{s}}} \quad \text{if } \tilde{\mathbf{s}} \in Z \tag{4.27}$$

□

4.3 The Fermi-Dirac Equilibrium Function

Now that we have shown that the long term solutions of the Chapman-Kolmogorov equation for LGCA are a constant probability, we look for a general form of the distribution function $\pi_{\tilde{\mathbf{s}}}$. To do this we state the following:

Hypothesis (Ergodic hypothesis) 4.3.1. *The solutions of equation (4.3) converge to a steady distribution which are constant over each energy level. That is, the statistical equilibria must be functions of mass and momentum only:*

$$\pi_{\tilde{\mathbf{s}}} = \mathcal{F}(M_{\tilde{\mathbf{s}}}, \mathbf{G}_{\tilde{\mathbf{s}}}), \tag{4.28}$$

where $M_{\tilde{\mathbf{s}}}$ and $\mathbf{G}_{\tilde{\mathbf{s}}}$ are the global mass on momentum, respectively.

It can be shown [58] that the steady solution $\pi_{\tilde{\mathbf{s}}}$ satisfies a Gibbs distribution of the form

$$\pi_{\tilde{\mathbf{s}}} = \frac{1}{\chi_{\tilde{\zeta}}} \exp\left\{-hM_{\tilde{\mathbf{s}}} - \mathbf{q}\cdot\mathbf{G}_{\tilde{\mathbf{s}}}\right\}, \quad \forall \tilde{\mathbf{s}} \in \Gamma, \tag{4.29}$$

where h and $\mathbf{q}$ are Lagrangian multipliers associated with mass and momentum and $\chi_{\tilde{\zeta}}$ is a normalisation constant. The normalisation condition $\sum_{\tilde{\mathbf{s}}} \pi_{\tilde{\mathbf{s}}} = 1$ is satisfied when

$$\chi_{\tilde{\zeta}} = \sum_{\tilde{\zeta}\in\Gamma} \exp\left\{-hM_{\tilde{\zeta}} - \mathbf{q}\cdot\mathbf{G}_{\tilde{\zeta}}\right\} \tag{4.30}$$

Equation (4.29) can be factorised over lattice nodes to give

$$\pi_{\tilde{\mathbf{s}}} = \prod_{\mathbf{r}\in\mathcal{L}} \pi_{\mathbf{s}(\mathbf{r})}, \tag{4.31}$$

where

$$\pi_{\mathbf{s}} = \frac{1}{\chi_\zeta} \exp\{-hm_{\mathbf{s}} - \mathbf{q}\cdot\mathbf{g}_{\mathbf{s}}\}, \quad \forall \mathbf{s} \in \gamma \tag{4.32}$$

In the above, $m_{\mathbf{s}}$ and $\mathbf{g}_{\mathbf{s}}$ are local mass and momentum pockets and χ_ζ is a normalisation constant satisfying

$$\chi_\zeta = \sum_{\zeta\in\gamma} \exp\{-hm_\zeta - \mathbf{q}\cdot\mathbf{g}_\zeta\}\,. \tag{4.33}$$

Further factorising over individual bits gives, on fulfilment of the normalisation condition,

$$\pi_{\mathbf{s}} = \prod_{i\in\mathcal{I}} \pi_i, \tag{4.34}$$

where

$$\pi_i(n_i) = \frac{\exp\{-hn_i - n_i\mathbf{q}\cdot\mathbf{c}_i\}}{1+\exp\{-hn_i - n_i\mathbf{q}\cdot\mathbf{c}_i\}}. \tag{4.35}$$

Due to the exclusion principle, n_i is a Boolean variable so averaging the above over the occupation variables yields

$$N_i^{(e)} = \pi_i(1) = \frac{1}{1+\exp\{h+\mathbf{q}\cdot\mathbf{c}_i\}}, \tag{4.36}$$

which is the Fermi-Dirac distribution for LGCA. The derivation of the parameters h and $\mathbf{q}$ can be found in [50].

Theorem 4.3.1. *Assuming the semi-detailed balance holds, the following three statements are equivalent:*

1. *The N_i's are a solution of equation (4.3);*
2. *The N_i's are a solution of the set of the $|\mathcal{I}|$ equations $\mathcal{C}_i(N) = 0$;*
3. *The N_i's are given by equation (4.36).*

Proof. (1) $\Rightarrow$ (2):

Assume N_i is a solution of to the Chapman-Kolmogorov equation. Equa-

tion (4.3) can be written as

$$\prod_{\mathbf{r}\in\mathcal{L}}\prod_{i\in\mathcal{I}} N_i^{s_i'}(1-N_i)^{(1-s_i')} = \sum_{\tilde{\mathbf{s}}\in\Gamma}\prod_{\mathbf{r}\in\mathcal{L}} a(\tilde{\mathbf{s}}\to\tilde{\mathbf{s}}')\prod_{j\in\mathcal{I}} N_j^{s_j}(1-N_j)^{(1-s_j)}, \tag{4.37}$$

for all $\tilde{\mathbf{s}}' \in \Gamma$ and we state without proof[3] that this is equivalent to

$$\prod_{j\in\mathcal{I}} N_j^{s_j'}(1-N_j)^{(1-s_j')} = \sum_{\mathbf{s}} A_c(\mathbf{s}\to\mathbf{s}')\prod_{j\in\mathcal{I}} N_j^{s_j}(1-N_j)^{(1-s_j)}, \tag{4.38}$$

for all $\mathbf{s}' \in \gamma$. Use the normalisation condition to write the above as

$$\sum_{\mathbf{s}} A_c(\mathbf{s}'\to\mathbf{s})\prod_{j\in\mathcal{I}} N_j^{s_j'}(1-N_j)^{(1-s_j')} = \sum_{\mathbf{s}} A_c(\mathbf{s}\to\mathbf{s}')\prod_{j\in\mathcal{I}} N_j^{s_j}(1-N_j)^{(1-s_j)}, \quad \forall \mathbf{s}' \in \gamma. \tag{4.39}$$

Now multiply both sides by s_i' and sum over $\mathbf{s}'$ to obtain

$$\sum_{\mathbf{s},\mathbf{s}'} s_i' A_c(\mathbf{s}'\to\mathbf{s})\prod_{j\in\mathcal{I}} N_j^{s_j'}(1-N_j)^{(1-s_j')} = \sum_{\mathbf{s},\mathbf{s}'} s_i' A_c(\mathbf{s}\to\mathbf{s}')\prod_{j\in\mathcal{I}} N_j^{s_j}(1-N_j)^{(1-s_j)}, \tag{4.40}$$

for all $\mathbf{s}' \in \gamma$ and $i \in \mathcal{I}$. Noting that $\mathbf{s}$ and $\mathbf{s}'$ on the LHS are dummy variables, rearrange equation (4.40) to show that

$$\sum_{\mathbf{s},\mathbf{s}'} (s_i' - s_i) A_c(\mathbf{s}\to\mathbf{s}')\prod_{j\in\mathcal{I}} N_j^{s_j}(1-N_j)^{(1-s_j)} = 0, \quad \forall i \in \mathcal{I}. \tag{4.41}$$

Therefore, N_i is a solution of $\mathcal{C}_i(N) = 0$.

[3] A proof can be found in [56]

(2) $\Rightarrow$ (3) :

Divide both sides of equation (4.40) by $\prod_{k\in\mathcal{I}}(1-N_k)$ to obtain

$$\sum_{\mathbf{s},\mathbf{s}'}(s_i'-s_i)A_c(\mathbf{s}\to\mathbf{s}')\prod_{j\in\mathcal{I}}\hat{N}_j^{s_j}=0,\quad \forall I\in\mathcal{I}, \tag{4.42}$$

where $\hat{N}_j = N_j/(1-N_j)$. Multiply both sides of the above equation by $\ln\hat{N}_i$ and sum over i to find

$$\sum_{\mathbf{s}',\mathbf{s}}A_c(\mathbf{s}\to\mathbf{s}')\ln\left(\frac{\prod_j\hat{N}_i^{s_i'}}{\prod_j\hat{N}_i^{s_i}}\right)\prod_j\hat{N}_i^{s_i}=0. \tag{4.43}$$

The semi-detailed balance condition allows us to write

$$\sum_{\mathbf{s}',\mathbf{s}}A_c(\mathbf{s}\to\mathbf{s}')\left(\prod_j\hat{N}_j^{s_j'}-\prod_j\hat{N}_j^{s_j}\right)=0, \tag{4.44}$$

and, by adding this expression to the left hand side of equation (4.43), a little algebra and analysis yields [56]

$$\sum_i A_c(\mathbf{s}\to\mathbf{s}')(s_i'-s_i\ln\hat{N}_i)=0,\quad \forall\mathbf{s},\mathbf{s}'\in\gamma. \tag{4.45}$$

This implies that $\ln\hat{N}_i$ is a collision invariant. The set of all collision invariants of a lattice gas model is a vector subspace of $\mathbb{R}^{|\mathcal{I}|}$. Consider a basis $(\mathbf{q}^k : k=1,\ldots)$ of this subspace. Any given collision invariant is a unique linear combination of the form $\sum_k\lambda^k\mathbf{q}^k$. Solving

$$\ln\hat{N}_i=\sum_k\lambda^k\mathbf{q}_i^k,\quad \forall i\in\mathcal{I} \tag{4.46}$$

yields the Fermi-Dirac distribution

$$N_i=\left(1+\exp\left\{\sum_k\lambda^k\mathbf{q}_i^k\right\}\right)^{-1},\quad \forall i\in\mathcal{I} \tag{4.47}$$

and since, by the ergodic hypothesis, mass and momentum are the only

invariants we see that

$$N_i = \frac{1}{1 + \exp\{h + \mathbf{q} \cdot \mathbf{c}_i\}}. \tag{4.48}$$

(3) $\Rightarrow$ (1) :

If N_i satisfies equation (4.36) then the equilibrium probability $\pi_{\tilde{\mathbf{s}}} = \prod_i \prod_{\mathbf{r}} N_i$ satisfies a Gibbs distribution (cf. Section 4.3) which is a solution to equation (4.3). It follows that N_i is a solution of the Chapman-Kolmogorov equation, which completes the proof. □

Chapter 5

Lattice Boltzmann Hydrodynamics

In the previous chapter we introduced the lattice gas cellular automaton and, from a statistical mechanics perspective, discussed its equilibrium properties. In this development the characteristic microscopic scales are the lattice spacing and time-steps but we now wish to describe how the hydrodynamic states (that is, the moments of the distribution function) vary on a macroscopic scale i.e. on space and time scales much larger than the characteristic lattice scales. In this chapter we introduce the lattice Boltzmann equation and show how it can approximate the equations of motion in the hydrodynamic limit. The new contributions to the lattice Boltzmann community given here are the alternative approach to the solution of the dispersion relation for a generalised lattice Boltzmann equation and a detailed study of the influence of the Reynolds number and blockage ratio on the flow over a cylinder. This work is also contained in our journal articles [51] and [52], respectively.

5.1 The Lattice Boltzmann Equation

The lattice Boltzmann model can be viewed as a direct extension of the lattice gas cellular automaton developed to resolve the LGCA shortcomings. The occupation variable n_i is replaced by the average population density

$N_i(\mathbf{x}, t) = \langle n_i(\mathbf{r}, t) \rangle$, thus reducing statistical noise[1]. Taking the (ensemble) average of the LGCA evolution equation (3.12) leads to the (non-linear) lattice Boltzmann equation:

$$N_i(\mathbf{x} + \mathbf{c}_i, t + 1) = N_i(\mathbf{x}, t) + \langle \Omega_i(\mathbf{n}) \rangle. \tag{5.1}$$

As it stands, the right-hand-side of equation (5.1) cannot be expressed in terms of the N_i's. Thus, to obtain a kinetic equation in closed form Boltzmann's assumption that particles entering a collision are uncorrelated is used:

$$N_i(\mathbf{x} + \mathbf{c}_i, t + 1) = N_i(\mathbf{x}, t) + \Omega_i(\mathbf{N}), \tag{5.2}$$

where $\mathbf{N} = [N_1, \ldots N_b]$. In the lattice Boltzmann framework, the macroscopic density and momentum are defined by the zeroth and first moments of the distribution function, respectively:

$$\rho = \sum_i N_i, \tag{5.3}$$

$$\rho \mathbf{u} = \sum_i N_i \mathbf{c}_i. \tag{5.4}$$

Despite overcoming the statistical noise issues, equation (5.2) inherited all other LGCA 'diseases', namely exponential complexity (causing difficulties when extending the model to three dimensions), lack of Galilean invariance (which results from the finite number of speeds available for the Fermi-Dirac distribution) and a relatively high viscosity and therefore low Reynolds number barrier (due to the maximum number of collisions an automaton can support). The next step in the LBE genealogy was completed by Higuera and Jimenez [23] who conquered the exponential complexity limitation by considering perturbations of the local equilibrium function.

The macrostates of the LBM (and indeed LGCA) are functions of the space variable $\mathbf{x}$ and vary slowly in space. Any significant variation takes

[1]This model was first proposed by G. McNamara and G. Zanetti [41]

place over distances much larger than the lattice length scale (i.e. the mesh size). We can then say that the population distribution function departs slightly from the local equilibrium state and write

$$N_i = N_i^{(0)} + \epsilon N_i^{(1)} + \epsilon^2 N_i^{(2)} + \cdots , \tag{5.5}$$

where $N_i^{(0)} = N_i^{(e)}$ is the equilibrium state and the expansion parameter $\epsilon \ll 1$ is the ratio of the microscopic scale to the smallest macroscopic scale. The equilibrium component is required to fulfil the following constraints:

$$\sum_{i=1}^{b} N_i^{(e)} = \rho, \tag{5.6}$$

$$\sum_{i=1}^{b} N_i^{(e)} \mathbf{c}_i = \rho \mathbf{u}. \tag{5.7}$$

Now, inserting this form of N_i into the collision term and expanding in a Taylor series about $N_i^{(0)}$ gives

$$\begin{aligned} \Omega_i(\mathbf{N}) \;\simeq\; & \Omega_i^{(0)} + \epsilon \sum_j \frac{\partial \Omega_i^0}{\partial N_j} N_j^{(1)} \\ & + \frac{\epsilon^2}{2} \sum_{jk} \frac{\partial^2 \Omega_i^0}{\partial N_j \partial N_k} N_j^{(1)} N_k^{(1)}, \end{aligned} \tag{5.8}$$

where the superscript 0 on the collision operator implies evaluation at $N_i = N_i^{(0)}$. This equation can be simplified when we realise that the collision operator in the equilibrium state vanishes i.e. $\Omega_i(\mathbf{N}^{(0)}) = 0$. Also, because of the conservation of momentum, $(\partial \Omega_i^0 / \partial N_j) N_j^{(1)} = 0$. Upon using these two results we obtain the *quasi-linear lattice Boltzmann equation*:

$$N_i(\mathbf{x} + \mathbf{c}_i, t+1) - N_i(\mathbf{x}, t) = \sum_j M_{ij} \left(N_j - N_j^{(e)} \right), \tag{5.9}$$

where

$$M_{ij} = \frac{\partial \Omega_i^0}{\partial N_j}, \tag{5.10}$$

defines the collision matrix which determines the scattering rate between directions i and j. This matrix is isotropic and cyclic since the scattering depends only on the absolute value between the incoming populations. The importance of this procedure is that it reduces the collision term complexity from 2^b to b^2 and then, because of the symmetry of M_{ij}, to order b, thus making it computationally feasible to perform lattice Boltzmann simulations in three dimensions. However, M_{ij} still has a one-to-one correspondence with the underlying LGCA dynamics. This means that the viscosity for the LBE is the same as that for the LGCA, resulting in a relatively strict upper bound on the permitted Reynolds number. This limitation was overcome with the work of Higuera, Succi and Benzi [24] who regarded the quasi-linear LBE as a self-standing mathematical tool for modelling fluid behaviour.

The only restrictions imposed on the self-standing or 'enhanced collisions' lattice Boltzmann equation are the conservation laws of mass and momentum

$$\sum_{i=1}^{b} M_{ij} = 0, \quad \sum_{i=1}^{b} M_{ij}\mathbf{c}_i = 0 \tag{5.11}$$

and the laws of symmetry (cf. Section 5.2). The equilibrium function $N_i^{(e)}$ can also be defined arbitrarily, subject to the above conditions. We again remark that the matrix elements M_{ij} are numerical parameters that can be tuned at will to achieve maximum Reynolds number. These elements are expressed in terms of the non-zero eigenvalues of M_{ij} and the spectral analysis of the scattering matrix yields the mass and momentum quantities (associated with the null eigenvalues) and the momentum flux tensor (associated with the first non-zero eigenvalue) as well as faster decaying kinetic modes. From this the *exact* expression for the fluid viscosity can be obtained. In view of the fact that the momentum flux, which is the slowest non-conserved quantity, needs only the leading non-zero eigenvalue of the collision matrix it is natural to wonder if the lattice Boltzmann model can be simplified yet further by choosing a single parameter scattering matrix. Many authors raised

this point concurrently [61] and defined the *Lattice Bhatnagar Gross Krook* (LBGK) model:

$$N_i(\mathbf{x}+\mathbf{c}_i, t+1) - N_i(\mathbf{x}, t) = \omega \left[N_i^{(e)}(\mathbf{x}, t) - N_i(\mathbf{x}, t) \right], \tag{5.12}$$

where ω, which is the first non-zero eigenvalue of M_{ij}, is a relaxation parameter. This is the simplest and most efficient lattice Boltzmann model at hand that recovers the Navier-Stokes equations and the detailed derivation of this model follows in the next section. We shall return to the multi-relaxation time LBE in Section 5.4.

5.2 Isotropy and the Equilibrium Function

The large scale dynamics of lattice Boltzmann methods depend on the underlying lattice geometry. To ensure the associated macroscopic equations satisfy the required invariance properties a suitably symmetric mesh has to be constructed.

5.2.1 Isotropy

A tensor is said to be *isotropic* if it is invariant under arbitrary rotations and reflections. More formally, a fully symmetric n^{th} order tensor $T^{(n)}$ is isotropic if, and only if, there exists an $a \in \mathbf{R}$ such that

$$\sum_{\alpha_1}^{D} \cdots \sum_{\alpha_n}^{D} T^n_{\alpha_1 \ldots \alpha_n} x_{\alpha_1} \ldots x_{\alpha_n} = a \|\mathbf{x}\|, \quad \forall \mathbf{x} \in \mathbf{R}^D. \tag{5.13}$$

Isotropic tensors associated with a lattice are constructed from the link vectors $\mathbf{c}_i$ by summing over all lattice directions i, weighted by a coefficient W_i:

$$T^{(n)}_{\alpha_1 \cdots \alpha_n} = \sum_{i=1}^{b} W_i c_{i\alpha_1} \cdots c_{i\alpha_n} \tag{5.14}$$

and a lattice Boltzmann model has n^{th} order isotropy if all these tensors

with order less than or equal to n are isotropic. Our aim is to derive the Navier-Stokes equations so we need to consider tensors up to fourth order. Isotropy dictates the following conditions:

$$\sum_i W_i = 1, \tag{5.15}$$

$$\sum_i W_i c_{i\alpha} = 0, \tag{5.16}$$

$$\sum_i W_i c_{i\alpha} c_{i\beta} = \lambda_1 \delta_{\alpha\beta}, \tag{5.17}$$

$$\sum_i W_i c_{i\alpha} c_{i\beta} c_{i\gamma} = 0, \tag{5.18}$$

$$\sum_i W_i c_{i\alpha} c_{i\beta} c_{i\gamma} c_{i\delta} = \lambda_2 \left(\delta_{\alpha\beta}\delta_{\gamma\delta} + \delta_{\alpha\gamma}\delta_{\beta\delta} + \delta_{\alpha\delta}\delta_{\beta\gamma}\right) \tag{5.19}$$

where λ_1 and λ_2 are constants, $\delta_{\alpha\beta}$ is the Kronecker delta function, given by:

$$\delta_{\alpha\beta} = \begin{cases} 1, & \text{if } \alpha = \beta, \\ 0, & \text{if } \alpha \neq \beta, \end{cases} \tag{5.20}$$

and the Greek indices refer to the Cartesian coordinates.

We have already seen in Section 2.2.1 that the four-velocity HPP lattice is not isotropic to fourth order and therefore fails to deliver the Galilean invariant Euler (and also Navier-Stokes) equations. The FHP model of Section 2.3 does not suffer any anisotropy until 6th order, giving it higher hydrodynamic credentials, but some drawbacks are still evident: The FHP model is a single speed lattice and therefore does not have multi-energy levels and its extension to three dimensions is complicated.

5.2.2 The D2Q9 Model

A simple yet sufficiently symmetric and multi-speed lattice is the D2Q9 lattice, shown in Figure 5.1. It is a nine velocity model (including a rest particle at the centre) for which we can derive an equilibrium solution with all the properties needed to recover the macroscopic hydrodynamic equations.

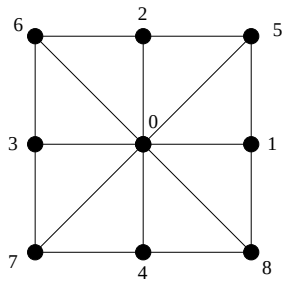

Figure 5.1: The D2Q9 lattice.

Assume the equilibrium solution is a function of the collision invariants (i.e. velocity and density) and expand about small velocity:

$$N_i^{(e)} = \rho W_i \left[A + B c_{i\alpha} u_\alpha + C u^2 + D c_{i\alpha} c_{i\beta} u_\alpha u_\beta \right], \tag{5.21}$$

where A, B, C and D are constants and $u = |\mathbf{u}|$. Using the mass conservation condition (equation (5.6)):

$$\rho = \rho \left(A + C u^2 + D u_\alpha u_\beta \lambda_1 \delta_{\alpha\beta} \right), \tag{5.22}$$

so we see that at 0^{th} order

$$A = 1,$$

and at order $O(u^2)$:

$$C + D\lambda_1 = 0.$$

Now, using the momentum conservation (equation (5.7)):

$$B = \frac{1}{\lambda_1}. \tag{5.23}$$

Defining the momentum flux tensor, $\Pi_{\alpha\beta}$, to be the second moment of the equilibrium function we find that

$$\Pi_{\alpha\beta} = \sum_{i=0}^{9} N_i^{(e)} c_{i\alpha} c_{i\beta}, \tag{5.24}$$

$$= p_0 \delta_{\alpha\beta} + \rho u_\alpha u_\beta, \tag{5.25}$$

where $p_0 = \lambda_1 \rho$ and we have set (at order u^2)

$$C\lambda_1 + 3D\lambda_2 = 1, \tag{5.26}$$

and (at order $O(u_\alpha u_\beta)$)

$$2D\lambda_2 = 1. \tag{5.27}$$

A little algebra reveals that

$$\begin{aligned} B &= 3, \\ C &= -\frac{3}{2}, \\ D &= \frac{9}{2}, \\ \lambda_1 &= \frac{1}{3}, \\ \lambda_2 &= \frac{1}{9}, \end{aligned}$$

and the weights are

$$W_i = \begin{cases} \frac{4}{9} & i = 0 \\ \frac{1}{9} & i = 1, 2, 3, 4 \\ \frac{1}{36} & i = 5, 6, 7, 8. \end{cases} \tag{5.28}$$

Therefore, the D2Q9 equilibrium function is given by

$$N_i^{(e)} = \rho W_i \left[1 + 3\mathbf{c}_i\mathbf{u} - \frac{3}{2}u^2 + \frac{9}{2}\left(\mathbf{c}_i \cdot \mathbf{u}\right)^2 \right], \tag{5.29}$$

with pressure p_0 defined by

$$p_0 = \frac{\rho}{3}. \tag{5.30}$$

Note that the pressure satisfies an ideal equation of state and the factor $1/3$ is the speed of sound squared, c_s^2.

5.3 Multi-Scale Analysis

One way of deriving the hydrodynamic equations of motion from the lattice Boltzmann equation is to employ the Chapman-Enskog expansion, which is a form of multi-scale analysis. The first step is to expand equation (5.12) in space and time:

$$\partial_t N_i + c_{i\alpha}\partial_\alpha N_i + \frac{1}{2}\left(\partial_{tt} N_i + 2c_{i\alpha}\partial_t\partial_\alpha N_i + c_{i\alpha}c_{i\beta}\partial_\alpha\partial_\beta N_i\right) + O(\partial^3 N_i) \quad (5.31)$$
$$= -\omega\left(N_i(\mathbf{x},t) - N_i^{(e)}(\mathbf{x},t)\right);$$

where $\partial_{(\cdot)} = \partial/\partial(\cdot)$. To relate the spacial and temporal variations of the macroscopic quantities to the lattice scales we introduce the macroscopic variables $\mathbf{x}_1$, t_1 and t_2:

$$\begin{aligned} \mathbf{x}_1 &= \epsilon\mathbf{x}, \\ t_1 &= \epsilon t, \quad (5.32) \\ t_2 &= \epsilon^2 t, \quad (5.33) \end{aligned}$$

where t_1 describes the short-term linear (sound wave) regime and t_2 represents the long-term dynamics. The corresponding derivatives are

$$\begin{aligned} \partial_t &= \epsilon\partial_{t_1} + \epsilon^2\partial_{t_2}, \quad (5.34) \\ \partial_\alpha &= \epsilon\partial_{\alpha_1}. \quad (5.35) \end{aligned}$$

Now we substitute the above, along with equation (5.34), into equation (5.31) and examine the coefficients of ϵ.

At first order in ϵ we have:

$$\partial_{t_1} N_i^{(0)} + c_{i\alpha}\partial_\alpha N_i^{(0)} = -\omega N_i^{(1)}. \quad (5.36)$$

Use the mass conservation constraint (5.3) on equation (5.36) to obtain:

$$\partial_{t_1}\rho + \partial_\alpha \rho u_\alpha = 0; \tag{5.37}$$

and the momentum conservation constraint (5.7) yields

$$\partial_{t_1}\rho u_\alpha + \partial_\beta \Pi_{\alpha\beta} = 0. \tag{5.38}$$

The second order terms in ϵ give the following relation:

$$\begin{aligned}\partial_{t_1} N_i^{(1)} + \partial_{t_2} N_i^{(0)} + c_{i\alpha}\partial_\alpha N_i^{(1)} + \frac{1}{2}\partial_{t_1 t_1} N_i^{(0)} + c_{i\alpha}\partial_{t_1}\partial_\alpha N_i^{(0)} \\ + \frac{1}{2} c_{i\alpha} c_{i\beta}\partial_\alpha\partial_\beta N_i^{(0)} = -\omega N_i^{(2)},\end{aligned} \tag{5.39}$$

and applying equation (5.3) shows that

$$\partial_{t_2}\rho + \frac{1}{2}\partial_{t_1 t_1}\rho + \partial_{t_1}\partial_\alpha \rho u_\alpha + \frac{1}{2}\partial_\alpha\partial_\beta \Pi_{\alpha\beta} = 0. \tag{5.40}$$

From equations (5.37) and (5.38) we deduce that

$$\partial_{t_1 t_1}\rho = -\partial_{t_1}\partial_\alpha \rho u_\alpha, \tag{5.41}$$

$$= \partial_\alpha\partial_\beta \Pi_{\alpha\beta}, \tag{5.42}$$

and substituting the above into equation (5.40) shows that

$$\partial_{t_2}\rho = 0, \tag{5.43}$$

which, along with equation (5.37) yields the continuity equation:

$$\partial_t \rho + \nabla \cdot \rho \mathbf{u} = 0. \tag{5.44}$$

Next, apply equation (5.4) to equation (5.39) to find

$$\partial_{t_2}\rho u_\alpha + \partial_\beta Q_{\alpha\beta} + \frac{1}{2}\partial_{t_1}\partial_\beta \Pi_{\alpha\beta} + \frac{1}{2}\partial_\beta\partial_\gamma P_{\alpha\beta\gamma} = 0, \tag{5.45}$$

where $P_{\alpha\beta\gamma} = \sum_i N_i^{(0)} c_{i\alpha} c_{i\beta} c_{i\gamma}$ and $Q_{\alpha\beta} = \sum_i N_i^{(1)} c_{i\alpha} c_{i\beta}$.

We have already seen that for a D2Q9 lattice the momentum flux tensor, which gives rise to the Newtonian stress tensor, is

$$\Pi_{\alpha\beta} = p_0 \delta_{\alpha\beta} + \rho u_\alpha u_\beta, \tag{5.46}$$

where the pressure $p_0 = \rho/3$. Up to second order in $\mathbf{u}$,

$$\partial_{t_1} \partial_\beta \Pi_{\alpha\beta} = -\frac{1}{3} \partial_\alpha \partial_\beta \rho u_\beta \tag{5.47}$$

and

$$\partial_\beta \partial_\gamma P_{\alpha\beta\gamma} = \frac{1}{3} \left(\partial_\beta \partial_\beta \rho u_\alpha + 2 \partial_\alpha \partial_\beta u_\beta \right). \tag{5.48}$$

To find $Q_{\alpha\beta}$ we take the second moment of equation (5.36) and rearrange to find:

$$Q_{\alpha\beta} = -\frac{1}{\omega} \left(\partial_{t_1} \Pi_{\alpha\beta} + \partial_\gamma P_{\alpha\beta\gamma} \right). \tag{5.49}$$

The substitution of the above into (5.45) gives

$$\partial_{t_2} \rho u_\alpha + \left(\frac{1}{2} - \frac{1}{\omega} \right) \left[\partial_{t_1} \partial_\beta \Pi_{\alpha\beta} + \partial_\beta \partial_\gamma P_{\alpha\beta\gamma} \right] = 0, \tag{5.50}$$

which can be written as

$$\partial_{t_2} \rho \mathbf{u} = \nu \left(\nabla^2 \rho \mathbf{u} + \nabla \nabla \cdot \rho \mathbf{u} \right), \tag{5.51}$$

where

$$\nu = \frac{1}{3} \left(\frac{1}{\omega} - \frac{1}{2} \right), \tag{5.52}$$

is the kinematic viscosity and we note that $0 < \omega < 2$. Finally, summing equations (5.38) and (5.51) and assuming incompressibility we arrive at the Navier-Stokes equations for incompressible flow:

$$\partial_t \mathbf{u} + \mathbf{u} \cdot \nabla \mathbf{u} = -\frac{1}{\rho} \nabla p_0 + \nu \nabla^2 \mathbf{u}, \tag{5.53}$$

$$\nabla \cdot \mathbf{u} = 0. \tag{5.54}$$

5.4 Generalised LBE

Although simple and elegant, the lattice LBGK equation (5.12) is not without its shortcomings. The single relaxation parameter, ω, implies that heat transfer takes place at the same rate as momentum transfer. Therefore, the Prandtl number, which is defined to be $Pr = \nu/\alpha$, where α is the thermal diffusivity, is always of unit value making equation (5.12) appropriate for isothermal flows only. Additional drawbacks include: the bulk and shear viscosities are identical, causing difficulties in simulating flows at high Reynolds number; limited understanding of lattice Boltzmann stability properties; and little freedom to extend the model to complex fluids whose stress tensors are characterised by more complicated constitutive relations. These problems can be addressed by considering the full collision operator in equation (5.9) and 'tuning' the matrix elements to obtain the desired properties. This task was systematically studied by Lallemand and Luo [30] and in this section we adopt their strategy.

Equation (5.9) can be written in the following concise form[2]:

$$|\delta N(\mathbf{x} + \mathbf{c}_i, t + 1)\rangle = |\delta N(\mathbf{x}, t)\rangle + \mathbf{M}|\delta N(\mathbf{x}, t)\rangle, \tag{5.55}$$

where $|X\rangle = (X_0, X_1, \ldots, X_8)^t$ with the superscript t denoting the matrix transpose, and $|\delta N\rangle$ is the fluctuating (non-equilibrium) part of the distribution function. Most D2Q9 models are constructed in a 9-dimensional vector space $\mathbf{R}^9$ spanned by $|N\rangle$, but the generalised LBE of Lallemand and Luo is instead based upon the moments $\{m_k \mid k = 0, \ldots, 8\}$ of N_i which are defined as

$$m_k = \langle \psi_k | N \rangle = \langle N | \psi_k \rangle, \quad \langle N| = (N_0, \ldots, N_8)\,, \tag{5.56}$$

where $\{|\psi_k\rangle\}$ is an orthogonal dual basis set obtained by the Gram-Schmidt procedure from polynomials of the lattice vectors $c_{i\alpha}$. If the members of the basis $\{|\psi_k\rangle\}$ are also set to be the eigenvectors of the matrix $\mathbf{M}$, the

[2]Here we are using the D2Q9 lattice but the application to other lattices follows the same path.

linear relaxation in moment space naturally accomplishes the collision process [8]. From our previous discussions on (Newtonian) LBE hydrodynamics we already know some of the eigenvectors $|\psi_k\rangle$. To ensure that the correct expressions for density, momentum and stress are obtained, the following vectors are used:

$$|\psi_0\rangle_i = |\mathbf{c}_i|^0 = 1, \tag{5.57}$$
$$|\psi_1\rangle_i = c_{ix}, \tag{5.58}$$
$$|\psi_2\rangle_i = c_{iy}, \tag{5.59}$$
$$|\psi_3\rangle_i = c_{ix}^2 - c_{iy}^2, \tag{5.60}$$
$$|\psi_4\rangle_i = c_{ix}c_{iy}. \tag{5.61}$$

The corresponding moments m_k, $k = 0, \ldots, 4$ give the density, x-component of momentum, y-component of momentum, and the diagonal and off diagonal components of the stress tensor, respectively. The remaining moments can be chosen according to the meso/macroscopic phenomena that is being modelled, such as multi-phase effects [40] and viscoelastic effects [13], for example (we shall return to the topic of viscoelasticity in Chapter 8). In [30], Lallemand and Luo find the following remaining (kinetic) moments:

$$|\psi_5\rangle_i = -4|\mathbf{c}_i|^0 + 3\left(c_{ix}^2 + c_{iy}^2\right), \tag{5.62}$$
$$|\psi_6\rangle_i = 4|\mathbf{c}_i|^0 - \frac{21}{2}\left(c_{ix}^2 + c_{iy}^2\right) + \frac{9}{2}\left(c_{ix}^2 + c_{iy}^2\right)^2, \tag{5.63}$$
$$|\psi_7\rangle_i = \left[-5|\mathbf{c}_i|^0 + 3\left(c_{ix}^2 + c_{iy}^2\right)\right] c_{ix}, \tag{5.64}$$
$$|\psi_8\rangle_i = \left[-5|\mathbf{c}_i|^0 + 3\left(c_{ix}^2 + c_{iy}^2\right)\right] c_{iy}, \tag{5.65}$$

corresponding to the physical quantities of energy, energy square, and the x and y-components of the energy flux[3] so that

$$|m\rangle = (\rho, j_x, j_y, P_{xx}, P_{yy}, e, \epsilon, q_x, q_y)^\dagger. \tag{5.66}$$

Each nonconserved moment has its own equilibrium state which is a function

[3]Note that to simplify the algebra, the eigenvectors $|\psi_k\rangle$ have not been normalised.

of the conserved moments. A possible choice for these states is [30]:

$$
\begin{aligned}
\psi_3^{(e)} &= \alpha_1 \frac{1}{\langle\psi_4|\psi_4\rangle}\left[\langle\psi_1|\psi_1\rangle j_x^2 - \langle\psi_2|\psi_2\rangle j_y^2\right) \\
&= \frac{3}{2}\alpha_1\left(j_x^2 - j_y^2\right), \qquad (5.67) \\
\psi_4^{(e)} &= \alpha_2 \frac{\sqrt{\langle\psi_1|\psi_1\rangle\langle\psi_2|\psi_2\rangle}}{\langle\psi_5|\psi_5\rangle}\left(j_x j_y\right) \\
&= \frac{3}{2}\alpha_2\left(j_x j_y\right), \qquad (5.68) \\
\psi_5^{(e)} &= \frac{1}{\langle\psi_6|\psi_6\rangle}\left[\beta_1\langle\psi_0|\psi_0\rangle\rho + \alpha_3(\langle\psi_1|\psi_1\rangle j_x^2 + \langle\psi_2|\psi_2\rangle j_y^2)\right] \\
&= \frac{1}{4}\beta_1\rho + \frac{1}{6}\alpha_3\left(j_x^2 + j_y^2\right), \qquad (5.69) \\
\psi_6^{(e)} &= \frac{1}{\langle\psi_7|\psi_7\rangle}\left[\beta_2\langle\psi_0|\psi_0\rangle\rho + \alpha_4(\langle\psi_1|\psi_1\rangle j_x^2 + \langle\psi_2|\psi_2\rangle j_y^2)\right] \\
&= \frac{1}{4}\beta_2\rho + \frac{1}{6}\alpha_4\left(j_x^2 + j_y^2\right), \qquad (5.70) \\
\psi_7^{(e)} &= \frac{\langle\psi_1|\psi_1\rangle}{\langle\psi_7|\psi_7\rangle}\gamma_1 j_x \\
&= \frac{1}{2}\gamma_1 j_x, \qquad (5.71) \\
\psi_8^{(e)} &= \frac{\langle\psi_2|\psi_2\rangle}{\langle\psi_8|\psi_8\rangle}\gamma_1 j_y \\
&= \frac{1}{2}\gamma_3 j_y, \qquad (5.72)
\end{aligned}
$$

where $\alpha_{1,2,3,4}$, $\beta_{1,2}$ and γ_1 are constants that will be determined in the next section. Based on the assumption that the nonconserved modes relax linearly

towards their equilibrium state, the post-collision moments $\hat{m}_k$ are given by

$$\begin{aligned}
\hat{P}_{xx} &= P_{xx} - \tau_1 \left[P_{xx} - P_{xx}^{(e)}\right], && (5.73)\\
\hat{P}_{xy} &= P_{xy} - \tau_2 \left[P_{xy} - P_{xy}^{(e)}\right], && (5.74)\\
\hat{e} &= e - \tau_3 \left[e - e^{(e)}\right], && (5.75)\\
\hat{\epsilon} &= \epsilon - \tau_4 \left[\epsilon - \epsilon^{(e)}\right], && (5.76)\\
\hat{q}_x &= q_x - \tau_5 \left[q_x - q_x^{(e)}\right], && (5.77)\\
\hat{q}_y &= q_y - \tau_6 \left[q_y - q_y^{(e)}\right]. && (5.78)
\end{aligned}$$

There exists a simple linear mapping, $\mathbf{T}$, that relates the distribution functions $|N\rangle$ to the moments $|m\rangle$: $|m\rangle = \mathbf{T}|N\rangle$ and $|N\rangle = \mathbf{T}^{-1}|m\rangle$ and the linearised lattice Boltzmann equation (5.55) may be written as

$$|\delta N(\mathbf{x} + \mathbf{c}_i, t+1)\rangle = |\delta N(\mathbf{x}, t)\rangle + \mathbf{T}^{-1}\mathbf{C}\mathbf{T}|\delta N(\mathbf{x}, t)\rangle, \qquad (5.79)$$

where

$$C_{ji} = \frac{\langle m_j|m_j\rangle}{\langle m_i|m_i\rangle}\frac{\partial \hat{m}_i}{\partial m_j}\Big|_{|m\rangle=|m^{(e)}\rangle} \qquad (5.80)$$

is the collision operator in moment space and is found to be

$$\mathbf{C} = \begin{pmatrix}
0 & 0 & 0 & 0 & 0 & 0 & 0 & 0 & 0\\
0 & 0 & 0 & 0 & 0 & 0 & 0 & 0 & 0\\
0 & 0 & 0 & 0 & 0 & 0 & 0 & 0 & 0\\
0 & 3\tau_1\alpha_1 V_x & -3\tau_1\alpha_1 V_y & -\tau_1 & 0 & 0 & 0 & 0 & 0\\
0 & 3\tau_2\alpha_2 V_y/2 & 3\tau_2\alpha_2 V_x/2 & 0 & -\tau_2 & 0 & 0 & 0 & 0\\
\tau_3\beta_1/4 & \tau_3\alpha_3 V_x/3 & \tau_3\alpha_3 V_y/3 & 0 & 0 & -\tau_3 & 0 & 0 & 0\\
\tau_4\beta_2/4 & \tau_4\alpha_4 V_x/3 & \tau_4\alpha_4 V_y/3 & 0 & 0 & 0 & -\tau_4 & 0 & 0\\
0 & \tau_5\gamma_1/2 & 0 & 0 & 0 & 0 & 0 & -\tau_5 & 0\\
0 & 0 & \tau_6\gamma_1/2 & 0 & 0 & 0 & 0 & 0 & -\tau_6
\end{pmatrix}. \qquad (5.81)$$

Clearly, $\mathbf{T} = (|\psi_0\rangle, \ldots, |\psi_8\rangle)^t$.

To examine how the transport coefficients depend on a wave vector $\mathbf{k}$ and to determine the LBE stability properties, a Fourier transform is performed

on equation (5.79) which yields:

$$\mathbf{A}|\delta N(\mathbf{k}+\mathbf{c}_i, t+1)\rangle = \left[\mathbf{I}+\mathbf{T}^{-1}\mathbf{C}\mathbf{T}\right]|\delta N(\mathbf{k},t)\rangle, \tag{5.82}$$

where $\mathbf{I}$ denotes the identity matrix,

$$A_{ij} = \exp(\imath \mathbf{c}_i \cdot \mathbf{k})\delta_{ij} \tag{5.83}$$

is the streaming operator and $\imath = \sqrt{-1}$. A more concise form of (5.82) is

$$|\delta N(\mathbf{k}, t+1)\rangle = \mathbf{L}|\delta N((\mathbf{k},t)\rangle, \tag{5.84}$$

where

$$\mathbf{L} = \mathbf{A}^{-1}\left[\mathbf{I}+\mathbf{T}^{-1}\mathbf{C}\mathbf{T}\right] \tag{5.85}$$

is the linearised evolution operator.

The difference equation (5.84) has solutions of the form

$$|G(\mathbf{x},t)\rangle = \lambda^t K_x^m K_y^n |X\rangle \tag{5.86}$$

where t here denotes time and m and n are indices for space ($\mathbf{x} = m\bar{\mathbf{x}} + n\bar{\mathbf{y}}$ and $\bar{\mathbf{x}}$ and $\bar{\mathbf{y}}$ are unit vectors in Cartesian coordinates). $|X\rangle$ is the initial state. For a fully periodic system the above solution can be chosen as

$$|\delta N\rangle = \exp(\lambda t - \imath \mathbf{k}\cdot\mathbf{x})|G\rangle, \tag{5.87}$$

which leads to the following eigenvalue equations [30]:

$$\lambda|X\rangle = \mathbf{L}|X\rangle, \tag{5.88}$$

$$\det\left[\mathbf{I}-\lambda\mathbf{L}\right] = 0. \tag{5.89}$$

The roots of the characteristic equation (5.89) determine the transport coefficients and their dependence on $\mathbf{k}$. The solution of the above equation also

provides the solution of the initial value problem (5.84):

$$|\delta N(\mathbf{k}, t+1)\rangle = \mathbf{L}^t |\delta N(\mathbf{k}, 0)\rangle = \sum_\mu \lambda_\mu^t |\phi_\mu\rangle \langle \phi'_\mu | \delta N(\mathbf{k}, 0)\rangle; \tag{5.90}$$

where $|\phi_\mu\rangle$ is the right eigenvector of $\mathbf{L}$ corresponding to eigenvalue λ_μ and $\langle \phi'_\mu|$ is the left eigenvector. Note that since the matrix $\mathbf{L}$ is non-symmetric and non-Hermitian, the right and left eigenvectors are neither equal nor orthogonal, but they do form a complete bi-orthonormal set, i.e.

$$\sum_\mu |\phi_\mu\rangle \langle \phi'_\mu| = \mathbf{I}, \tag{5.91}$$

$$\langle \phi'_\upsilon | \phi_\mu \rangle = \delta_{\upsilon\mu}. \tag{5.92}$$

The dispersion relation is complicated and one cannot get analytic expressions for the roots in λ, except for some very special cases. When $k_x = k_y = 0$ equation (5.89) factorises as

$$(1-\lambda)^3[\lambda - (1-\tau_1)][\lambda - (1-\tau_2)][\lambda - (1-\tau_3)]\times \tag{5.93}$$

$$[\lambda - (1-\tau_4)][\lambda - (1-\tau_5)][\lambda - (1-\tau_6)] = 0 \tag{5.94}$$

and since the hydrodynamic regime corresponds to long times and large spacial scales (i.e. when $k = |\mathbf{k}| \to 0$), the hydrodynamic eigenvalues are those with λ close to 1. Luo and Lallemand [30] suggest solving equation (5.88) by expanding the evolution operator, $\mathbf{L}$, in powers of k and applying Gaussian elimination to the matrix using $1/\tau_\alpha$ as small parameters for the non-conserved (kinetic) modes. Doing this successfully leads to a new 3×3 determinant for the conserved (hydrodynamic) modes. Due to the complexity of the dispersion matrix and the large number of unknowns this procedure is rather cumbersome. Therefore, we choose to solve the dispersion equation

by considering a perturbation expansion of equation (5.88) [56], i.e.

$$\mathbf{L} = \mathbf{L}^{(0)} + \mathbf{L}^{(1)} + \mathbf{L}^{(2)} + \ldots, \tag{5.95}$$

$$\phi_\mu = \phi_\mu^{(0)} + \phi_\mu^{(1)} + \phi_\mu^{(2)} + \ldots, \tag{5.96}$$

$$\lambda_\mu = \lambda_\mu^{(0)} + \lambda_\mu^{(1)} + \lambda_\mu^{(2)} + \ldots, \tag{5.97}$$

where the superscripts refer to the order of $k \ll 1$ and

$$\mathbf{L}^{(n)} = \mathbf{K}^{(n)} \left[\mathbf{I} + \mathbf{M}^{-1}\mathbf{C}\mathbf{M}\right], \tag{5.98}$$

$$K_{ij}^n = \frac{1}{n!} \left(-\imath \mathbf{k} \cdot \mathbf{c}_i\right)^n \delta_{ij}. \tag{5.99}$$

The transport coefficients are related to the eigenvalues of $\mathbf{L}$ through the following [30]:

$$\nu(\mathbf{k}) = -\frac{1}{k^2} \Re(\ln \lambda_T(\mathbf{k})), \tag{5.100}$$

$$g(\mathbf{k}) V \cos\psi = -\frac{1}{k} \Im(\ln \lambda_T(\mathbf{k})), \tag{5.101}$$

$$\frac{1}{2}\nu(\mathbf{k}) + \zeta(\mathbf{k}) = -\frac{1}{k^2} \Re(\ln \lambda_\pm(\mathbf{k})), \tag{5.102}$$

$$c_s(\mathbf{k}) \pm g(\mathbf{k}) V \cos\psi = \mp\frac{1}{k} \Im(\ln \lambda_\pm(\mathbf{k})), \tag{5.103}$$

where ν is the kinematic viscosity, ζ is the bulk viscosity, g is a Galilean invariant factor ($g = 1$ implies Galilean invariance), ψ is the angle between $\mathbf{V}$ and $\mathbf{k}$, and λ_T and $\lambda_\pm$ are the eigenvalues corresponding to the tranverse and longitudinal hydrodynamic modes of the system. The transport coefficients are to be obtained through a perturbation analysis so the following series expansion is used:

$$\nu(\mathbf{k}) = \nu^{(0)} + \nu^{(1)}k^2 + \ldots + \nu^{(n)}k^{2n} + \ldots, \tag{5.104}$$

$$\zeta(\mathbf{k}) = \zeta^{(0)} + \zeta^{(1)}k^2 + \ldots + \zeta^{(n)}k^{2n} + \ldots, \tag{5.105}$$

$$C(\mathbf{k}) = C^{(0)} + C^{(1)}k^2 + \ldots + C^{(n)}k^{2n} + \ldots, \tag{5.106}$$

$$g(\mathbf{k}) = g^{(0)} + g^{(1)}k^2 + \ldots + g^{(n)}k^{2n} + \ldots. \tag{5.107}$$

Examining the resulting dispersion equation at different orders of k gives the transport coefficients and the bounds on the free parameters.

5.4.1 The Eigenvalues and Transport Coefficients

Substituting the expansions (5.95), (5.96) and (5.97) into the dispersion equation (5.88) yields the set of equations:

$$\begin{aligned}
\mathbf{L}^{(0)}|\phi_\mu^{(0)}\rangle &= \lambda_\mu^{(0)}|\phi_\mu^{(0)}\rangle, && (5.108)\\
\left(\mathbf{L}^{(0)} - \lambda_\mu^{(0)}\mathbf{I}\right)|\phi_\mu^{(1)}\rangle &= -\left(\mathbf{L}^{(1)} - \lambda_\mu^{(1)}\mathbf{I}\right)|\phi_\mu^{(0)}\rangle, && (5.109)\\
\left(\mathbf{L}^{(0)} - \lambda_\mu^{(0)}\mathbf{I}\right)|\phi_\mu^{(2)}\rangle &= -\left(\mathbf{L}^{(2)} - \lambda_\mu^{(2)}\mathbf{I}\right)|\phi_\mu^{(0)}\rangle && (5.110)\\
&\quad -\left(\mathbf{L}^{(1)} - \lambda_\mu^{(1)}\mathbf{I}\right)|\phi_\mu^{(1)}\rangle.
\end{aligned}$$

We first consider the simpler case in which the streaming velocity $\mathbf{V} = \mathbf{0}$. Equation (5.108) is easily solved and an eigenvalue $\lambda_\mu^{(0)} = 1$ with a three fold degeneracy is found. These eigenvalues correspond to three hydrodynamic (conserved) modes. Due to the degeneracy of $\lambda_\mu^{(0)}$ the corresponding $O(1)$ eigenvectors, $|z_n\rangle$, are linearly dependent and the general solution to equation (5.108) is a linear combination of these vectors:

$$|\phi_\mu^{(0)}\rangle = \sum_n B_{\mu,n}|z_n\rangle, \tag{5.111}$$

where the $B_{\mu,n}$'s are coefficients to be determined.

To solve the order k equation we multiply (5.109) to the left with $\langle z'_m|$:

$$\begin{aligned}
\langle z'_m|\mathbf{L} - \lambda_\mu^{(1)}\mathbf{I}|\phi_\mu^{(0)}\rangle &= \\
\sum_n \langle z'_m|\mathbf{L} - \lambda_\mu^{(1)}\mathbf{I}|z_n\rangle B_{\mu,n} &= 0, && (5.112)
\end{aligned}$$

where the left vectors, $\langle z'_m|$, are found by solving the transpose of equation (5.108). For future reference we define the general solution to the 'left' equation to be

$$\langle \phi_\upsilon'^{(0)}| = \sum_m B'_{\upsilon,m}\langle z'_m|. \tag{5.113}$$

Equation (5.112) is an eigenvalue problem to order k in the sub-space spanned by the hydrodynamic modes, i.e. $|\mathbf{L} - \lambda_\mu^{(1)}| = 0$. The characteristic polynomial is of degree 3 in $\lambda_\mu^{(1)}$ and can be solved to find

$$\lambda_T^{(1)} = 0, \tag{5.114}$$

$$\lambda_\pm^{(1)} = \pm \imath k c_s, \tag{5.115}$$

with the speed of sound squared given by

$$c_s^2 = \frac{1}{3}\left(2 + \frac{\beta_1}{8}\right). \tag{5.116}$$

To ensure positivity of the speed of sound we require $\beta_1 > -16$. The coefficients $B_{\mu,n}$, and hence the eigenvectors $|\phi_\mu^{(0)}\rangle$, are found by substituting $\lambda_\mu^{(1)}$ into equation (5.112) and solving the linear system. A similar procedure applied to the left equation yields the particular solution $\langle \phi_\mu'^{(0)}|$. The general solution to equation (5.109) is

$$|\phi_\mu^{(1)}\rangle = -\left(\mathbf{L}^{(0)} - \lambda_\mu^{(0)}\mathbf{I}\right)^{-1}\left(\mathbf{L}^{(1)} - \lambda_\mu^{(1)}\mathbf{I}\right)|\phi_\mu^{(0)}\rangle + \sum_n D_{\mu,n}|\phi_\mu^{(0)}\rangle, \tag{5.117}$$

where $D_{\mu,n}$ are constant coefficients. Since the matrix $\left(\mathbf{L}^{(0)} - \lambda_\mu^{(0)}\mathbf{I}\right)$ is singular we find the first term on the right-hand-side of equation (5.117), which we call $|\sigma_\mu^{(1)}\rangle$, by applying the method of Gaussian elimination and back-substitution to the linear system (5.109).

To find the eigenvalues at order k^2 we multiply equation (5.110) to the left by $\langle \phi_\upsilon'^{(0)}|$ and rearrange to obtain

$$\lambda_\mu^{(2)} = \frac{1}{\langle \phi_\upsilon'^{(0)}|\phi_\mu^{(0)}\rangle}\Big[\langle \phi_\upsilon'^{(0)}|\mathbf{L}^{(2)}|\phi_\mu^{(1)}\rangle + \langle \phi_\upsilon'^{(0)}|\mathbf{L}^{(1)} - \lambda_\mu^{(1)}\mathbf{I}|\sigma_\mu^{(1)}\rangle + \textstyle\sum_n D_{\mu,n}\langle \phi_\upsilon'^{(0)}|\mathbf{L}^{(1)} - \lambda_\mu^{(1)}\mathbf{I}|\phi_\mu^{(0)}\rangle\Big]. \tag{5.118}$$

For $\upsilon = \mu$ the last term on the right-hand-side of equation (5.118) vanishes

and we find the following expressions for the eigenvalues:

$$\lambda_T^{(2)} = -k^2\nu_0 = \frac{\langle \phi_T'^{(0)}|\mathbf{L}^{(2)}|\phi_T^{(1)}\rangle + \langle \phi_T'^{(0)}|\mathbf{L}^{(1)}|\sigma_T^{(1)}\rangle}{\langle \phi_T'^{(0)}|\phi_T^{(0)}\rangle}; \tag{5.119}$$

$$\begin{aligned}\lambda_\pm^{(2)} &= -k^2(\nu_0+\zeta_0)\\ &= \frac{\langle \phi_\pm'^{(0)}|\mathbf{L}^{(2)}|\phi_\pm^{(1)}\rangle + \langle \phi_\pm'^{(0)}|\mathbf{L}^{(1)} \pm \imath k c_s \mathbf{I}|\sigma_\pm^{(1)}\rangle}{\langle \phi_\pm'^{(0)}|\phi_\pm^{(0)}\rangle}.\end{aligned} \tag{5.120}$$

The above depend on the direction of the wave vector $\mathbf{k}$. To eliminate this effect and ensure isotropy we require the expressions to factorise in k^2. This is achieved if we set

$$\frac{1}{\tau_2} - \frac{1}{2} = 2\left(\frac{1}{\tau_1} - \frac{1}{2}\right)\frac{\gamma_1+4}{2-\gamma_1}, \tag{5.121}$$

which leads to expressions for the kinematic and bulk viscosity in the long wave-length limit ($\mathbf{k} \to 0$):

$$\nu_0 = \frac{2-\gamma_1}{12}\left(\frac{1}{\tau_1} - \frac{1}{2}\right), \tag{5.122}$$

$$\zeta_0 = \frac{\gamma_1 + 10 - 12c_s^2}{24}\left(\frac{1}{\tau_3} - \frac{1}{2}\right), \tag{5.123}$$

where $-4 < \gamma_1 < 2$ and $0 < \tau_1, \tau_2, \tau_3 < 2$ by the positivity of the transport coefficients.

To determine the other adjustable parameters and narrow the bounds of β_1 and γ_1 we now consider the dispersion equation with a constant streaming velocity $\mathbf{V}$. To satisfy Gallilean invariance we must have $g_0 = 1$, which is only obtained when

$$\alpha_1 = \alpha_2 = \frac{2}{3}, \quad \alpha_3 = 18. \tag{5.124}$$

We proceed in the same way as the case when $\mathbf{V} = \mathbf{0}$ by examining the dispersion equation to different orders in k. After solving equation (5.108), equation (5.109) is solved to find the speed of sound, C_s:

$$C_s = \mathbf{V}\cdot\mathbf{k} \pm \sqrt{c_s^2 + (\mathbf{V}\cdot\mathbf{k})^2}. \tag{5.125}$$

The second order eigenvalues are complicated expressions that depend on the direction of the wave vector k. If we set $\gamma_1 = -2$, the shear and bulk viscosities are found to be

$$\begin{aligned}
\nu_0 &= \left[\tau_3(2-\tau_1)\left[c_s^2 + (1-3c_s^2)(\mathbf{V}\cdot\mathbf{k})^2\right] + 3[2[\tau_1 - \tau_3]\right. \\
&\quad \left. +\tau_1(\tau_3 - 2)(\mathbf{V}\cdot\mathbf{k})^2/V]\right] / [6\tau_3\tau_1((\mathbf{V}\cdot\mathbf{k})^2 + c_s^2)], \qquad (5.126) \\
\zeta_0 &= \Big[(\mathbf{V}\cdot\mathbf{k})\sqrt{c_s^2 + (\mathbf{V}\cdot\mathbf{k})^2}\left(12V^2[(\tau_3 - \tau_1) + \tau_3(\tau_1 - 2)(\mathbf{V}\cdot\mathbf{k})^2/V^2]\right. \\
&\quad \left.(2\tau_3 - 3\tau_3\tau_1 + 4\tau_1)(1 - 3c_s^2)\right) + 3(\mathbf{V}\cdot\mathbf{k})^2[(\mathbf{V}\cdot\mathbf{k})^2(2\tau_1 + 3\tau_1\tau_3 - 8\tau_1) \\
&\quad 6V^2(\tau_3 - \tau_1)] + 2(\mathbf{V}\cdot\mathbf{k})^2[6(2\tau_1\tau_3 - \tau_3 - \tau_1)c_s^2 + \tau_1(2 - \tau_3)] \\
&\quad +c_s^2\left[6V^2(\tau_3 - \tau_1) + \tau_1(2 - \tau_3)\right. \\
&\quad \left.\times(2 - 3c_s^2)\right]\Big] / \left[12\tau_1\tau_3((\mathbf{V}\cdot\mathbf{k})^2 + c_s^2)\right] \qquad (5.127)
\end{aligned}$$

The effect of V on the transport coefficients is clear. Setting $c_s^2 = 1/3$ (that is, $\beta_1 = -8$) eliminates the first order effect of $\mathbf{V}$ on ζ_0 and the second order effect on ν_0. Lallemand and Luo [30] argue that the second order effects of $\mathbf{V}$ on C_s and ζ_0 can be removed by considering a more complicated 13 velocity lattice and allowing for compressibility effects in the equilibrium properties. Note that the model reduces to the LBGK equation (5.12) if we set all the relaxation parameters to be equal ($\tau_\alpha = \omega$) and choose $\beta_2 = 4$, $\alpha_4 = -18$.

By conducting a perturbation analysis on the dispersion equation (5.88) we have found expressions for the hydrodynamic transport coefficients that are the same as those in [30] and are optimal in the sense that they yield the desirable properties. The value of this approach is it provides a means to analyse the generalised hydrodynamic behaviour of the LBE which can be compared to that of the Navier-Stokes equations. If (to a certain value of $\mathbf{k}$) the modes of the LBE and Navier-Stokes equations behave in exactly the same way (as shown in [30]) then there is no distinction between the two sets of equations (to a given order of $\mathbf{k}$) and the Chapman-Enskog analysis (which can be rather cumbersome for models more complicated that the D2Q9 LBGK equation (5.12) can be bypassed. Also, the ability to study the LBE for a range of k (which the Chapman-Enskog analysis cannot do) reveals some shortcomings of the D2Q9, namely the dependence of the transport co-

efficients on the mean velocity $\mathbf{V}$. The generalised LBE separates different time scales within the model, allowing for the incorporation of sophisticted physics such as energy modes (important for defining non-isothermal LBE's that are consistent with thermodynamics) and non-Newtonian constitutive relations for the stress tensor. It has been shown that having separate relaxation times for the kinetic modes can increase the stability of the model [30].

5.5 Boundary Conditions

In conventional CFD, boundary conditions are generally given in terms of velocity. This leads to potential difficulties in the approximation of the pressure gradient term in the momentum equation and the discretisation of the Navier-Stokes equations using standard finite element/volume/difference methods may give rise to numerical instabilities, particularly at the boundaries. One of the advantages the lattice Boltzmann method has over its continuum counterparts is the ease with which it can incorporate rather complex geometries, thanks to particle nature inherited from the LGCA.

5.5.1 'Bounce-Back' and Periodic Conditions

The most simple way to apply external boundaries is to use the method of surrounding the flow domain with a set of buffer nodes, as in Figure 5.2.

Each fluid site has the address (i, j) where $i = 1, 2, ..., nx$, and $j = 1, 2, ..., ny$, (nx=6 and ny=5 in Figure 5.2). The buffer sites can be grouped as N, S, E, W representing the north, south, east and west layers, respectively, to form the sets

$$N = \{(i, ny + 1) : i = 0, 1, \ldots, nx + 1\}, \tag{5.128}$$

$$S = \{(i, 0) : i = 0, 1, \ldots, nx + 1\}, \tag{5.129}$$

$$E = \{(nx + 1, j) : j = 0, 1, \ldots, ny + 1\}, \tag{5.130}$$

$$W = \{(0, j) : j = 0, 1, \ldots, ny + 1\} \tag{5.131}$$

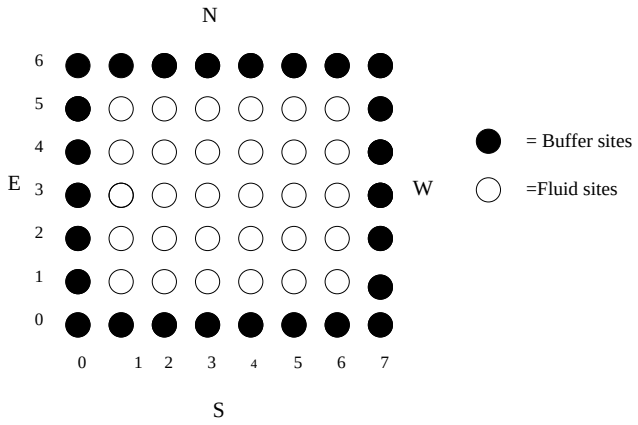

Figure 5.2: Buffer sites for a 6×5 fluid domain.

Fluid 'particles' are forbidden from moving along these sites and they serve only as an apparatus that redistribute the populations. Specific attention is now given to periodic and no-slip boundary conditions using the D2Q9 lattice.

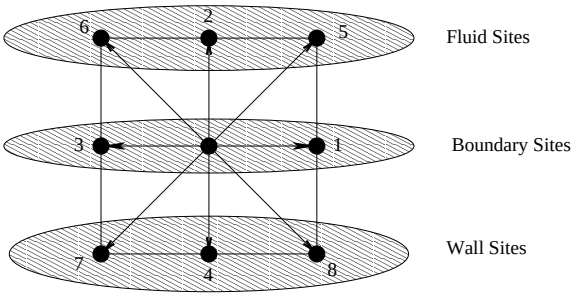

Figure 5.3: A site on the south boundary with fluid sites above and solid wall below.

Periodic Boundary Conditions

In computational fluid dynamics, if a domain D is symmetric and the flow within periodic then only a section A of D needs to be modelled. This technique can be easily adapted to the lattice Boltzmann method with periodic boundary conditions applied to the necessary sites of the section A. We give

particular attention to a flow with periodicity imposed at the far left and far right of the section. If, in the discrete world, a fluid particle is about to leave A, that is it reaches either the east or west side buffer (see Figure 5.2), then it is simply re-entered at the opposite end of the computational geometry with the same velocity. This method ensures that the conservation of mass constraint (equation (5.3)) is not violated. To clarify the situation, consider a fluid particle approaching the east buffer (set E). If it is moving in a horizontal direction (that is in the direction $\mathbf{c}_1$) the distribution function $N_1[(nx, j), t]$ at time t is propagated to the west buffer $N_1[(0, j), t+1]$ at the next time step. This is shown visually in Figure 5.4. The same rule applies to particles moving in any direction that will take them out of A. These boundary conditions are written as [61]

$$N_{\{in,W\}}(W) = N_{\{out,E\}}(EF), \tag{5.132}$$
$$N_{\{in,E\}}(E) = N_{\{out,W\}}(WF), \tag{5.133}$$

where W and E are the sets defined in equation (5.128) and EF and WF stand for the eastward fluid and westward fluid sites respectively. These sets are

$$EF = \{(nx, j) : j = 0, 1, ..., ny + 1\}, \tag{5.134}$$
$$WF = \{(0, j) : j = 0, 1, ..., ny + 1\}, \tag{5.135}$$

The subscripts 'in' and 'out' refer to the inward and outward populations, respectively. For the D2Q9 lattice of Figure 5.1 these read

$$\{in, W\} = \{out, E\} = \{1, 5, 8\}, \tag{5.136}$$
$$\{out, W\} = \{in, E\} = \{3, 6, 7\}, \tag{5.137}$$

The corner buffer sites NW, NE, SW and SE (standing for north west etc) are asked to fulfil the following conditions:

$$N_{\{in\}}(NW) = N_{\{out\}}(SE), \tag{5.138}$$
$$N_{\{in\}}(SW) = N_{\{out\}}(NE), \tag{5.139}$$
$$N_{\{in\}}(NE) = N_{\{out\}}(SW), \tag{5.140}$$
$$N_{\{in\}}(SE) = N_{\{out\}}(NW). \tag{5.141}$$

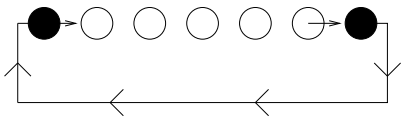

Figure 5.4: The particles that are about to occupy the east side buffer are re-distributed from the west side buffer at the next time step.

An obvious consequence of periodicity is the absence of an inflow and outflow condition. This means that there is nothing driving the flow and therefore an external force must be applied to the fluid to induce motion. For steady Poiseuille flow at moderate Reynolds number the pressure gradient G can be assumed constant and written as $G = (P_i - P_o)/\rho L$, where P_i is the inflow pressure, P_o is the outflow pressure, ρ is the density and L the length of the channel. A problem with the lattice Boltzmann model arises here because although it has been shown (see Section (5.3)) that these equations can recover the Navier Stokes equation, they do not predict any pressure variation. This feature is a direct consequence of the lattice Boltzmann's ancestor, the lattice gas cellular automata. Although the LBE is a tool designed to predict the behaviour of a viscous fluid, its foundations were laid with the intention of simulating the dynamics of an ideal gas and thus incorporates the equation of state for an ideal gas, i.e $P = \rho T$, where P is the pressure and T the temperature. So what has happened to the pressure gradient? In

terms of kinetic theory it has been absorbed into the diagonal component of the non-equilibrium momentum flux tensor $Q_{\alpha\beta} = \sum_i N_i^{(ne)} c_{i\alpha} c_{i\beta}$. This added difficulty is the reason why the Poisson equation for the pressure field is not solved.

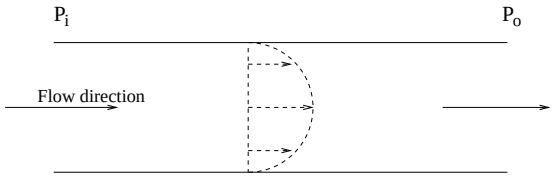

Figure 5.5: Flow through a channel.

This potential drawback can be managed by mimicking the pressure gradient with an equivalent force. For the specific case of Poiseuille flow this is done by biasing the collision rule to increase the distribution functions in the flow direction and decrease the counter flow populations. As an example, consider the flow from left to right through a rectangular channel as shown in Figure 5.5. It is easily shown that for the D2Q9 lattice (Figure 5.1) the force f required is

$$f = \frac{8\rho\nu U_c}{W^2}, \tag{5.142}$$

where U_c is the maximum value of the fluid velocity and W is the width of the channel. The force f is required to be sufficiently small in order to prevent the affected populations breaking the probabilistic requirement that $0 < N_i < 1$.

No-Slip Boundary Conditions

The no-slip condition is one of the most important and widely applicable of all boundary conditions. No-slip ensures that the velocity of a fluid at a solid wall is zero. Assuming that such a wall is aligned with a lattice axis, this condition is imposed by simply reflecting any particle that hits the wall back to the site it came from. This is known as the bounce back scheme.

The simplicity of this method supports the claim [61] that the LBM is ideal for simulating flows in complicated geometries such as flow through porous media.

If a solid wall having sufficient friction to prevent any slip lies exactly on a lattice axis, say on the north and south buffer sites of Figure 5.2, then the bounce back scheme is as follows:

$$N_{in}(N) = N_{out}(N), \tag{5.143}$$
$$N_{in}(S) = N_{out}(S), \tag{5.144}$$

where $N_{in}(N)$ is understood to represent the (average) particle populations sitting on the north buffer moving in a northward direction. Similar reasoning holds for the out subscripts and set S. With the above equations the average fluid velocity $\mathbf{u} = (u, v)$, which is calculated from the momentum equation (5.4), is found to be zero in both the normal and tangential directions to the walls, as required. For example, with help from Figure 5.3 the D2Q9 configuration yields

$$u = N_1 + N_5 + N_8 - N_3 - N_6 - N_7 = N_1 - N_3 = 0, \tag{5.145}$$
$$v = N_2 + N_5 + N_6 - N_4 - N_7 - N_8 = 0. \tag{5.146}$$

The requirement in the first equation that $N_1 = N_3$ at the buffer sites is set at the initial time step $t = 0$. These populations are not affected by any subsequent dynamics since particles are restricted from travelling along these nodes.

Despite the simplicity of this method it contains adequate detail to simulate, with reasonable success, flows with no-slip boundary conditions. However, it has been found [73] that the 'on axis' bounce back scheme is only first order in numerical accuracy. This has a detrimental effect on LBM simula-

tions since the lattice Boltzmann family has been shown to be (see Section 5.3) a second-order accurate approximation to the Navier Stokes equation. Ziegler [73] realised that a second-order bounce back scheme can be used if the boundary lies between two lattice grid lines. As an example, consider a solid boundary at the lower end of a flow domain. With reference to Figure 5.2 this wall would now be placed *between* row 0 (south buffer sites) and row 1 (lower most fluid sites). Or, in general, between row $ny - 1$ and ny. The reason why this technique is second order accurate stems from the fact that particles now meet at time $t + 1/2$ rather than at time $t + 1$. The bounce back conditions for the upper and lower walls are now [61]

$$N_{in}(N) = N_{out}(NF), \tag{5.147}$$
$$N_{in}(S) = N_{out}(SF), \tag{5.148}$$

where NF and SF (northward fluid and southward fluid) refer to the set of fluid sites adjacent to the N and S buffers, respectively. They are the sets

$$NF = \{(i, ny) : i = 0, 1, ..., nx + 1\}, \tag{5.149}$$
$$SF = \{(i, 0) : i = 0, 1, ..., nx + 1\}. \tag{5.150}$$

To fix ideas, let a no-slip boundary be placed at the south end of a channel (see Figure 5.6). The mid-axis bounce back condition is explicitly written as

$$\begin{bmatrix} N_5(x,0) \\ N_2(x,0) \\ N_6(x,0) \end{bmatrix} = \begin{pmatrix} 1 & 0 & 0 \\ 0 & 1 & 0 \\ 0 & 0 & 1 \end{pmatrix} \begin{bmatrix} N_7(x+1,1) \\ N_4(x,1) \\ N_8(x-1,1) \end{bmatrix} \tag{5.151}$$

where $(x, 0)$=S.

5.5.2 Interpolation Scheme for Boundaries

The bounce-back treatment of solid boundaries has the computational advantage of being efficient and simple to implement while remaining sufficiently

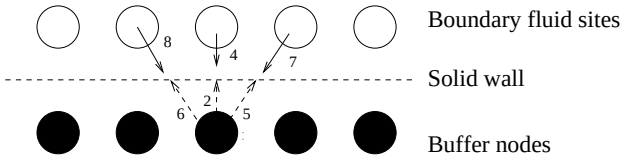

Figure 5.6: The mid-axis bounce back condition at the south buffer. Solid arrow represents the 'in' populations and dashed arrows represent the 'out' populations.

detailed to give second-order accuracy. This level of accuracy is obtained because the wall is placed exactly halfway between two neighbouring lattice nodes. Unfortunately this means curved boundaries have to be approximated with staircase-like geometries, leading to discontinuities which cause larger numerical errors as the Reynolds number increases. To circumvent this inadequacy several authors have proposed alternative methods for computing with surfaces of smooth curvature using more advanced techniques. Mei and Shyy [43] and He and Doolen [21, 22] extend the LBE to curvilinear, or body-fitted, coordinates. Although these methods have produced encouraging results for flows over cylinders they lose some of the lattice Boltzmann's most attractive features such as simplicity and efficiency due to the need to use numerical grid generation techniques, common to standard Navier-Stokes solvers. To retain the inherent LBE advantages, interpolation techniques have been proposed to calculate the distribution functions at a solid wall [5, 10, 42]. Such methods are easily implemented in a Cartesian system and maintain second-order accuracy for curved boundaries [70]. One drawback is a different formula for the boundary condition is required for walls placed at different distances from a lattice node. A unified approach has been proposed by Yu et al. [71] and it is this strategy we choose to adopt.

In general, the boundary condition for the momentum at a solid wall is specified but the distribution functions N_i are not known. Therefore, a satisfactory approximation is sought. Consider a curved surface in a lattice mesh, as shown in Figure 5.7. The nodes inside the boundary are labelled with the vector $\mathbf{x}_b$, the nearest fluid sites are denoted $\mathbf{x}_f$, the next nearest node is $\mathbf{x}_{ff}$ and the exact location of the wall is $\mathbf{x}_w$. Particles travelling

towards the wall have velocity $\mathbf{c}_i$, outgoing particles have velocity $\bar{\mathbf{c}}_i$ and the fraction of an intersected link in the fluid region is

$$\Delta = \frac{|\mathbf{x}_f - \mathbf{x}_w|}{|\mathbf{x}_f - \mathbf{x}_b|}, \quad 0 \leq \Delta \leq 1. \tag{5.152}$$

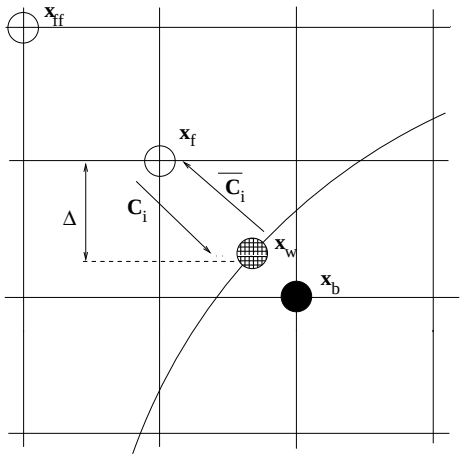

Figure 5.7: Lattice nodes and velocities with a curved boundary.

After the propagation process has been accomplished, $N_i(\mathbf{x}_f, t+1)$ and $N_i(\mathbf{x}_b, t+1)$ are known but $N_{\bar{i}}(\mathbf{x}_f, t+1)$ is not. To obtain this quantity we first approximate $N_i(\mathbf{x}_w, t+1)$ by the following linear interpolation:

$$N_i(\mathbf{x}_w, t+1) = N_i(\mathbf{x}_f, t+1) + \Delta \left[N_i(\mathbf{x}_b, t+1) - N_i(\mathbf{x}_f, t+1) \right]. \tag{5.153}$$

For a no-slip condition we require

$$N_{\bar{i}}(\mathbf{x}_w, t+1) = N_i(\mathbf{x}_w, t+1) \tag{5.154}$$

which is used as part of the linear interpolation for finding $N_{\bar{i}}(\mathbf{x}_f, t+1)$:

$$N_{\bar{i}}(\mathbf{x}_f, t+1) = N_{\bar{i}}(\mathbf{x}_w, t+1) + \frac{\Delta}{1+\Delta} \left[N_{\bar{i}}(\mathbf{x}_f + \mathbf{c}_{\bar{i}}, t+1) - N_{\bar{i}}(\mathbf{x}_w, t+1) \right]. \tag{5.155}$$

For second order accuracy equation (5.153) can be replaced by

$$N_i(\mathbf{x}_w, t+1) = N_i(\mathbf{x}_f, t+1) + \Delta\left[N_i(\mathbf{x}_b, t+1) - N_i(\mathbf{x}_f, t+1)\right] \quad (5.156)$$
$$+\Delta(\Delta-1)\frac{N_i(\mathbf{x}_b, t+1) - 2N_i(\mathbf{x}_f, t+1) + N_i(\mathbf{x}_f + \mathbf{c}_{\bar{i}}, t+1)}{2},$$

and equation (5.155) by

$$\begin{aligned} N_{\bar{i}}(\mathbf{x}_f, t+1) &= N_{\bar{i}}(\mathbf{x}_w, t+1) + \frac{\Delta}{1+\Delta}\left[N_{\bar{i}}(\mathbf{x}_f + \mathbf{c}_{\bar{i}}, t+1) - N_{\bar{i}}(\mathbf{x}_w, t+1)\right] \\ &- \left[\frac{\Delta N_{\bar{i}}(\mathbf{x}_f + 2\mathbf{c}_{\bar{i}}, t+1)}{2+\Delta} - \frac{\Delta N_{\bar{i}}(\mathbf{x}_f + \mathbf{c}_{\bar{i}}, t+1)}{1+\Delta}\right. \\ &+ \left.\frac{\Delta N_{\bar{i}}(\mathbf{x}_w, t+1)}{(2+\Delta)(1+\Delta)}\right]. \end{aligned} \quad (5.157)$$

Inflow/Outflow Conditions

Periodic boundaries are not suitable for complex flows where the downstream velocity does not reach a one-dimensional zero gradient profile. In such cases open boundaries replace the periodicity and inflow and outflow conditions prescribed. An examination of different inlet boundary treatments and their effects on computational stability is presented in [70] and based on these findings we adopt Yu's superposition scheme.

The arguments of Section 5.1 show that $N_i = N_i^{(e)} + N_i^{(ne)}$, where the superscripts e and ne denote the equilibrium and non-equilibrium contributions, respectively, and $N_i^{(ne)} \ll N_i^{(e)}$. Therefore, if $N_{\bar{i}}^{(e)}$ is specified at the inlet (with $\mathbf{c}_{\bar{i}}$ pointing toward the interior of the flow field), then a substantial portion of $N_{\bar{i}}$ at the inlet will be specified.

After the propagation step the number of particles leaving the first column of fluid nodes is not known but can be obtained via an simple interpolation. Denoting the inflow equilibrium function by $N_I^{(e)}$ and the equilibrium distribution on the first and second columns of fluid nodes by $N_A^{(e)}$ and $N_B^{(e)}$,

respectively, we find that

$$N_{\bar{i},A}^{(e)} = N_{\bar{i},I}^{(e)} + \frac{\Delta}{1+\Delta}\left(N_{\bar{i},B}^{(e)} - N_{\bar{i},I}^{(e)}\right). \tag{5.158}$$

The non-equilibrium part of the distribution function at the inlet is unknown but by making use of the bounce-back scheme it can be approximated by

$$N_{\bar{i},I}^{(ne)} = N_{i,B}^{(neq)}, \tag{5.159}$$

and an interpolation for $N_{\bar{i},A}^{(neq)}$ is then obtained:

$$N_{\bar{i},A}^{(neq)} = N_{\bar{i},I}^{(neq)} + \frac{\Delta}{1+\Delta}\left(N_{\bar{i},B}^{(neq)} - N_{\bar{i},I}^{(neq)}\right). \tag{5.160}$$

At the outlet a first order extrapolation is used:

$$N_{i,Z} = 2N_{i,Y} - N_{i,X}, \tag{5.161}$$

where Z is the last column of fluid nodes, Y the previous column, with X adjacent.

5.6 Numerical Simulation

Before considering the complex problem of flow over a confined cylinder we first verify our code and the different boundary treatments with the simulation of laminar Poiseuille flow, as shown in Figure 5.5.

A domain consisting of 128×65 lattice nodes was constructed and the initial density and velocity were chosen to be $\rho = 1$ and $\mathbf{u} = \mathbf{0}$, respectively. The relaxation parameter was set to $\omega = 1.25$, corresponding to a kinematic viscosity of $\nu = 0.1$. The analytical solution for the velocity is easily found to be:

$$u(y) = U_c\left(1 - \frac{4y^2}{W^2}\right), \quad -\frac{W}{2} < y < \frac{W}{2}, \tag{5.162}$$

where W is the channel width and $U_c = 0.1$ is the maximum velocity. Figure 5.8 plots the analytical solution (solid line) and the numerical predictions

for the pressure driven periodic flow using a bounce-back, first order interpolation and second order interpolation schemes for the no-slip boundary condition.

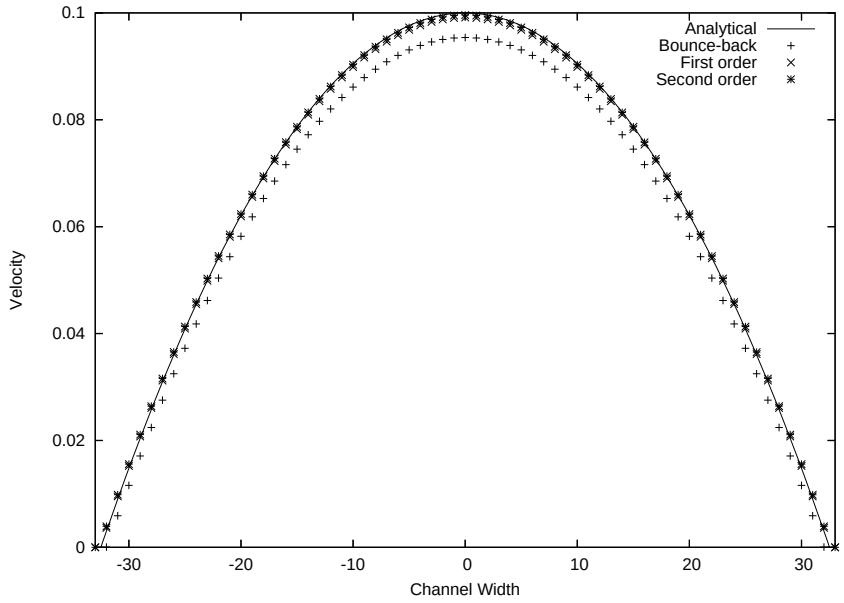

Figure 5.8: Analytical and numerical solutions for the pressure driven Poiseuille flow using three different boundary treatments.

The graph shows the interpolation technique is a clear improvement on the bounce-back scheme for the no-slip boundary condition. When using the interpolation technique an excellent agreement between the analysis and numerics is observed in all channel positions.

Figure 5.9 plots the analytical solution (solid line) and the numerical predictions for laminar Poiseuille flow with inlet/outlet conditions using a bounce-back, first order interpolation and second order interpolation schemes for the no-slip boundary condition. Once again the plot shows that the interpolation scheme gives reliable and accurate predictions for the velocity near a no-slip boundary

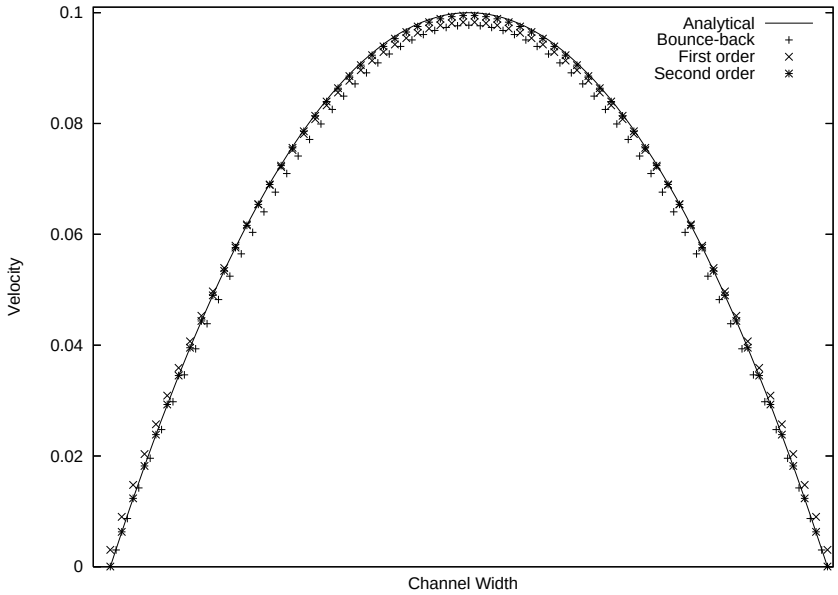

Figure 5.9: Analytical and numerical solutions for the Poiseuille flow with inlet condition using three different boundary treatments.

5.6.1 Flow Over a Cylinder

Since the pioneering work of von Karman, there has been a wealth of interest in the rich topic of flow over a cylinder in a channel. Experimentalists, theoreticians and computational fluid dynamicists, including the lattice Boltzmann community, have sought to explain the interesting flow features associated with this benchmark problem in CFD. Some phenomena, for example the onset of vortices and instabilities at critical Reynolds numbers, the development of von Karman streets in the cylinder wake, and the measurement of quantities such as the drag coefficient at different Reynolds numbers in an unbounded domain are now well understood, but surprising little attention has been paid to the influence of the *lateral* walls on the viscous flow over a confined cylinder. A detailed study of this problem was recently conducted by Sahin [59] and the primary aim of this section is to compare our lattice Boltzmann approach against Sahin's finite volume approach for the measurement of drag and lift coefficients and Strouhal numbers at different Reynolds numbers and blockage ratios.

Drag and Lift Coefficients

The drag and lift coefficients over a cylindrical body are defined to be

$$C_D = \frac{|F_x|}{\rho U^2 R}, \tag{5.163}$$

$$C_L = \frac{|F_y|}{\rho U^2 R} \tag{5.164}$$

where $\mathbf{F} = (F_x, F_y)$ is the force on the body, U is the free-stream velocity and R is the radius of the cylinder. The most common way of finding $\mathbf{F}$ in standard Navier-Stokes solvers is by using a stress integration approach:

$$\mathbf{F} = \int_\gamma \mathbf{n} \cdot \left[p\mathbf{I} + \rho\nu \left(\nabla\mathbf{u} + (\nabla\mathbf{u})^T \right) \right] dA \tag{5.165}$$

where $\mathbf{n}$ is the outward normal vector and γ is the surface of the cylinder. In the lattice Boltzmann framework $\mathbf{u}$ is not a primary variable since it is approximated by the first moment of the distribution function through equation (5.4). Therefore, the evaluation of $\mathbf{u}$ may suffer a loss of accuracy due to round-off errors which will be amplified in the calculation of the gradient field. An alternative method, unique to the LBM, that is simpler to implement and not victim to the aforementioned shortcomings is the momentum exchange approach.

The force on each lattice link is a result of the momentum exchanged by two opposing directions, $\left[\mathbf{c}_{\bar{i}} \hat{N}_i(\mathbf{x}_b, t) - \mathbf{c}_i \hat{N}_i(\mathbf{x}_b + \mathbf{c}_{\bar{i}}, t) \right]$, where $\hat{N}$ denotes the post collision distribution. Therefore, the total force acting on solid body is:

$$\begin{aligned} \mathbf{F} &= \sum_{\mathbf{x}_b} \sum_{i=1}^{8} \mathbf{c}_{\bar{i}} \left[\hat{N}_i(\mathbf{x}_b, t) + \hat{N}_{\bar{i}}(\mathbf{x}_b + \mathbf{c}_{\bar{i}}, t) \right] \\ &\times \left[1 - \chi(\mathbf{x}_b + \mathbf{c}_{\bar{i}}) \right], \end{aligned} \tag{5.166}$$

where

$$\chi(\mathbf{x}_b + \mathbf{c}_{\bar{i}}) = \begin{cases} 0 & \text{at } \mathbf{x}_f, \\ 1 & \text{at } \mathbf{x}_b. \end{cases}$$

The inner summation calculates the momentum exchange between a solid node and all neighbouring fluid nodes, and the outer summation calculates the force contributed by all boundary nodes.

Results

We begin with the steady flow over a column of cylinders since this simpler case has been used as a benchmark test for different CFD techniques, including the lattice Boltzmann method. Consider a column of circular cylinders of radius R and centre-to-centre distance H. To construct this situation we impose symmetry conditions at $y = -H - 1$ (corresponding to $j = 1$ in the computational domain) and $y = H + 1$ (corresponding to $j = M_y$):

$$\begin{aligned}
&N_1(i,1) = N_1(i,3), \qquad &&N_5(i,1) = N_8(i,3), \quad &&N_2(i,1) = N_4(i,3),\\
&N_6(i,1) = N_7(i,3), \qquad &&N_3(i,1) = N_3(i,3), \quad &&N_7(i,1) = N_6(i,3),\\
&N_4(i,1) = N_2(i,3), \qquad &&N_8(i,1) = N_5(i,3), \quad &&N_0(i,1) = N_0(i,3),
\end{aligned}$$

with similar conditions holding at $j = M_y$. The cylinder is centred at $(135, 65)$ and at the inlet a uniform velocity $\mathbf{u} = (V, 0)$ is specified and an extrapolation used at the outlet. To make comparisons with existing results in the literature we choose the following parameters:

$$\begin{aligned}
\rho &= 1,\\
V &= 0.06,\\
\omega &= 1.8657,\\
M_x &= 500,\\
M_y &= 130,\\
R &= 10.
\end{aligned}$$

The Reynolds number is defined to be $Re = \frac{2RV}{\nu}$ and the above parameters give $Re = 100$. Figure 5.10 is a contour plot of the streamwise velocity at $t = 100000$. We observe the expected characteristics of a von Karman vortex street in the wake of the cylinder, the breakdown of symmetry and negative

Present Linear	Present Quadratic	Yu Linear	Yu Quadratic	Fornberg
1.230	1.246	1.275	1.247	1.248

Table 5.1: Comparison of drag coefficient for flow over a column of cylinders at $Re = 100$.

velocity behind the body.

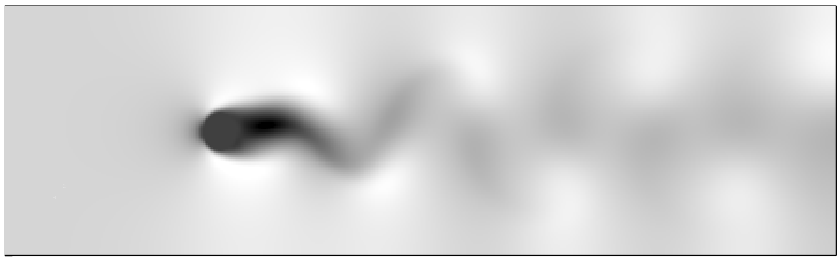

Figure 5.10: Contour plot of flow over a column of cylinders at $Re = 100$.

Table 5.1 shows our computed value of the drag coefficient using the first and second order boundary treatment alongside the predictions of Yu [71] and the established result of Fornberg [11] (finite volume method). It is seen that this lattice Boltzmann algorithm compares well with the results of Fornberg [11] and the second order scheme gives a closer approximation. The slight difference between our results and those of Yu et al. [71] is most likely due to the small difference between the chosen parameters.

To demonstrate mesh convergence we construct two additional meshes, one coarser and one finer than the one mentioned above. The coarse grid, $M0$, has dimensions 250×75 lattice units, $M1$ is the original grid (500×130) and the finer mesh, $M2$, has dimensions 1000×260. In these experiments, the

	$M0$	$M1$	$M2$
C_D	1.58109	1.24633	1.24640
	0.33476	0.00007	

Table 5.2: Computed drag coefficient for flow over a column of cylinders using different meshes and the difference between them.

diameter of the cylinder is always 10. The drag coefficient is measured on each of these grids using the second order interpolation boundary treatment and Table 5.2 shows these results and the difference between adjacent predictions. Mesh $M0$ is clearly too coarse to obtain accurate predictions since the relative difference between the computed drag on this grid and the results of Fornberg [11] is over 25%. We also see that doubling the mesh dimensions from $M1$ to $M2$ does not appear to effect the results.

To study the influence of the confining walls we define the blockage ratio $\Lambda = \frac{D}{W}$, where D is the diameter of the cylinder and W the width of the channel. Although it is well understood that both the Reynolds number and the blockage ratio influence the flow field, only recently has a systematic and quantitative numerical study been conducted [59]. Consider an infinitely long cylinder of diameter D placed halfway between two parallel plates which are a distance W apart (Figure 5.11). A no-slip condition is imposed on the plates and the cylinder boundary, and a parabolic velocity profile specified as the inflow condition. An extrapolation is once again used at the outlet.

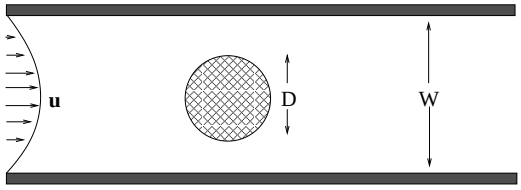

Figure 5.11: Flow domain for cylinder computations.

Table 5.3 shows the computed value of the drag coefficient using the first-order interpolation boundary condition applied to the parallel plates and the cylinder for different Reynolds number and blockage ratios. The initial mesh has dimensions 500×101. Also shown in Table 5.3 are the results of

Sahin [59] and the relative difference between the data sets. We see that the lattice Boltzmann predictions compare well with the novel finite volume method with the difference remaining below 5% for all but one value of Λ and $Re \leq 100$ and in several cases closer agreement was obtained.

Table 5.4 shows the computed value of the drag coefficient using the second-order interpolation boundary condition applied to the parallel plates and the cylinder for different Reynolds number and blockage ratios, along with the results of Sahin [59]. The same mesh as the first-order simulations was used. Again we see that the lattice Boltzmann predictions compare well with the novel finite volume method and notice a reduction in relative difference compared to the first-order case. However, for two results ($Re = 10$, $\Lambda = 0.7$ and $Re = 40$, $\Lambda = 0.2$) the first-order scheme gives a prediction of C_d closer to the value obtained by Sahin. The reason for this is unclear. It is also interesting to note that for each value of Λ the error between the lattice Boltzmann and finite volume predictions reduces as the Reynolds number is increased from $Re = 10$ to $Re = 40$ although the trend does not continue at higher Reynolds numbers. In Figure 5.12 we plot the drag coefficient against Reynolds number for a selection of blockage ratios. The graph emphasises the good agreement between Sahin's results and our predictions using both the first and second order interpolation schemes applied to the no-slip boundaries.

Table 5.5 shows the computed value of the lift coefficient using first and second-order interpolation boundary conditions applied to the parallel plates and the cylinder when $Re = 100$ and $\Lambda = 0.2$, 0.3, along with the results of Sahin [59]. In the table $C_L^{(1)}$ refers to the results obtained using the first order boundary interpolation scheme and $C_L^{(2)}$ is the second order case. The difference column presents the relative difference between Sahin's results [59] and the second order boundary treatment results. We see a decent agreement between the data sets with relative differences similar to those in the drag computations.

An important non-dimensional quantity in the analysis of unsteady flow

Λ	C_D	Sahin [59]	Difference (%)
$Re = 0.1$			
0.2	337.78	324.23	4.2
0.3	585.25	558.04	4.88
0.5	1846.39	1765.3	4.6
0.7	7965.1	8058.0	1.2
$Re = 1$			
0.2	33.913	32.574	4.1
0.3	58.576	55.875	4.8
0.5	187.516	176.56	4.5
0.7	796.513	806.01	1.2
$Re = 10$			
0.2	4.2108	4.1081	2.5
0.3	6.368	6.1464	3.4
0.5	18.976	17.957	5.72
0.7	79.659	80.891	1.28
$Re = 20$			
0.2	2.6631	2.6248	1.46
0.3	3.686	3.6052	2.24
0.5	9.8207	9.3786	4.7
0.7	40.2595	40.174	0.2
$Re = 40$			
0.2	1.8298	1.8264	0.19
0.3	2.3813	2.3644	0.7
0.5	5.4889	5.3470	2.65
0.7	20.8077	21.298	2.3
$Re = 100$			
0.2	1.258	1.322	4.84
0.3	1.5896	1.577	0.8
0.5	3.253	3.1570	3.04
0.7	11.2616	10.782	4.45

Table 5.3: Comparison of drag coefficient for flow over a cylinder using a first order interpolation boundary scheme.

Λ	C_D	Sahin [59]	Difference (%)
$Re = 0.1$			
0.2	335.1	324.23	3.35
0.3	583.632	558.04	4.6
0.5	1840.58	1765.3	4.3
0.7	7939.11	8058	1.5
$Re = 1$			
0.2	33.77	32.544	3.77
0.3	58.415	55.87	4.5
0.5	187.048	176.56	5.9
0.7	799.65	806.01	0.8
$Re = 10$			
0.2	4.1867	4.1081	1.91
0.3	6.345	6.1464	3.2
0.5	18.929	17.957	5.45
0.7	79.602	80.891	1.59
$Re = 20$			
0.2	2.6484	2.6248	0.9
0.3	3.674	6.1464	1.9
0.5	9.7972	9.3786	4.48
0.7	40.1331	40.174	0.1
$Re = 40$			
0.2	1.8174	1.8264	0.49
0.3	2.3714	2.3664	0.3
0.5	5.4761	5.3470	2.41
0.7	20.812	21.298	2.28
$Re = 100$			
0.2	1.297	1.322	1.89
0.3	1.5896	1.577	0.8
0.5	3.236	3.1570	2.5
0.7	11.222	10.782	4.08

Table 5.4: Comparison of drag coefficient for flow over a cylinder using a second order interpolation boundary scheme.

Λ	$C_L^{(1)}$	$C_L^{(2)}$	Sahin [59]	Difference (%)
0.2	0.28	0.2269	0.2231	1.7
0.3	0.099	0.0973	0.0943	3.2

Table 5.5: Comparison of lift coefficient for flow over a cylinder using a first ($C_L^{(1)}$) and second ($C_L^{(2)}$) order interpolation boundary scheme.

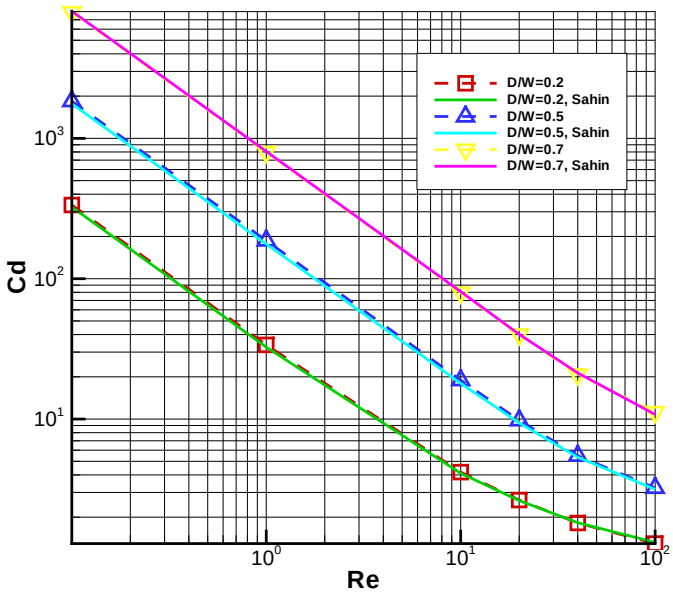

Figure 5.12: Computed drag coefficient versus Reynolds number for $\Lambda = 0.2$, 0.5 and 0.7.

past a body is the Strouhal number, which is defined to be

$$St = \frac{fL}{U}, \tag{5.167}$$

where f is the frequency of the vortex shedding, L is a characteristic length (taken to be the diameter of the cylinder here) and U is the free-stream velocity. The Strouhal number describes the time-dependent behavior of the flow and can be thought of as a measure for the vortex shedding frequency. This quantity is a function of the Reynolds number and previous numerical and experimental work [59] has studied the relation between the two. These two numbers are of great importance in engineering applications where the transition from the steady to the unsteady regime is needed.

To further our study of this model we measure the Strouhal number and once again compare our results against those obtained by Sahin [59]. The

Λ	St	Sahin [59]	Difference %
0.2	0.1795	0.1718	4.4

Table 5.6: Comparison of Strouhal number for flow over a cylinder at $Re = 100$.

shedding frequency is found by plotting the x-component of the centreline velocity and measuring the distance between 'peaks' behind the cylinder. Figure 5.13 plots the x-component of the centerline velocity when $Re = 100$ and $\Lambda = 0.2$. The distance, between peaks above and below the obstacle is approximately $P = 112$, giving a period of shedding $T = P/U = 1866.67$. The frequency, f, is then $f = 1/T$, which is then used to find St. The Strouhal number for this flow is presented in Table 5.6 together with the corresponding results of Sahin [59] and the relative difference between the two.

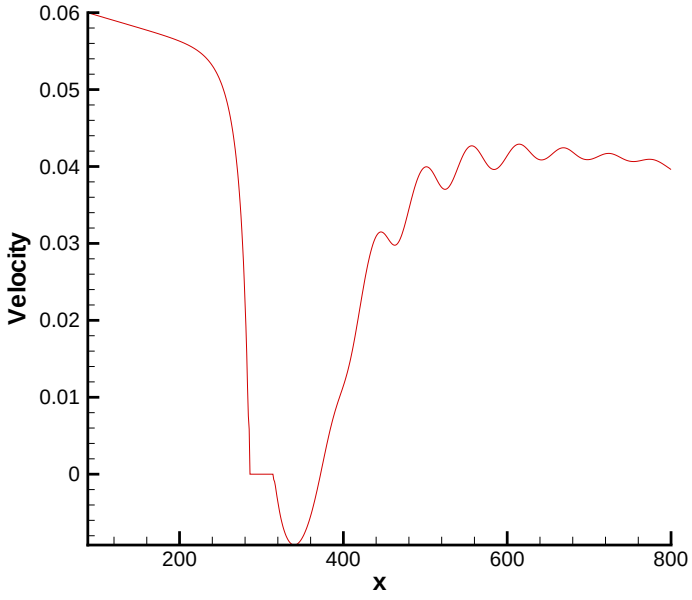

Figure 5.13: Centerline velocity for flow over a confined cylinder at $Re = 100$ and $\Lambda = 0.2$.

To demonstrate mesh convergence we construct four additional meshes,

Λ	$M0$	$M1$	$M2$	$M3$	$M4$	Sahin
0.2	12661	50175	201695	808807	1821255	1727584
0.5	12241	48491	194915	781495	1759719	1612384
0.7	11753	46583	187147	750207	1689311	1554784

Table 5.7: Number of degrees of freedom for the five meshes and Sahin's grid.

one coarser and three finer than the one mentioned above. The coarse grid, $M0$, has dimensions 250×51 lattice units, $M1$ is the original grid (500×101) and the finer meshes, $M2$, $M3$ and $M4$ have dimensions 1000×203, 2000×407 and 3000×611, respectively. Note that the mesh refinement factor is 2 for most cases but mesh $M4$ is not double the size of $M3$ because of computational restrictions. Table 5.7 shows the number of degrees of freedom for each mesh and chosen blockage ratios along with the corresponding number used on Sahin's finest grid. [59].

The drag coefficient is measured on each of these grids using the second order interpolation boundary treatment and Table 5.8 shows these results and the difference between adjacent predictions. We see the difference between computed values of the drag coefficient is approximately the reciprocal of the mesh refinement factor (excluding the results of $M0$), allowing us to estimate the drag on an even finer grid. The difference between computed values is larger at larger blockage ratios, which is to be expected considering the reduction in the number of degrees of freedom. We note that on mesh $M0$ the numerical values for the drag coefficient have a large relative difference compared to the results of Sahin [59] and the pattern of halving the difference is lost. This tells us that grid $M0$ is too coarse to predict meaningful results and a minimum number of nodes is necessary (note that the '/' in Table 5.8 indicates that the code was unable to give a result with these parameters).

Although our mesh refinement study shows convergence of the value of the drag coefficient, the values of the finer meshes have a greater relative difference compared with Sahin's. To check our results are indeed converging we examine the stream-wise velocity at the point $(3nx/4, ny/2)$ in meshes $M1$ to $M4$, where nx and ny are the number of nodal points in the x and y directions, respectively. Table 5.9 shows the velocity at this point on each

	$M0$		$M1$		$M2$		$M3$		$M4$
$Re = 10$									
$\Lambda = 0.2$	/		4.1867		4.118		4.036		4.026
				0.0687		0.082		0.01	
$Re = 10$									
$\Lambda = 0.5$	20.354		18.929		17.978		17.538		17.228
		1.425		0.951		0.44		0.31	
$Re = 10$									
$\Lambda = 0.7$	94.92		79.602		72.777		68.88		65.922
		15.318		6.825		3.897		2.958	
$Re = 40$									
$\Lambda = 0.2$	9.02		1.8174		1.7936		1.7868		1.7814
		7.2026		0.0238		0.0068		0.0054	
$Re = 40$									
$\Lambda = 0.5$	11.056		5.4761		5.2323		5.1198		5.0528
		5.5799		0.2438		0.1125		0.067	
$Re = 40$									
$\Lambda = 0.7$	32.292		20.812		19.018		18.235		17.814
		11.48		1.794		0.783		0.421	

Table 5.8: Computed drag coefficient using different meshes and the difference between them.

	$M1$		$M2$		$M3$		$M4$
$Re = 10$							
$\Lambda = 0.2$	0.01479		0.01407		0.01403		0.01300
		0.00011		0.00004		0.00003	
$Re = 10$							
$\Lambda = 0.5$	0.01441		0.01432		0.01429		0.01427
		0.00009		0.00003		0.00002	
$Re = 10$							
$\Lambda = 0.7$	0.01232		0.01214		0.01196		0.01181
		0.00018		0.00018		0.00015	
$Re = 40$							
$\Lambda = 0.2$	0.03904		0.03834		0.03799		0.03786
		0.00060		0.00034		0.00014	
$Re = 40$							
$\Lambda = 0.5$	0.04781		0.04670		0.04661		0.04651
		0.00111		0.00009		0.00001	

Table 5.9: Computed velocity $u(3nx/4, ny/2)$ using different meshes and the difference between them.

mesh and the difference between adjacent predictions. Although the difference between adjacent values of velocity is rather erratic (that is, there is no obvious pattern between the difference in velocity and the size of the mesh) the results are once again generally showing convergence.

Figure 5.14 plots the streamwise velocity contours for the flow over a cylinder at $Re = 20$ and $\Lambda = 0.2$. We observe the correct flow characteristics of a velocity over-shoot around the leading half of the cylinder and deceleration round the trailing half resulting in zero velocity behind the cylinder. Figure 5.15 plots the streamwise velocity contours for the flow over a cylinder at $Re = 20$ and $\Lambda = 0.7$. We again see the velocity overshoot but also notice the larger acceleration and gradients around the cylinder due to the greater blockage ratio, and see the area of high velocity now follows closely the profile of the obstacle. The streamlines and vectors of this laminar flow are plotted in Figure 5.16 showing how the fluid is forced over the cylinder into a high flow-rate region before returning to a uniform, zero acceleration flow downstream.

Figures 5.17 and 5.18 show the normal (v-component) velocity for $Re =$

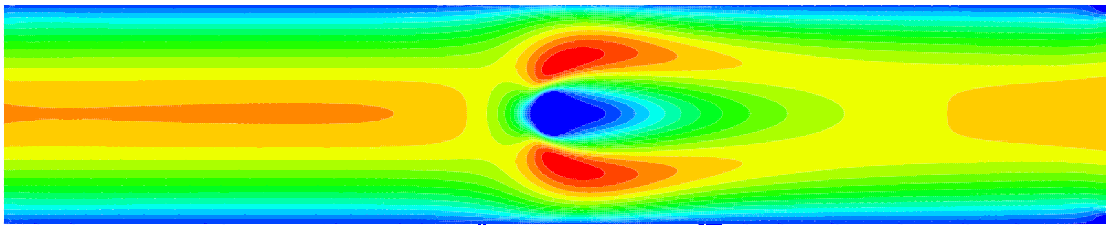

Figure 5.14: Contour plot of streamwise velocity for $Re = 20$ and $\Lambda = 0.2$.

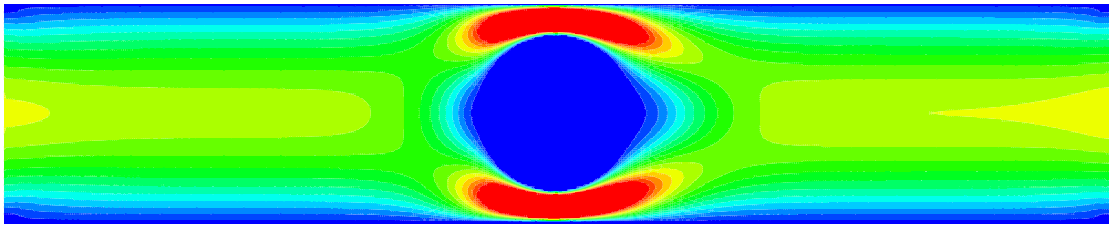

Figure 5.15: Contour plot of streamwise velocity for $Re = 20$ and $\Lambda = 0.7$.

20 and $Re = 100$, respectively, when $\Lambda = 0.7$. In front of the cylinder the contours are similar in both cases. Although the area of non-zero velocity is larger when $Re = 100$ both flows exhibit a region of positive velocity in the upper rear quadrant and a negative region in the lower rear quadrant. Behind the obstacle the flow pattern is quite different with the higher Reynolds number plot showing complex contours that extend far past the cylinder and two smaller vortices developing between them.

As the Reynolds number increases the flow ceases to be stable and the velocity field looses its symmetry. This complex behaviour is shown in Figure

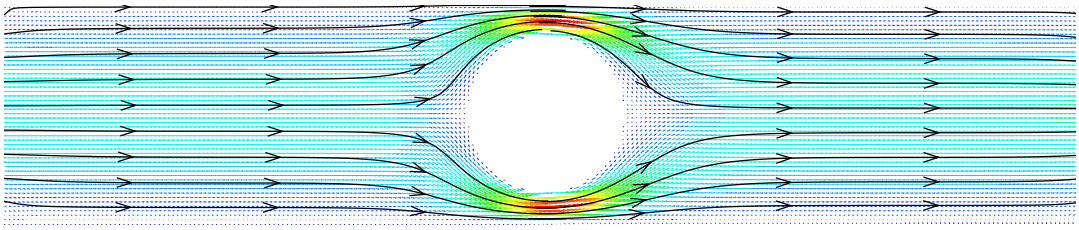

Figure 5.16: Streamlines and vector plot for flow over a cylinder at $Re = 20$ and $\Lambda = 0.7$.

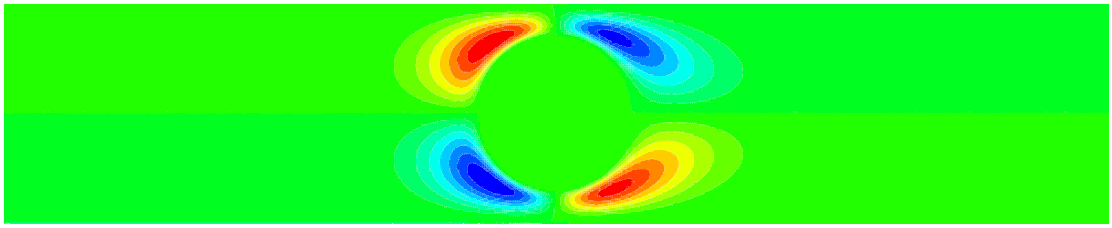

Figure 5.17: Contour plot of normal velocity for $Re = 20$ and $\Lambda = 0.7$.

5.19 which plots the velocity contours in the streamwise direction when $Re = 100$ and $\Lambda = 0.2$. We see a region of negative velocity behind the cylinder and vortex shedding in the wake, giving rise to an oscillating von-Karman street. This phenomenon is clearly observed in Figure 5.20 and Figure 5.21 which plot the streamlines of this flow and show the familiar pair of trailing vortices. The normal velocity is plotted in Figure 5.22, giving further evidence of the periodic shedding in the cylinder wake.

As the blockage ratio increases to 0.7 (with $Re = 100$) the flow around the free end suppresses the von-Karman vortex shedding, as shown in Figure 5.23, and symmetry and stability is preserved. We plot the streamlines in

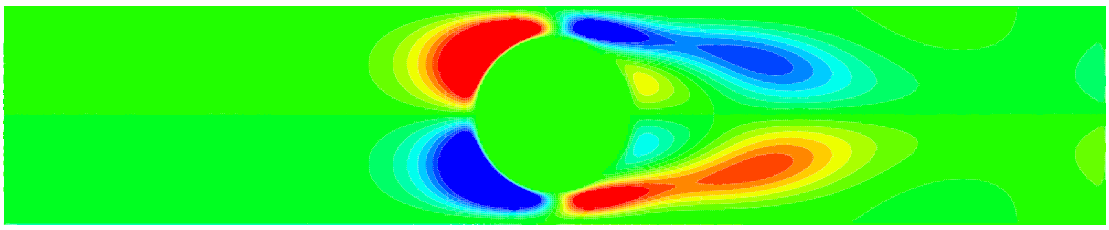

Figure 5.18: Contour plot of normal velocity for $Re = 100$ and $\Lambda = 0.7$.

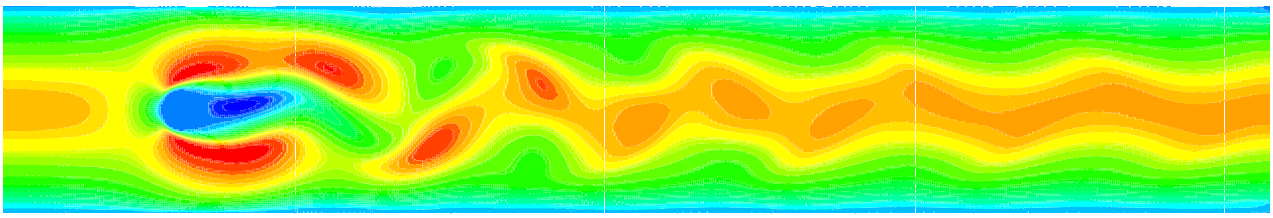

Figure 5.19: Contour plot of streamwise velocity for $Re = 100$ and $\Lambda = 0.2$.

Figure 5.24 and magnify the image behind the obstacle in Figure 5.25. We notice a pair of arch vortices form in the near-wake before returning to a uniform, zero acceleration flow further downstream.

5.7 Discussion

In this chapter we defined the lattice Boltzmann equation and have shown, via a Chapman-Enskog analysis, that it is a second order approximation to the Navier-Stokes equations. An alternative approach to the solution of the dispersion relation for the generalised lattice Boltzmann equation is

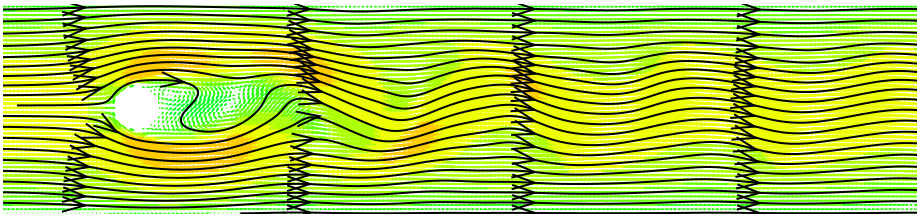

Figure 5.20: Streamlines and vector plot for flow over a cylinder at $Re = 100$ and $\Lambda = 0.2$.

presented and a journal article containing this development is in preparation [51]. A survey of different boundary treatments has been presented with some numerical results for laminar Poiseuille flow and flow over a column of cylinders that verify our code and the improved interpolation scheme for the no-slip boundary condition of Yu et al. [71].

We have also studied the flow over a confined cylinder in a channel and examined the lattice Boltzmann equation's ability to predict the drag coefficient at a variety of Reynolds numbers and blockage ratios. Our results show that the LBE measurements compare well with those recently obtained using a novel finite volume approach [59] with a relative difference usually below 3%. Considering no grid refinement around the obstacle was used we believe these results to be encouraging for a first systematic study of the influence of the Reynolds number and blockage ratio using a lattice Boltzmann model. By refining the computational grid we have also been able to demonstrate second order convergence for the drag coefficient. However, a number of our results are somewhat puzzling and counter-intuitive. It is, for example, unclear at this stage why the error reduces with an increase in blockage ratio for some values of Re. In some situations the error is below 1% where in others it is closer to 5% and there appears to be no obvious relation between the error and the flow parameters. Also, although our study of mesh refinement shows convergence, in some cases the relative difference between these results and Sahin's increases as the mesh size increases. A possible explanation for

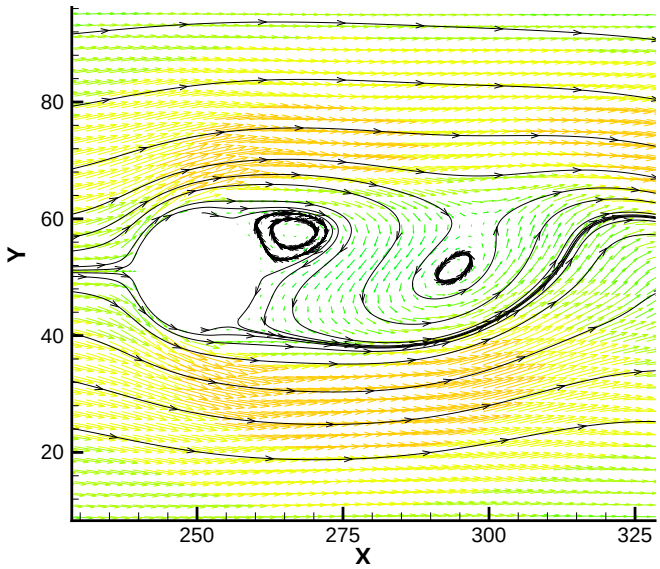

Figure 5.21: Magnified view of streamlines and vector plot for flow over a cylinder at $Re = 100$ and $\Lambda = 0.2$.

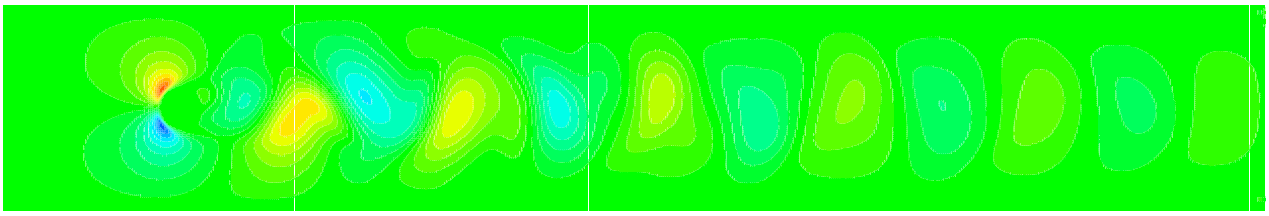

Figure 5.22: Contour plot of normal velocity for $Re = 100$ and $\Lambda = 0.2$.

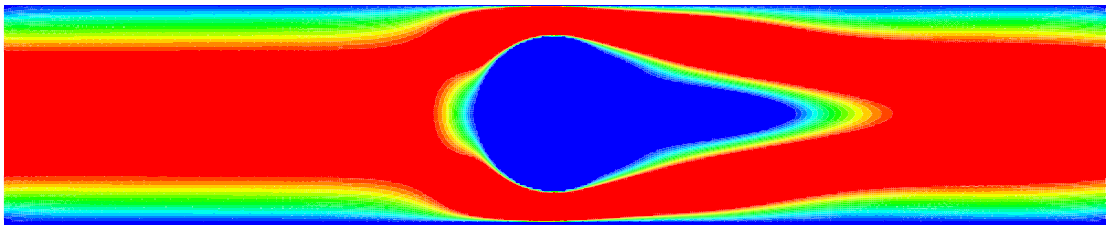

Figure 5.23: Contour plot of streamwise velocity for $Re = 100$ and $\Lambda = 0.7$.

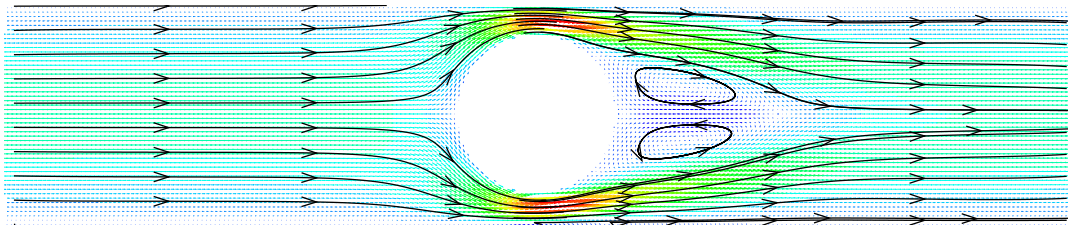

Figure 5.24: Streamlines and vector plot for flow over a cylinder at $Re = 100$ and $\Lambda = 0.7$.

the two mentioned peculiarities is the distance between the centre of the cylinder and the outlet (and inlet) was not constant in these simulations but was in Sahin [59]. To increase the blockage ratio we increased the radius of the cylinder while keeping the grid size constant. Therefore, the inflow and outflow conditions may influence the flow differently for different blockage ratio's; a problem that does not occur in [59].

Finally, an investigation of the velocity field has shown that the relatively simple lattice Boltzmann model is sufficiently detailed to capture the characteristics of this complex flow. The graphs of behaviour of the fluid in the wake of the cylinder presented above show the expected development of a von-Karman street at high Reynolds number and low blockage ratio and a pair of vortices in the near-wake at high Reynolds number and high blockage ratio. A journal article for this study is currently in preparation [52].

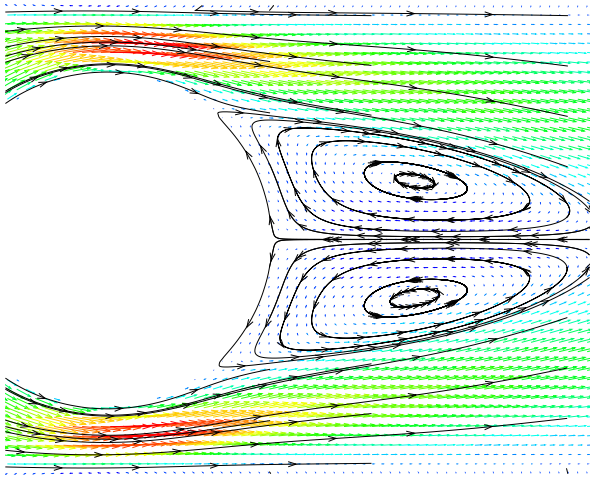

Figure 5.25: Magnified view of streamlines and vector plot for flow over a cylinder at $Re = 100$ and $\Lambda = 0.7$.

Chapter 6

Axisymmetric Flow

The formulation of the standard lattice Boltzmann model for predicting the flow of incompressible fluids is based on the Cartesian coordinate system. However, numerous important flow problems exist for which there is axial symmetry e.g. flow past a cylinder or sphere in a confined channel. The computational demand required for three-dimensional lattice Boltzmann models is considerably greater than for the 2D case. Therefore an axisymmetric LBM, which will only depend on two coordinates, is highly desirable since it makes computational sense to take advantage of any reduction in dimension that can be accrued from geometrical considerations. Alternatively, a reduction in dimensionality also allows for greater spatial refinement through the availability of additional degrees of freedom that would have been required in the third dimension.

Halliday et al. [18] demonstrated how the evolution equation for the momentum distribution function within a 2D Cartesian framework may be adjusted by adding suitable source terms in order to recover the axisymmetric Navier-Stokes equations in the macroscopic limit. The first and second order terms in an expansion of the source term are chosen so that the terms in the lattice continuity and momentum equations, respectively, arising from the cylindrical polar coordinate system are recovered. Premnath and Abraham [49] adopted a similar approach for multiphase flows by including temporally and spatially dependent source terms to account for the axisymmetric

contributions of the order parameter of the fluid phases and inertial, viscous and surface tension forces.

In this section we follow the general philosophy embodied in the paper of Halliday et al. [18] but depart from it in the way that that the second order contribution to the source term is chosen in the recovery of the lattice momentum equation. In this method, the first and second order contributions to the source term are derived through a Chapman-Enskog analysis. The analysis detailed here is performed consistently within the Chapman-Enskog formalism, unlike previously adopted approaches. Furthermore, the form of the source terms that are derived here allow for a more efficient implementation of the LBM for axisymmetric flow problems due to the reduction in the number of terms that require numerical differentiation. The validity of the model is confirmed with a number of benchmark simulations. The theoretical development of this alternative model has been published in [55] and an article containing the numerical evaluation of the model is in preparation [53].

6.1 Governing Equations in Axisymmetric Geometries

Consider the flow of an incompressible, isotropic fluid through a three-dimensional pipe. Let $\mathbf{e}_r$, $\mathbf{e}_\theta$ and $\mathbf{e}_z$ be the standard orthonormal unit vectors defining a cylindrical coordinate system:

$$\mathbf{e}_r = \left(\frac{x}{r}, \frac{y}{r}, 0\right), \quad \mathbf{e}_\theta = \left(\frac{y}{r}, -\frac{x}{r}, 0\right), \quad \mathbf{e}_z = (0, 0, 1)\,; \tag{6.1}$$

where $r = \sqrt{x^2 + y^2}$, $x = r\cos\theta$ and $y = r\sin\theta$. If the solution to the Navier-Stokes equation is of the form

$$\mathbf{u} = u_r(r, z)\mathbf{e}_r + u_z(r, z)\mathbf{e}_z, \tag{6.2}$$

that is the velocity field does not depend on θ, then the flow is said to be axisymmetric (without swirl). The continuity equation in cylindrical coordi-

nates is

$$\frac{\partial u_r}{\partial r} + \frac{u_r}{r} + \frac{\partial u_z}{\partial z} = 0, \tag{6.3}$$

and the components of the momentum equation are:

$$\begin{aligned} \frac{\partial u_r}{\partial t} + u_r\frac{\partial u_r}{\partial r} + u_z\frac{\partial u_r}{\partial z} &= -\frac{1}{\rho}\frac{\partial P}{\partial r} \\ &\quad +\nu\left(\frac{\partial^2 u_r}{\partial r^2} + \frac{1}{r}\frac{\partial u_r}{\partial r} - \frac{u_r}{r^2} + \frac{\partial^2 u_r}{\partial z^2}\right), \end{aligned} \tag{6.4}$$

$$\begin{aligned} \frac{\partial u_z}{\partial t} + u_r\frac{\partial u_z}{\partial r} + u_z\frac{\partial u_z}{\partial z} &= -\frac{1}{\rho}\frac{\partial P}{\partial z} \\ &\quad +\nu\left(\frac{\partial^2 u_z}{\partial r^2} + \frac{1}{r}\frac{\partial u_z}{\partial r} + \frac{\partial^2 u_z}{\partial z^2}\right), \end{aligned} \tag{6.5}$$

where ν is the kinematic viscosity.

By performing the following coordinate transformation:

$$(r, z) \mapsto (y, x), \tag{6.6}$$

$$(u_r, u_z) \mapsto (u_y, u_x); \tag{6.7}$$

equations (6.3)-(6.5) can be written in Cartesian-like coordinates:

$$\partial_\alpha u_\alpha = -\frac{u_y}{y}, \tag{6.8}$$

$$\frac{D\rho u_\alpha}{Dt} + \partial_\alpha P - \nu\rho\nabla^2 u_\alpha = \frac{\nu\rho}{y}\partial_y u_\alpha - \frac{\nu\rho u_\alpha}{y^2}\delta_{\alpha y}, \tag{6.9}$$

where D/Dt is the material derivative, $\delta_{\alpha\beta}$ is the Kronecker delta function and $\alpha = x, y$. The terms on the right-hand side of the momentum equation (6.9) are the additional axisymmetric contributions that the source terms need to recover.

6.2 Axisymmetric LBE

To apply the lattice Boltzmann equation to a range of flow problems, an internal or external force term may need to be added to equation (5.12). The exact form of this term depends on the mechanics in question, for example

particle-fluid suspensions [29], multi-phase flows [6, 15, 63], viscoelastic fluids [27], or flow in an axisymmetric geometry [18]. A general representation of forcing terms within the LBE framework that considers discrete lattice effects has been proposed by Guo et al. [17]. With the intention of deriving equations (6.8)-(6.9), a spatial and temporal microscopic term, $S_i(\mathbf{x}, t)$, is introduced into the D2Q9 lattice Boltzmann equation [18, 49]:

$$N_i(\mathbf{x} + \mathbf{c}_i, t + 1) = N_i(\mathbf{x}, t) + \omega \left[N_i^{(0)}(\mathbf{x}, t) - N_i(\mathbf{x}, t) \right] + S_i(\mathbf{x}, t), \quad (6.10)$$

and we take this source term to be at least $O(\epsilon)$:

$$S_i = \epsilon S_i^{(1)} + \epsilon^2 S_i^{(2)} + \cdots , \quad (6.11)$$

that is, there is no equilibrium S_i term.

The aim now is to perform a Taylor and Chapman-Enskog expansion on equation (6.10) and choose S_i in such a way to recover equations (6.3), (6.4) and (6.5). To first order in ϵ we obtain:

$$\partial_{t_1} N_i^{(0)} + c_{i\alpha} \partial_\alpha N_i^{(0)} = -\omega N_i^{(1)} + S_i^{(1)}, \quad (6.12)$$

and the mass and momentum constraints yield

$$\partial_{t_1} \rho + \partial_\alpha \rho u_\alpha = \sum_{i=0}^{8} S_i^{(1)}, \quad (6.13)$$

$$\partial_{t_1} \rho u_\alpha + \partial_\beta \Pi_{\alpha\beta} = \sum_{i=0}^{8} S_i^{(1)} c_{i\alpha}, \quad (6.14)$$

respectively, where $\Pi_{\alpha\beta} = \sum_{i=0}^{8} N_i^{(0)} c_{i\alpha} c_{i\beta}$ is the momentum flux tensor. To recover the continuity equation (6.3) we, like Halliday et al. [18], choose the first order source term to be:

$$S_i^{(1)} = -\frac{W_i \rho u_y}{y}, \quad (6.15)$$

where the weights, W_i, $i = 0, \ldots, 8$, are given by equation (5.28). Note that

$$\sum_{i=0}^{8} S_i^{(1)} = -\frac{\rho u_y}{y}, \tag{6.16}$$

$$\sum_{i=0}^{8} S_i^{(1)} c_{i\alpha} = 0. \tag{6.17}$$

Our analysis now differs from previous derivations of axisymmetric LBM's in the following way. Halliday et al. [18] and Premnath and Abraham [49] borrow the $O(\epsilon)$ terms in the expansion of the evolution equation from the unadjusted LBGK equation to find at second order in ϵ:

$$\partial_{t_2} N_i^{(0)} + (\partial_{t_1} + c_{i\alpha}\partial_\alpha)\left(1 - \frac{\omega}{2}\right) N_i^{(1)} = -\omega N_i^{(2)} + S_i^{(2)}. \tag{6.18}$$

We argue that the $S_i^{(1)}$ term plays a greater role in the expansion, thus changing the form of $S_i^{(2)}$.

At order ϵ^2 we obtain

$$\begin{aligned} &\partial_{t_2} N_i^{(0)} + \partial_{t_1} N_i^{(1)} + c_{i\alpha}\partial_\alpha N_i^{(1)} + \frac{1}{2}\partial_{t_1}\partial_{t_1} N_i^{(0)} \\ &+ c_{i\alpha}\partial_{t_1}\partial_\alpha N_i^{(0)} + \frac{1}{2} c_{i\alpha} c_{i\beta}\partial_\alpha\partial_\beta N_i^{(0)} = -\omega N_i^{(2)} + S_i^{(2)}. \end{aligned} \tag{6.19}$$

If, using equations (6.12) and (6.15), we write the above in a similar form to Halliday et al. [18] and Premnath and Abraham [49], i.e.

$$\begin{aligned} &\partial_{t_2} N_i^{(0)} + (\partial_{t_1} + c_{i\alpha}\partial_\alpha)\left(1 - \frac{\omega}{2}\right) N_i^{(1)} \\ &\quad - (\partial_{t_1} + c_{i\alpha}\partial_\alpha)\frac{W_i \rho u_y}{2y} = -\omega N_i^{(2)} + S_i^{(2)}, \end{aligned} \tag{6.20}$$

we see the presence of additional terms involving $S_i^{(1)}$ which are missing in the article of Halliday et al [18]. More precisely, the coupling of the two source terms occurs through the non-equilibrium part of the distribution function, $N_i^{(1)}$. Substituting equation (6.12) into equation (6.20) (or alternatively, equation (6.19)) yields the following axisymmetric terms that are not present

in the unadjusted LBGK equation:

$$-\frac{1}{\omega}\left(\partial_{t_1}+c_{i\alpha}\partial_\alpha\right)\frac{W_i\rho u_y}{y}-S_i^{(2)}=\frac{1}{\omega}\left(\partial_{t_1}+c_{i\alpha}\partial_\alpha\right)S_i^{(1)}-S_i^{(2)}. \tag{6.21}$$

Comparing this with the expression (17) in Halliday et al. [18], we see that our second order axisymmetric contribution does not include the $-S_i^{(1)}/2$ term. We suggest that (6.21) is the correct form for the expanded LBGK expression with an additional geometrical force term and note that equation (6.20) is consistent with the generalised expansion of LBGK equations with additional forces, as described in [17].

Applying the mass conservation constraint to equation (6.19) gives:

$$\partial_{t_2}\rho+\frac{1}{2}\partial_{t_1}\partial_{t_1}\rho+\partial_{t_1}\partial_\alpha\rho u_\alpha+\frac{1}{2}\partial_\alpha\partial_\beta\Pi_{\alpha\beta}=\sum_{i=0}^{8}S_i^{(2)}, \tag{6.22}$$

and upon using equations (6.13) and (6.14) we find that

$$\partial_{t_2}\rho-\frac{1}{2}\partial_{t_1}\frac{\rho u_y}{y}=\sum_{1=0}^{8}S_i^{(2)}. \tag{6.23}$$

Adding the above equation to equation (6.13) shows that

$$\partial_t\rho+\partial_\alpha\rho u_\alpha=-\frac{\rho u_y}{y}+\frac{1}{2}\partial_{t_1}\frac{\rho u_y}{y}+\sum_{i=0}^{8}S_i^{(2)}, \tag{6.24}$$

so to recover the correct continuity equation we require

$$\sum_{i=0}^{8}S_i^{(2)}=-\frac{1}{2y}\partial_{t_1}\rho u_y=\frac{1}{2y}\partial_\alpha\Pi_{\alpha y}. \tag{6.25}$$

When the momentum conservation constraint is applied to equation (6.19) we find the following equality:

$$\partial_{t_2}\rho u_\alpha+\partial_\beta Q_{\alpha\beta}+\frac{1}{2}\partial_{t_1}\partial_{t_1}\rho u_\alpha+\partial_{t_1}\partial_\beta\Pi_{\alpha\beta}+\frac{1}{2}\partial_\beta\partial_\gamma P_{\alpha\beta\gamma}=\sum_{i=0}^{8}S_i^{(2)}c_{i\alpha}, \tag{6.26}$$

where $Q_{\alpha\beta} = \sum_{i=0}^{8} N_i^{(1)} c_{i\alpha} c_{i\beta}$ and $P_{\alpha\beta\gamma} = \sum_{i=0}^{8} N_i^{(0)} c_{i\alpha} c_{i\beta} c_{i\gamma}$. This equation can be simplified using equation (6.14) to give

$$\partial_{t_2} \rho u_\alpha + \partial_\beta Q_{\alpha\beta} + \frac{1}{2} \partial_{t_1} \partial_\beta \Pi_{\alpha\beta} + \frac{1}{2} \partial_\beta \partial_\gamma P_{\alpha\beta\gamma} = \sum_{i=0}^{8} S_i^{(2)} c_{i\alpha}, \tag{6.27}$$

where, from equation (6.12),

$$Q_{\alpha\beta} = -\frac{1}{\omega} \left(\partial_{t_1} \Pi_{\alpha\beta} + \partial_\gamma P_{\alpha\beta\gamma} + \frac{\rho u_y}{3y} \delta_{\alpha\beta} \right). \tag{6.28}$$

For a D2Q9 lattice the tensors $\mathbf{\Pi}$ and $\mathbf{P}$ are found to have the following form:

$$\Pi_{\alpha\beta} = \frac{\rho}{3} \delta_{\alpha\beta} + \rho u_\alpha u_\beta, \tag{6.29}$$

$$P_{\alpha\beta\gamma} = \frac{\rho u_\alpha}{3} \left(u_\gamma \delta_{\alpha\beta} + u_\beta \delta_{\alpha\gamma} + u_\alpha \delta_{\beta\gamma} \right) \tag{6.30}$$

A little algebra now shows that equation (6.27) may be written as

$$\partial_{t_2} \rho u_\alpha - \nu \left(\partial_\alpha \partial_\alpha \rho u_\alpha + \partial_\alpha \partial_\beta \rho u_\beta + \partial_\alpha \frac{\rho u_y}{y} - 2 \partial_\alpha \frac{\rho u_y}{y} \right)$$
$$- \frac{1}{3\omega} \partial_\alpha \frac{\rho u_y}{y} = \sum_{i=0}^{8} S_1^{(2)} c_{i\alpha}, \tag{6.31}$$

where

$$\nu = \frac{1}{3} \left(\frac{1}{\omega} - \frac{1}{2} \right)$$

is the kinematic viscosity. If we assume the fluid is incompressible then equation (6.13) tells us that

$$\partial_\alpha \partial_\beta \rho u_\beta + \partial_\alpha \frac{\rho u_y}{y} = 0, \tag{6.32}$$

which allows us to write equation (6.31) as

$$\partial_{t_2} \rho u_\alpha - \nu \partial_\alpha \partial_\alpha \rho u_\alpha = \sum_{i=0}^{8} S_i^{(2)} c_{i\alpha} - 2\nu \partial_\alpha \frac{\rho u_y}{y} + \frac{1}{3\omega} \partial_\alpha \frac{\rho u_y}{y}. \tag{6.33}$$

Summing the first and second order momentum equations yields:

$$\partial_t \rho u_\alpha + \partial_\beta \Pi_{\alpha\beta} - \nu \partial_\alpha \partial_\alpha \rho u_\alpha = \sum_{i=0}^{8} S_i^{(2)} c_{i\alpha} - 2\nu \partial_\alpha \frac{\rho u_y}{y} + \frac{1}{3\omega} \partial_\alpha \frac{\rho u_y}{y}, \quad (6.34)$$

and using equation (6.29) we find the momentum equation to be

$$\rho \left(\partial_t u_\alpha + u_\beta \partial_\beta u_\alpha \right) + \partial_\alpha P - \rho\nu \partial_\beta \partial_\beta u_\alpha = \sum_{i=0}^{8} S_i^{(2)} c_{i\alpha} - 2\nu \partial_\alpha \frac{\rho u_y}{y} + \frac{1}{3\omega} \partial_\alpha \frac{\rho u_y}{y} + u_\alpha \frac{\rho u_y}{y}, \quad (6.35)$$

where the left-hand side contains the terms in the standard Navier-Stokes equations and the terms on the right-hand side must deliver the extra axisymmetric contributions. Looking at the components of the above momentum equation and the second order mass equation we see that $S_i^{(2)}$ must conform to the following three conditions:

$$\sum_{i=0}^{8} S_i^{(2)} = \frac{1}{2y} \partial_\beta \Pi_{y\beta}, \quad (6.36)$$

$$\sum_{i=0}^{8} S_i^{(2)} c_{ix} = \frac{\rho\nu}{y} \left(\partial_y u_x + \partial_x u_y \right) - \frac{\rho}{6y} \partial_x u_y - \frac{\rho u_x u_y}{y}, \quad (6.37)$$

$$\sum_{i=0}^{8} S_i^{(2)} c_{iy} = \frac{1}{y} \left(2\nu - \frac{1}{6} \right) \left(\partial_y u_y - \frac{u_y}{y} \right) - \frac{\rho u_y^2}{y}. \quad (6.38)$$

To simplify the above relations and follow the the lattice Boltzmann methodology as closely as possible we try to relate $S_i^{(2)}$ to moments of the distribution function. Recalling that

$$\begin{aligned} Q_{\alpha\beta} &= -\frac{1}{\omega} \left(\partial_{t_1} \Pi_{\alpha\beta} + \partial_\gamma P_{\alpha\beta\gamma} + \frac{\rho u_y}{3y} \delta_{\alpha\beta} \right), \\ &= -\frac{\rho}{3\omega} \left(\partial_\alpha u_\beta + \partial_\beta u_\alpha \right), \end{aligned} \quad (6.39)$$

enables us to find most of the required gradients in terms of the moments of

$N_i^{(1)}$:

$$\frac{\nu\rho}{y}\left(\partial_x u_y + \partial_y u_x\right) = -\frac{6\nu}{(6\nu+1)y}\sum_{i=0}^{8} N_i^{(1)} c_{ix} c_{iy}, \tag{6.40}$$

$$\frac{1}{y}\left(2\nu - \frac{1}{6}\right)\left(\partial_y u_y - \frac{u_y}{y}\right) = \frac{(1-12\nu)}{y}\left[\frac{1}{2(1+6\nu)}\sum_{i=0}^{8} N_i^{(1)} c_{iy}^2 + \frac{\rho u_y}{y}\right].$$

A suitable choice of $S_i^{(2)}$ can now be found by inspection. Given below are our first and second order source terms that meet the required conditions (6.36), (6.37) and (6.38) and therefore recover the axisymmetric Navier-Stokes equations in the macroscopic limit:

$$S_i^{(1)} = -\frac{W_i \rho u_y}{y}, \tag{6.41}$$

$$\begin{aligned} S_i^{(2)} = \frac{3W_i}{y}\Bigg[& \frac{c_{iy}^2}{2}\left(u_x\partial_x u_y - \frac{3u_y\omega}{2}Q_{xx} - 3u_y\omega Q_{yy} - \frac{\rho u_y^2}{y}\right) \\ & - c_{ix}\left(\frac{6\nu}{6\nu+1}Q_{xy} + \frac{\rho}{6}\partial_x u_y - \rho u_x u_y\right) \\ & + c_{iy}(1-12\nu)\left(\frac{1}{2(1+6\nu)}Q_{yy} + \frac{\rho u_y}{y} - \rho u_y^2\right)\Bigg] \end{aligned} \tag{6.42}$$

The differences between our model and that of Halliday et al. [18] should now be highlighted. Our second-order source term is given mainly in terms of the tensor $\mathbf{Q}$, which is the third moment of the non-equilibrium distribution function, $N_i^{(ne)}$. Therefore, we argue that this derivation is more sympathetic to the lattice Boltzmann philosophy. Another advantage of this approach is the reduction in the amount of numerical differentiation that needs to be performed compared to the lattice Boltzmann models of Halliday et. al [18] and Premnath and Abraham [49]. In the modified LBM described here, only one term viz. $\partial_x u_y$ in the expression for $S_i^{(2)}$ needs to be approximated using finite differences compared with five terms in [18]. Although Halliday et al. [18] comment that components of the velocity gradient tensor can, in principle, be evaluated from appropriate higher order moments of the non-equilibrium function, in practice we are of the opinion that it is not possible

to express $\partial_x u_y$ in this manner. Finally, the analysis performed here is of the same form and to the same order as that presented in [18] but delivered in a different manner. We argue that this method is more transparent than that of Halliday et al. and exposes an additional term in their second order expansion of the evolution equation. The analysis performed in this paper is consistent within the Chapman-Enskog analysis and the general form of LBE equations with additional forcing given by Guo et al. [17]. We note that along the axisymmetric line, i.e. $y = 0$, the singular source terms of type $1/y$ are evaluated using L'Hôpital's rule. After applying this formula we are only left with terms contain a factor of either $\partial_y(\cdot)$ or u_y. Since $u_y(0) = 0$ and all resulting derivatives evaluated at $y = 0$ are zero the terms $S_i(0) = 0$ and therefore we only need to compute S_i from $y = 1$ to $y = H$.

6.3 Hagen-Poiseuille Flow

We verify our model by simulating flows for which there are known exact solutions. The exact solution, $U(r)$, of the axisymmetric Navier-Stokes equations (6.3)-(6.5) to the steady, laminar flow of a viscous fluid through a pipe of radius a is found to be

$$U(r) = U_0 \left(1 - \frac{r^2}{a^2}\right), \tag{6.43}$$

where

$$U_0 = \frac{Ga^2}{4\nu\rho} \tag{6.44}$$

is the maximum velocity in the pipe and G is the pressure gradient.

We construct a 256×64 D2Q9 lattice domain with a line of symmetry at $y = 0$ and a solid wall at $y = 64$. The no-slip boundary condition is applied to the wall using the interpolation scheme, as described in Section 5.5.2. We impose an inflow and outflow condition as detailed in Section 5.5.2 with maximum velocity $U_0 = 0.5$.

Figure 6.1 plots the analytical solution (solid line) and the numerical predictions for Hagen-Poiseuille flow. The graph shows a very good agree-

ment between the analysis and numerics, thus confirming the validity of the axisymmetric lattice Boltzmann equation proposed in Section 6.2.

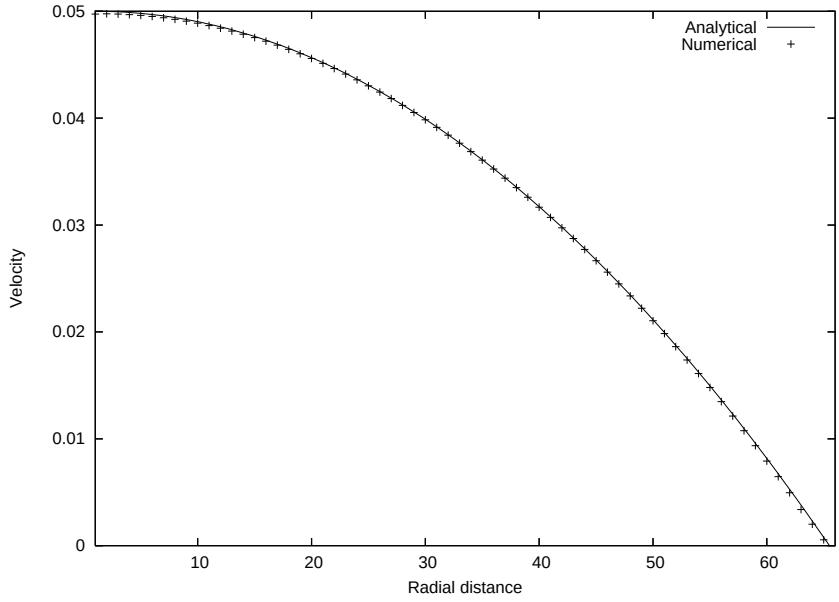

Figure 6.1: Analytical and numerical solutions for Hagen-Poiseuille flow.

6.4 Stokes' Flow over a Sphere

Consider the flow of an incompressible, viscous fluid around a sphere. If the Reynolds number, which we define to be

$$Re = \frac{UD}{\nu}, \tag{6.45}$$

where D is the diameter of the sphere and U is the free-stream velocity, is small (typically $Re \ll 1$) then Stokes' law is valid for the drag force, F_D, on the sphere [31]:

$$F_D = 3\pi\mu DU, \tag{6.46}$$

where μ is the shear viscosity of the fluid. The drag coefficient, C_D is defined as:

$$C_D = \frac{F_D}{0.5\rho U^2 A}, \tag{6.47}$$

where A is the projected area of the obstacle in the plane perpendicular to the flow. For Stokes' flow over a sphere,

$$A = \frac{\pi D^2}{4}, \tag{6.48}$$

so the coefficient of drag is

$$C_D = \frac{24}{Re}. \tag{6.49}$$

In this section we compute the drag coefficient using our axisymmetric lattice Boltzmann model and compare the results with the approximation given by equation (6.49).

We construct a $L \times H$ D2Q9 lattice domain with a line of symmetry at $y = 0$ and place a sphere of radius r at $(x = L/2, y = 0)$, as shown in Figure 6.2. Since the flow is symmetric about $y = 0$ the sphere is represented by a semi-circle. The interpolation scheme, as described in Section 5.5.2, is used to apply the boundary condition. As equation (6.49) is valid in an infinite domain we apply symmetry conditions at the north and south boundaries and specify a uniform velocity, U, at the inlet.

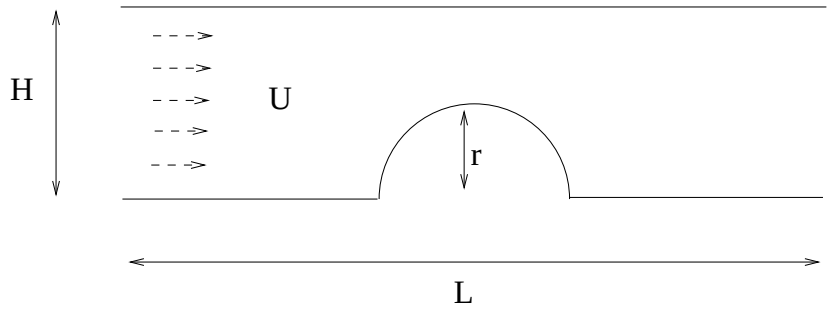

Figure 6.2: Computational domain for axisymmetric flow over a sphere.

Table 6.1 shows, to two decimal places, the computed drag coefficient ($\bar{C}_D$) using a first order interpolation boundary scheme, the Stokes approx-

imation for the drag and the relative difference between the two for different Reynolds numbers. To determine whether or not different flow parameters affect the computation we calculated the drag coefficient twice for each Reynolds number, changing the diameter of the sphere and the fluid viscosity while keeping the velocity $U = Re/100$. In all simulations we kept $L/H = 5$ and $r/H = 0.3$. We note the excellent agrement between the analytical formula for the drag coefficient and the lattice Boltzmann predictions for all $Re < 0.5$.

Table 6.2 shows the computed drag coefficient ($\bar{C}_D$) using a second order interpolation boundary scheme, the Stokes approximation for the drag and the relative difference between the two for different Reynolds numbers. The agreement between the data is seen to be excellent with a difference between the analytical and numerical results often below 0.1%. We also observe the similarity between the lattice Boltzmann results obtained with the first and second order interpolation boundary schemes, indicating that the first order treatment is sufficient to capture the hydrodynamics of this low Reynolds number, laminar flow. Figures 6.4 and 6.5 plot the stream-wise and normal velocity contours, respectively, for the axisymmetric flow over a sphere at $Re = 0.01$. The plots show the expected characteristics associated with this flow, including symmetry of the velocity field, decaying axial velocity approaching the sphere, and a positive radial velocity in front of the sphere and a negative one behind.

From Tables 6.1 and 6.2 we see that as the Reynolds number increases beyond 0.5 the relative difference between the approximations gradually increases. This is to be expected since Stokes' formula (6.49) is only valid when the inertia terms in the Navier-Stokes equations can be neglected, i.e. when the Reynolds number is small. When Re is large the following empirical formula for the drag coefficient on a sphere has been suggested [3]:

$$C_D = \left(\sqrt{\frac{24}{Re}} + 0.5407 \right)^2 . \tag{6.50}$$

Table 6.3 shows the drag coefficient found by equation (6.50) and the nu-

Re	D	$\bar{C}_D$	$C_D = 24/Re$	Difference (%)
0.01	40	2400.41	2400	0.017
0.01	60	2402.03	2400	0.096
0.03	40	800.17	800	0.021
0.03	60	800.78	800	0.98
0.05	40	480.13	480	0.027
0.05	60	480.49	480	0.103
0.07	40	342.96	342.86	0.029
0.07	60	343.11	342.86	0.073
0.09	40	266.77	266.67	0.037
0.09	60	266.95	266.67	0.105
0.1	40	240.10	240	0.042
0.1	60	240.25	240	0.104
0.2	40	120.10	120	0.083
0.2	60	120.15	120	0.125
0.3	40	80.11	80	0.138
0.3	60	80.12	80	0.150
0.5	40	48.14	48	0.292
0.5	60	48.12	48	0.250
0.7	40	34.46	34.29	0.496
0.7	60	34.42	34.29	0.379
1	40	24.23	24	0.958
1	60	24.16	24	0.667
2	40	12.39	12	3.250
2	60	12.29	12	2.417
3	40	8.54	8	6.750
3	60	8.41	8	5.125

Table 6.1: Comparison of drag coefficient for axisymmetric flow over a sphere using a first order interpolation boundary scheme.

Re	D	$\bar{C}_D$	$C_D = 24/Re$	Difference (%)
0.01	40	2400.42	2400	0.018
0.01	60	2402.01	2400	0.084
0.03	40	800.17	800	0.021
0.03	60	800.76	800	0.095
0.05	40	480.14	480	0.029
0.05	60	480.49	480	0.103
0.07	40	342.95	342.86	0.029
0.07	60	343.1	342.86	0.070
0.09	40	266.76	266.67	0.034
0.09	60	266.295	266.67	0.105
0.1	40	240.1	240	0.042
0.1	60	240.25	240	0.104
0.2	40	120.10	120	0.08
0.2	60	120.14	120	0.117
0.3	40	80.12	80	0.150
0.3	60	80.12	80	0.150
0.5	40	48.15	48	0.313
0.5	60	48.12	48	0.250
0.7	40	34.46	34.29	0.496
0.7	60	34.42	34.29	0.379
1	40	24.22	24	0.917
1	60	24.17	24	0.708
2	40	12.40	12	3.333
2	60	12.27	12	2.50
3	40	8.54	8	6.750
3	60	8.41	8	5.125

Table 6.2: Comparison of drag coefficient for axisymmetric flow over a sphere using a second order interpolation boundary scheme.

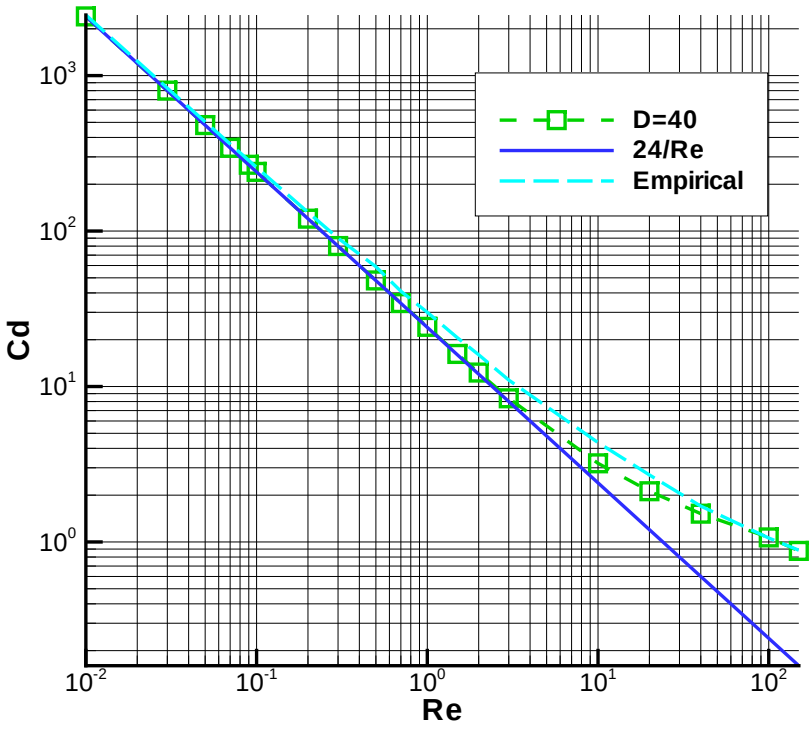

Figure 6.3: Graph showing C_D as a function of Re for axisymmetric flow over a sphere.

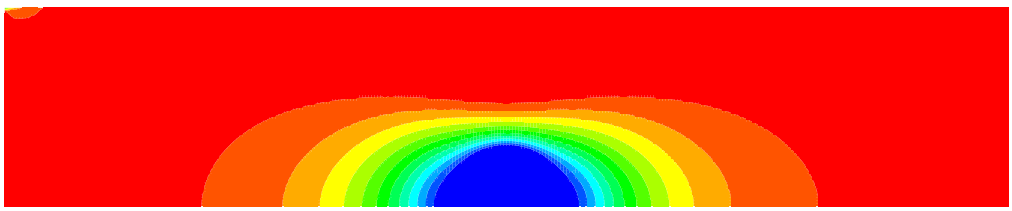

Figure 6.4: Stream-wise velocity contours for axisymmetric flow over a sphere at $Re = 0.01$.

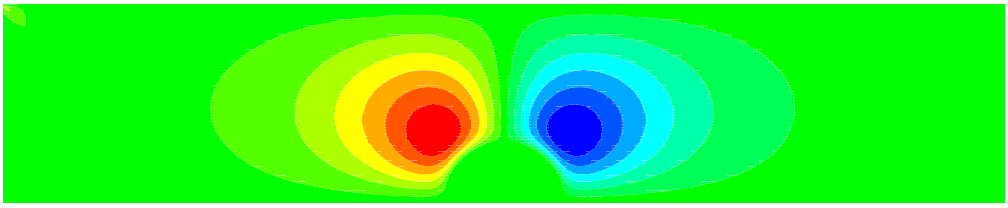

Figure 6.5: Normal velocity contours for axisymmetric flow over a sphere at $Re = 0.01$.

Re	$\bar{C}_D$	C_D	Difference (%)
10	3.58	4.37	18.078
20	2.58	2.68	11.194
40	1.87	1.73	8.208
100	1.07	1.06	0.9

Table 6.3: Comparison of drag coefficient for axisymmetric flow over a sphere for larger Reynolds numbers

merical approximations for larger Reynolds numbers. In all cases $U = 0.05$ and $D = 40$. We clearly see that the lattice Boltzmann predictions and the empirical formula are in better agreement when Re is large. Figure 6.3 plots the drag coefficient as a function of Reynolds number and clearly shows the excellent agrement between the analytic formula for C_D in axisymmetric Stokes' flow and the lattice Boltzmann predictions. The graph also highlights the numerical predictions departure from Stokes' formula and approach to the empirical formula (6.50) at increasing Re

6.5 Discussion

In this chapter we developed an axisymmetric lattice Boltzmann equation which is shown to be a second-order approximation to the axisymmetric Navier-Stokes equations. Unlike previous models this one correctly applies the Chapman-Enskog analysis to LBE and fully exposes the coupling between the two additional source terms through the non-equilibrium contribution

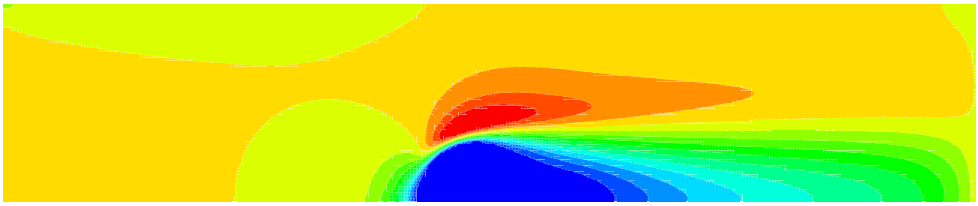

Figure 6.6: Stream-wise velocity contours for axisymmetric flow over a sphere at $Re = 100$.

to the D2Q9 distribution function, therefore recovering the correct spatial derivatives in the macroscopic limit. These source terms are geometric forces which are consistent with the general form for additional LBE forces as found by Guo et al. [17]. Moreover, the source terms derived here are more local than those of Halliday et al [18] since they are given mainly in terms of moments of the non-equilibrium distribution function. This has the practical advantage of reducing the amount of numerical differentiation which is not only more sympathetic to the general lattice Boltzmann philosophy but is also likely to improve computational efficiency and stability. This last point is as yet unproven but a local stability analysis could be conducted using a Fourier-space formulation (cf Section 5.4). We first validated the model by simulating Hagen-Poiseuille flow. This flow has a well-known analytical solution, with which our numerical predictions are shown to agree very well. We then applied our equation to Stokes' flow over a sphere and found an excellent agreement between the analytical and numerical approximations for the drag coefficient for all $Re < 1$ (i.e when Stokes' law is valid). At higher Reynolds numbers our results agree with an empirical formula for the drag based on experimental evidence. Two journal articles, [55] and [53], have been written to account for this new material.

Chapter 7

Multi-Phase Lattice Boltzmann Methods

Our study of lattice Boltzmann models now moves forward into the realm of complex fluids. In this chapter we discuss at length the application of the lattice BGK equation to immiscible multi-phase (in particular two-phase) flows and present the associated numerical results.

We begin this chapter with a brief introduction to the mathematical theory of multi-phase hydrodynamics before reviewing the most favored immiscible lattice Boltzmann methods. Followed is an in-depth study of a chosen model, namely a R-K type model, and our proposed modification. This new model is evaluated with simulations of problems of practical importance and has been published in [54]

7.1 Mathematical Theory of Multi-Phase Flow

The work in this section follows closely Joseph and Renardy [28]. We adopt a fixed Cartesian frame of reference and consider an infinitesimal fluid element having position vector

$$\mathbf{x}(\tau) = (x_1(\tau), x_2(\tau), x_3(\tau)) \tag{7.1}$$

at some time τ. Now define the velocity of the element at time $\tau = t$ to be

$$\mathbf{u}(\mathbf{x}(t), t) = \left. \frac{d\mathbf{x}(\tau)}{d\tau} \right|_{\tau=t}. \tag{7.2}$$

The acceleration of the fluid element at time $\tau = t$ is given by

$$\mathbf{a}(\mathbf{x}(t), t) = \left. \frac{D}{D\tau} \mathbf{u}(\mathbf{x}(\tau), \tau) \right|_{\tau=t}, \tag{7.3}$$

where

$$\frac{D}{D\tau} = \frac{\partial}{\partial \tau} + \frac{dx_\alpha}{d\tau} \frac{\partial}{\partial x_\alpha} = \left(\frac{\partial}{\partial \tau} + \mathbf{u}(\mathbf{x}(\tau), \tau) \cdot \nabla \right) \tag{7.4}$$

is the *material derivative* operator.

7.1.1 Transport Identities

Let $\rho = \rho(\mathbf{x}(t), t)$ be the density at position $\mathbf{x}$ and time t. Let $\Omega(t)$ be any material volume and denote it's boundary by $\partial\Omega$. Conservation of mass requires that the rate of change of the mass occupying $\Omega(t)$ should be zero:

$$\frac{d}{dt} \int_{\Omega(t)} \rho d\Omega = 0. \tag{7.5}$$

If we use the Reynolds transport theorem with equation (7.5) and assume a continuous integrand we find that

$$\frac{D\rho}{Dt} + \rho \nabla \cdot \mathbf{u} = 0. \tag{7.6}$$

If we further assume the fluid is incompressible, that is $\frac{D\rho}{Dt} = 0$, then

$$\nabla \cdot \mathbf{u} = 0. \tag{7.7}$$

Now let $f(\mathbf{x}, t)$ be a smooth field in $\Omega(t)$. The Reynolds transport theorem tells us that

$$\frac{d}{dt} \int_{\Omega(t)} f d\Omega = \int_{\Omega(t)} \left(\frac{Df}{Dt} + f \nabla \cdot \mathbf{u} \right) d\Omega, \tag{7.8}$$

and since equation (7.7) holds (so that ρ is a constant),

$$\frac{d}{dt}\int_{\Omega(t)} \rho f d\Omega = \int_{\Omega(t)} \rho \frac{Df}{Dt} d\Omega. \tag{7.9}$$

Suppose $f(\mathbf{x}, t)$ has a simple discontinuity (that is, a finite jump in value with limits existing on both sides of the discontinuity) across the surface (interface) χ, as shown in Figure 7.1. Following the work of Joseph and Renardy [28] we consider limits in which $\Omega(t)$ tends to zero while χ is held constant, that is $\Omega(t)$ is collapsed onto χ.

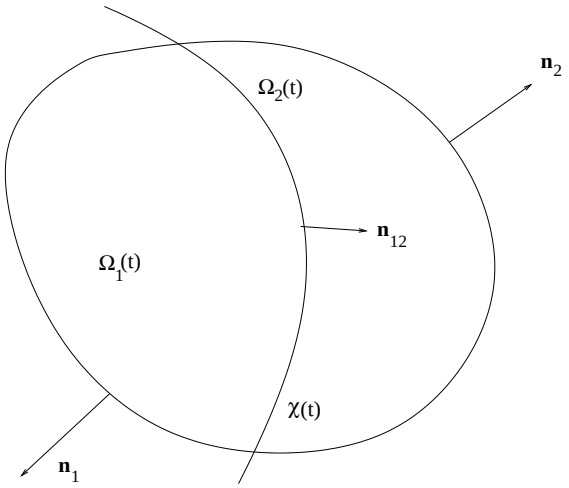

Figure 7.1: The material volume $\Omega(t) = \Omega_1(t) \cup \Omega_2(t)$. $\chi(t)$ is an interface and $\mathbf{n}_1$ and $\mathbf{n}_2$ are the outward normals on $\partial\Omega_1$ and $\partial\Omega_2$, respectively. $\mathbf{n}_{12}$ is from $\partial\Omega_1$ to $\partial\Omega_2$ on χ.

Define

$$[[f]] = f_1(\mathbf{x}, t) - f_2(\mathbf{x}, t) \tag{7.10}$$

as the jump in f at $\mathbf{x} \in \chi$. When concerned with interfaces between two fluids there are two jump identities:

$$\lim_{\Omega\to\chi}\int_{\partial\Omega} \mathbf{n} f dS = \int_{\chi} -\mathbf{n}_{12}[[f]] d\chi, \tag{7.11}$$

$$\lim_{\Omega\to\chi}\frac{d}{dt}\int_{\Omega} \rho f d\Omega = \lim_{\Omega\to\chi}\int_{\Omega} \rho \frac{Df}{Dt} d\Omega = 0, \tag{7.12}$$

where dS is an element on the surface of $\partial\Omega$.

In the absence of any body forces the principle of linear momentum tells us that

$$\frac{d}{dt}\int_{\Omega}\rho\mathbf{u}d\Omega = \int_{\partial\Omega}\mathbf{t}dS + \int_{\partial\chi}\sigma\hat{\mathbf{n}}dl, \tag{7.13}$$

where $\sigma(\mathbf{x})$ is the surface tension on the interface, $\hat{\mathbf{n}}$ is the normal of the curve $\partial\chi = \chi \cap \partial\Omega$, $\mathbf{t}$ is the traction vector and the last term in equation (7.13) is a line integral representing the force due to interfacial stresses. Using the divergence theorem this integral can be written as

$$\int_{\chi}\left[\nabla\sigma - \mathbf{n}_{12}\left(\mathbf{n}_{12}\cdot\nabla\sigma\right) + \left(\frac{1}{R_1}+\frac{1}{R_2}\right)\sigma\mathbf{n}_{12}\right]d\chi, \tag{7.14}$$

where R_1 and R_2 are the principal radii of curvature.

In equation (7.13) the traction vector $\mathbf{t}$ is a traction vector is given by the Cauchy-Fourier formula $\mathbf{t} = \boldsymbol{\Sigma}\mathbf{n}$. Here, $\boldsymbol{\Sigma}$ is the symmetric stress tensor which in components has the form

$$\Sigma_{\alpha\beta} = -p\delta_{\alpha\beta} + T_{\alpha\beta}, \tag{7.15}$$

where p is the pressure. The extra-stress tensor $\mathbf{T}$ is assumed to be a linear function of the velocity gradient $\nabla\mathbf{u}$ and as a consequence can be written as

$$T_{\alpha\beta} = A_{\alpha\beta\gamma\delta}\frac{\partial u_{\gamma}}{\partial x_{\delta}}, \tag{7.16}$$

where $\mathbf{A}$ is some fourth-order tensor. Assuming it is an isotropic function of the components of $\nabla\mathbf{u}$ the extra stress tensor $\mathbf{T}$ is found to have the following form:

$$\mathbf{T} = \eta\dot{\boldsymbol{\gamma}}, \tag{7.17}$$

where η is known as the dynamic viscosity and

$$\dot{\boldsymbol{\gamma}} = \left(\nabla\mathbf{u} + (\nabla\mathbf{u})^{T}\right) \tag{7.18}$$

is the rate of strain tensor. The superscript T denotes the transpose of a

tensor.

Equation (7.12) tells us the discontinuity in f does not alter equation (7.9), which when applied to (7.13) yields

$$\int_{\Omega} \rho \frac{D\mathbf{u}}{Dt} d\Omega = \int_{\partial\Omega} \boldsymbol{\Sigma}\mathbf{n} dS + \int_{\chi} \left[\nabla\sigma - \mathbf{n}_{12} \left(\mathbf{n}_{12} \cdot \nabla\sigma \right) + \left(\frac{1}{R_1} + \frac{1}{R_2} \right) \sigma \mathbf{n}_{12} \right] d\chi. \tag{7.19}$$

By first noting that with the use of equation (7.11)

$$\int_{\partial\Omega} \boldsymbol{\Sigma}\mathbf{n} dS = \int_{\partial\Omega_1} \boldsymbol{\Sigma}\mathbf{n}_1 dS + \int_{\partial\Omega_2} \boldsymbol{\Sigma}\mathbf{n}_2 dS - \int_{\chi} [[\boldsymbol{\Sigma}]]\mathbf{n}_{12} d\chi \tag{7.20}$$

and then applying the divergence theorem we see that

$$\int_{\Omega} \left(\rho \frac{D\mathbf{u}}{Dt} - \nabla \cdot \boldsymbol{\Sigma} \right) d\Omega + \int_{\chi} \left[[[\boldsymbol{\Sigma}]]\mathbf{n}_{12} - \nabla\sigma + \mathbf{n}_{12} \left(\mathbf{n}_{12} \cdot \nabla\sigma \right) - \left(\frac{1}{R_1} + \frac{1}{R_2} \right) \sigma \mathbf{n}_{12} \right] d\chi = 0. \tag{7.21}$$

Finally, if we argue that equation (7.21) is true for all closed bounded material volumes Ω and surfaces of discontinuity χ the governing equations for a bi-component fluid are found to be

$$\rho \frac{D\mathbf{u}}{Dt} = \nabla \cdot \boldsymbol{\Sigma}, \quad \mathbf{x} \in \Omega_1 \text{ or } \Omega_2, \tag{7.22}$$

$$[[\boldsymbol{\Sigma}]]\, \mathbf{n}_{12} = \nabla\sigma - \mathbf{n}_{12} \left(\mathbf{n}_{12} \cdot \nabla\sigma \right) + \left(\frac{1}{R_1} + \frac{1}{R_2} \right) \sigma \mathbf{n}_{12}, \quad \mathbf{x} \in \chi. \tag{7.23}$$

We close this subsection with a few remarks on the boundary conditions at a fluid-fluid interface. We state that the velocity across such an interface is continuous:

$$[[\mathbf{u}]] = 0. \tag{7.24}$$

Equation (7.23) tells us the shear stress is also continuous, that is

$$\mathbf{t}_k \cdot [[\eta\dot{\boldsymbol{\gamma}}]] \cdot \mathbf{n}_{12} = 0, \quad k = 1, 2, \tag{7.25}$$

where $\mathbf{t}_k$ is tangential to the interface. The normal stress jump is balanced by the surface tension:

$$\mathbf{n}_{12} \cdot [[\eta\dot{\boldsymbol{\gamma}}]] \cdot \mathbf{n}_{12} - [[p]] + \left(\frac{1}{R_1} + \frac{1}{R_2}\right)\sigma = 0. \tag{7.26}$$

Also, a kinematic free-surface condition holds at the interface:

$$\frac{\partial h}{\partial t} + \mathbf{u} \cdot \nabla h = 0, \tag{7.27}$$

where $h(\mathbf{x}(t), t) = 0$ describes the interface.

7.1.2 Non-Unique Solutions

Joseph and Renardy [28] note that, since the position of a fluid-fluid interface is unknown, a steady state solution to the multi-phase equations of motion (7.22,7.23) is not unique. For example, if two immiscible fluids of equal density are contained within a domain Ω spheres, or bubbles, of one fluid will emerge. The size and position of these bubbles at steady state are not unique.

Parallel shear flows of layers of two (or more) liquids also have a continuum of solutions. There could be, in theory, N layers of one fluid with viscosity η_1 separated by layers of another fluid with viscosity η_2. The number of layers and their heights is arbitrary. Although there is an infinite number of solutions to problems of this type the configurations that are realised in experiments position the low viscosity component in regions of high shear. It is argued in [28] that the low viscosity fluid will encapsulate the high viscosity fluid. Moreover it is proven, by a viscous dissipation principle, that the arrangement in plane Poiseuille flow that maximises the mass flux is as shown in Figure 7.2.

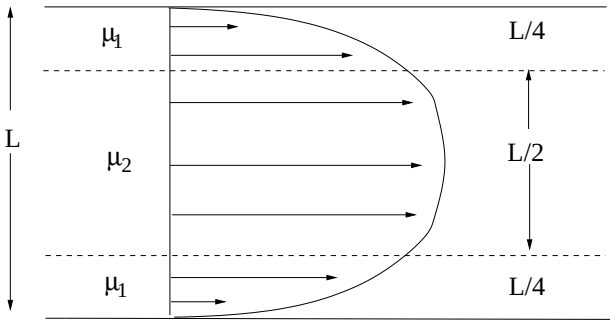

Figure 7.2: Layered plane Poiseuille that maximises the mass flux for a given pressure gradient with $\mu_1 < \mu_2$ (from [28]).

7.2 Multi-Phase Lattice Boltzmann Models

A time dependent interface, as described above, provides an added difficulty to computation techniques for multi-phase flow. These moving boundaries require tracking in time - a task not easily accomplished by continuum based numerical methods. For example, a Lagrangian approach can accurately track an interface by attaching to it a number of probes, the dynamics of which follow the boundary evolution. However, if the interface topology is radically altered this method can suffer from ill-conditioning and singularities, and due to re-meshing three-dimensional computations can prove to be costly. An Eulerian approach on the other hand can overcome these difficulties since large deformations in an interface can be captured without a re-discretisation of the domain. Rather than track the interface explicitly, this method reconstructs it as an isocontour of a field variable. The problem with this technique is, due to the lack of explicit treatment, interfacial diffusion effects are generally smeared over a region surrounding this boundary.

From a micro/mesoscopic view point the segregation of two fluids is due to inter-particle forces. The Lattice Boltzmann method is therefore in a strong position compared to its macroscopic rivals since these particle interaction can be incorporated into the evolution of the distribution function. As a result, a multi-phase Lattice Boltzmann should not track interfaces but rather let them spontaneously emerge from the underlying dynamics.

A number of Lattice Boltzmann models have been developed to predict the flow of two interacting fluids, each showing a degree of success in a variety of test situations but also several limitations. We now present an overview of the most favoured models. A comprehensive survey of two-phase Lattice Boltzmann techniques can be found in [44, 61].

7.2.1 The R-K Model

In 1989, Rothman and Keller [57] proposed an extension to the FHP (with rest particles) to incorporate immiscible two-phase effects in fluid flow. Soon after, Gunstensen [16] developed a multi-phase Lattice Boltzmann model based on the principles of Rothman and Keller.

The technique behind these models, which are to be referred to as R-K models, is to define two types of particles which can be distinguished by a *colour*, say "red" and "blue", and add to the collision process a routine which will encourage like particles to congregate.

The first step in the Gunstensen algorithm is the usual single face collision step:

$$N_i' = N_i - \omega \left(N_i(\mathbf{x}, t) - N_i^{(e)}(\mathbf{x}, t) \right), \tag{7.28}$$

where N_i' denotes the post collision state. The expected number of particles is $N_i = R_i + B_i$, where R_i and B_i are the number of red and blue particles, respectively. Next, a surface tension inducing perturbation step is added to N_i':

$$N_i'' = N_i' + A|\mathbf{F}| \cos[2(\theta_i - \theta_F)], \tag{7.29}$$

where A is a parameter controlling surface tension, θ_i is the angle of lattice direction i, and θ_F is the angle of the *colour gradient* $\mathbf{F}$ which is given by

$$\mathbf{F}(\mathbf{x}) = \sum_i \sum_j \mathbf{c}_i \left[R_j(\mathbf{x} + \mathbf{c}_i) - B_j(\mathbf{x} + \mathbf{c}_i) \right]. \tag{7.30}$$

The next step is a recolouring procedure designed to achieve zero diffusivity of one colour into the other (but conserving total mass). Finally the populations are propagated to their nearest neighbours.

The authors derived a theoretical expression for the surface tension which was shown to agree very well with Laplace's law. They also showed a preliminary application to flow in porous media. Although it predicts some multi-phase phenomena, this original method can only deal with fluids of equal viscosity and density. A similar model that allows for a variation in these quantities was developed by Grunau *et.al* [15] and since this publication immiscible LBM's adopting a similar technique have been developed for three dimensional models in porous media [65] and for incorporating microcurrents into curved boundaries [19]. Further advances have shown an improvement in the isotropy of the interface [33] and a comprehensive study of the diffusion and phase separation properties of these gradient-based models can be found in [32].

R-K type models have been shown to produce results in good agreement with analytical solutions and experimental observations. They use a relatively straightforward addition to the LBGK algorithm which is easy to implement. However, the optimisation step can be computationally expensive and a more in-depth study reveals R-K models obey an ideal equation of state. Despite these drawbacks we chose to develop and use models of this type because of their success with bi-component flows, their ability to maintain sharp interfaces, their potential to tackle complicated "real-life" industrial applications and, unlike other immiscible LBM's, they allow us to fix the surface tension value *a priori*.

7.2.2 The Shan-Chen Model

The pseudo-potential approach introduced by Shan and Chen [6] is a multi-phase LBM that attempts to be a more physically orientated model than the R-K models described above. Since flows with more than one phase have a non-ideal equation of state, Shan and Chen looked to preserve this feature in a lattice Boltzmann framework by incorporating non-local interactions among particles.

The evolution equation in the Shan-Chen model is similar to the normal

LBGK equation:

$$N_i(\mathbf{x}+\mathbf{c}_i, t+1) = N_i(\mathbf{x}, t) - \omega\left(N_i(\mathbf{x}, t) - N_i^{(e)}(\mathbf{x}, t)\right) \tag{7.31}$$

but in this model an additional momentum forcing term $\mathbf{\Gamma}$ is explicitly added to the velocity field after each time step:

$$\mathbf{u}^*(\mathbf{x}, t) = \mathbf{u}(\mathbf{x}, t) + \mathbf{\Gamma}(\mathbf{x}, t), \tag{7.32}$$

where

$$\mathbf{\Gamma}(\mathbf{x}, t) = -\frac{1}{\omega\rho}\psi(\mathbf{x})\mathcal{G}\sum_i \psi(\mathbf{x}+\mathbf{c}_i)\mathbf{c}_i. \tag{7.33}$$

In the above equation $\psi(\mathbf{x})$ is a "potential" function and $\mathcal{G}$ comes from a Green's function:

$$G(|\mathbf{x}-\mathbf{x}'|) = \begin{cases} 0, & \text{if } |\mathbf{x}-\mathbf{x}'| > 1 \\ \mathcal{G}, & \text{if } |\mathbf{x}-\mathbf{x}'| = 1. \end{cases}$$

Unlike the R-K methods this model has, in general, a non-ideal equation of state, for a D2Q9 lattice given by

$$p = \frac{\rho}{3} + 4\mathcal{G}\psi^2. \tag{7.34}$$

Consequently, thermodynamic phase transition will occur if the pressure p is not a monotonically increasing function of the density ρ.

Shan and Chen demonstrated in [6] that phase transition occurs whenever the interaction strength $\mathcal{G}$ exceeds a critical value $\mathcal{G}_c$. They also point out that their model can simulate fluids with immiscible components by setting $\psi = \rho$. This leads to an ideal equation of state. Chin *et al* used a Shan-Chen model on a D2Q9 lattice with the LBGK collision operator to simulate flows of immiscible fluids with different viscosities. Their prediction of Laplace's law for surface tension gives noticeable errors and their simulated results for Poiseuille flow, although in close agreement in single fluid regions, shows discrepancies near an interface.

Due to its simplicity and elegance the Shan-Chen model is probably the

most popular choice for flows with phase transitions. Encouraging results in comparison to thermodynamic theory have been obtained [6,7,60]. There are unfortunately a number of drawbacks. As pointed out in [44] this model cannot introduce a temperature which is consistent with thermodynamics and Luo [36] shows that the equation of state is not the same in the momentum equation and the energy equation.

7.2.3 The Free Energy Model

Striving to ensure thermodynamic consistency within the lattice Boltzmann framework, Swift *et al* [63] introduced a non-ideal pressure tensor directly into the collision operator by taking into consideration the free energy functional Φ defined as

$$\Phi(\mathbf{x}) = \int \frac{\kappa}{2} \left[(\nabla \rho)^2 + \phi(\rho) \right] d\mathbf{x}, \tag{7.35}$$

where κ is the interfacial energy and the second term in the integrand describes the bulk free energy. The local pressure tensor then relates to Φ through

$$p = \rho \frac{\partial \Phi}{\partial \rho} - \Phi. \tag{7.36}$$

The full pressure tensor is obtained by adding off-diagonal terms:

$$P_{\alpha\beta} = p\delta_{\alpha\beta} + \kappa \partial_\alpha \rho \partial_\beta \rho. \tag{7.37}$$

In order to include this pressure tensor into the equilibrium function, Swift *et al* used an expansion of $N_i^{(e)}$ similar to that laid out in Section 5.2 but extended to incorporate the non-local thermodynamic properties of equation 7.36:

$$N_i^{(e)} = A + Bc_{i\alpha}u_\beta + Cu^2 + Du_\alpha u_\beta c_{i\alpha}c_{i\beta} + E_\alpha c_{i\alpha} + F_{\alpha\beta}c_{i\alpha}c_{i\beta}. \tag{7.38}$$

The coefficients can be found using the moments of $N_i^{(e)}$ as in Section 5.2.

To test their model Swift *et al* [63] performed numerical simulations (on

a FHP lattice with one rest particle) using a Van-de-Waals equation of state:

$$\phi = \rho T \ln\left(\frac{\rho}{1-b\rho}\right) - a\rho^2, \tag{7.39}$$

where a and b are free parameters. They report a very good agreement between the mechanical (Laplace's law) and thermodynamic definitions of surface tension. Also shown in [63] is the accurate prediction of the coexistence curve between the two phases for different fluid temperatures. Further work with the Free Energy model was undertaken by Inamuro, Nobuharu and Ogino [26] who showed Galilean invariance of the model in moving droplet deformation and breakup simulations, and Xu, Gonnella and Lamura [69] improved the stability of the model by controlling density fluctuations.

Theoretical criticisms of the free energy approach are made strongly by Luo [35, 36]. He points out that since density gradients do not appear in the first order Chapman-Enskog expansion (cf Section 5.3) the inclusion of $\nabla\rho$ terms in equation (7.37) is not justified. An in-depth study reveals other shortcomings such as a degree of anisotropy and varying temperature even though the model claims to be isothermal. Although all the algorithms considered so far in this Section are in some way mathematically *ad hoc* it appears from the work of Luo that the Free Energy model is also physically incorrect.

7.2.4 Contemporary Methods

In a series of theoretical papers Li-Shi Luo [35–37] formally derived a multiphase lattice Boltzmann model from the kinetic theory of non-ideal gases and binary mixtures in an *a priori* fashion. If the Enskog extension to the Boltzmann equation which, if BGK approximation is used, is given by

$$\partial_t f + \boldsymbol{\xi}\cdot\nabla f + \mathbf{a}\cdot\nabla_\xi f = -\frac{g}{\lambda}\left[f - f^{(e)}\right] + J', \tag{7.40}$$

where

$$J' = -f^{(e)} b\rho g[\boldsymbol{\xi} - \mathbf{u}]\cdot\ln(\rho^2 g), \tag{7.41}$$

properly describes non-ideal dense gases, Luo proceeded to obtain a lattice Boltzmann-type equation via the expansion and phase-space discretisation[1] of equations (7.40) and (7.41). In these equations f is the (continuous) single particle distribution function, $f^{(e)}$ is the local (Maxwellian) equilibrium function, $\boldsymbol{\xi}$ and $\mathbf{a}$ the particle velocity and acceleration, respectively, λ is a relaxation time, $g = g(b\rho)$ and b is a constant. The resulting lattice Boltzmann equation on a D2Q9 lattice, assuming unit time steps and lattice spacing, is shown to be:

$$\begin{aligned} N_i(\mathbf{x}+\mathbf{c}_i, t+1) - N_i(\mathbf{x}, t) = \\ -g\omega \left[N_i(\mathbf{x}, t) - N_i^{(e)}(\mathbf{x}, t) \right] \\ -bgN_i^{(e)}(\mathbf{x}, t) \times (\mathbf{c}_i - \mathbf{u}) \cdot \nabla \left(\rho^2 g \right) - F_i, \end{aligned} \tag{7.42}$$

where

$$F_i = -3W_i\rho \left[(\mathbf{c}_i - \mathbf{u}) + 3(\mathbf{c}_i \cdot \mathbf{u})\mathbf{c}_i \right] \cdot \mathbf{a}, \tag{7.43}$$

and the weights W_i are defined in equation (5.28). The pressure, found through the Chapman-Enskog analysis, is given by

$$P = \rho\theta(1 + b\rho g), \tag{7.44}$$

where the normalised temperature θ is defined by

$$\theta = \frac{\rho}{2} \sum_i (\mathbf{c}_i - \mathbf{u})^2 N_i^{(e)}, \tag{7.45}$$

and g can be found by specifying an appropriate equation of state.

For the case of binary mixtures a similar procedure with the associated kinetic theory (details of which can be found in [37]) leads to the following lattice Boltzmann equation:

$$N_i^k(\mathbf{x}+\mathbf{c}_i, t+1) - N_i^k(\mathbf{x}, t) = Q_i^{kk} + Q_i^{kl} - F_i^k, \tag{7.46}$$

[1] Luo first employed this technique to obtain the lattice Boltzmann equation directly from the Boltzmann equation [38].

where

$$Q_i^{kk} = -\omega_i \left[N_i^k - N_i^{k(e)} \right], \tag{7.47}$$

$$Q_i^{kl} = -\omega \frac{\rho_l}{\rho} \frac{N^{k(0)}}{R_k T} (\mathbf{c}_i - \mathbf{u}) \cdot (\mathbf{u}_k - \mathbf{u}_l), \tag{7.48}$$

$$F_k^k = -W_i \rho_k \frac{\mathbf{c}_i \cdot \mathbf{a}_k}{R_k T}, \tag{7.49}$$

where k and l refer to fluid species, ρ and $\mathbf{u}$ are the density and velocity of the mixture, respectively, T is the temperature and R_k is the gas constant for species k. The equilibrium function $N_i^{k(e)}$ has the following form:

$$N_i^{k(e)} = \left[1 + \frac{1}{R_k T} (\mathbf{c}_i - \mathbf{u}) \cdot (\mathbf{u}_k - \mathbf{u}) \right] N_i^{k(0)}, \tag{7.50}$$

$$N_i^{k(0)} = W_i \rho_k \left[1 + \frac{(\mathbf{c}_i - \mathbf{u}) \cdot \mathbf{u}}{R_k T} + \frac{(\mathbf{c}_i \cdot \mathbf{u})^2}{2 (R_k T)^2} \right], \tag{7.51}$$

and the macroscopic density and momentum for each species are defined as the first two moments of $N_i^{k(e)}$, respectively. It should be noted that this model does not have a surface tension.

Recent work by McCracken and Abraham [40] builds on the theoretical work of Luo and Girimanji [37] by using multiple relaxation times in the collision process. They have shown that this model improves numerical stability compared to the LBGK operator and verified the model with numerical experiments. Other contributions come from Premnath and Abraham [49] who presented a model for axisymmetric multi-phase flows in a Cartesian coordinate system and reported satisfactory agreement between their simulated results and available data for a number of test problems including Rayleigh capillary instability and breakup.

7.3 Immiscible Lattice Boltzmann Model

We now expand on our notes of Section 7.2.1 to develop a R-K-type model for immiscible binary fluids with different densities and viscosities, similar to the work of Grunau *et al* [15]. Like these authors we use a lattice Boltzmann

equation with a single relaxation parameter for each fluid but use a D2Q9 lattice rather than a 7-velocity FHP lattice with additional rest particles. The equilibrium expressions given in this section, found by a simple ansatz, thus differ to those in [15] and the collision operator is modified to satisfy the conservation laws and recover the extra volume source term in the multi-phase Navier-Stokes equations.

Let N_i^k be the single particle distribution function for fluid k, where $k = r$ or b denotes the *colour* ("red" or "blue"). The total population at node $\mathbf{x}$ and time t is

$$N_i(\mathbf{x}, t) = N_i^r(\mathbf{x}, t) + N_i^b(\mathbf{x}, t), \tag{7.52}$$

and the evolution equation for each phase is

$$N_i^k(\mathbf{x} + \mathbf{c}_i, t + 1) = N_i^k(\mathbf{x}, t) + \Omega_i^k(\mathbf{x}, t). \tag{7.53}$$

The collision operator

$$\Omega_i^k = \left(\Omega_i^k\right)^{(1)} + \left(\Omega_i^k\right)^{(2)}, \quad i = 0, \ldots, 8 \tag{7.54}$$

consists of two processes. The first represents relaxation to a local equilibrium state using, for simplicity, an LBGK operator:

$$\left(\Omega_i^k\right)^{(1)} = -\omega_k \left(N_i^k - N_i^{k(e)}\right), \tag{7.55}$$

where $N_i^{k(e)}$ is an equilibrium function and ω_k is the relaxation parameter of fluid k. $\left(\Omega_i^k\right)^{(2)}$ is derived in Section 7.3.1.

Mass and momentum are, as usual, defined to be the first two moments of the distribution function respectively, and conservation of these quantities require

$$\rho_k = \sum_i N_i^k = \sum_i N_i^{k(e)}, \tag{7.56}$$

$$\rho \mathbf{u} = \sum_i \sum_k N_i^k \mathbf{c}_i = \sum_i \sum_k N_i^{k(e)} \mathbf{c}_i, \tag{7.57}$$

where ρ_k is the density of fluid k, $\rho = \rho_r + \rho_b$ is the total density, and $\mathbf{u}$ is the local fluid velocity.

The equilibrium function, $N_i^{k(e)}$, can be chosen arbitrarily providing it respects the conservation constraints of equations (7.56) and (7.57). To derive an expression we specify a D2Q9 lattice domain and use the following ansatz:

$$\begin{aligned} N_0^{k(e)} &= A_0^k + D_0^k \mathbf{u}^2, && (7.58)\\ N_i^{k(e)} &= A_1^k + B_1^k \mathbf{c}_i \cdot \mathbf{u} + C_1^k (\mathbf{c}_i \cdot \mathbf{u})^2 + D_1^k \mathbf{u}^2, \quad i = 1,2,3,4, && (7.59)\\ N_i^{k(e)} &= A_2^k + B_2^k \mathbf{c}_i \cdot \mathbf{u} + C_2^k (\mathbf{c}_i \cdot \mathbf{u})^2 + D_2^k \mathbf{u}^2, \quad i = 5,6,7,8, && (7.60) \end{aligned}$$

where the 10 capital letters are free parameters to be 'tuned' accordingly. To continue we adopt tactics similar to Section 5.2 and take advantage of the first three moments of the equilibrium function. However, to achieve a stable interface we require the non-stationary distribution functions for both liquids to be equal when $\mathbf{u} = 0$. To meet this condition we assume

$$\frac{B_1^k}{B_2^k} = \frac{D_0^k}{D_1^k} = \frac{D_1^k}{D_2^k} = r \tag{7.61}$$

and find $r = 4$. Now assume

$$\begin{aligned} A_0^k &= \alpha_k \rho_k, && (7.62)\\ \frac{A_1^k}{A_2^k} &= r, && (7.63) \end{aligned}$$

where α_k is a free parameter. The equilibrium functions are readily found to be

$$N_0^{k(e)} = \rho_k \left(\alpha_k - \frac{2}{3}\mathbf{u}^2 \right), \tag{7.64}$$

$$N_i^{k(e)} = \rho_k \left(\frac{1-\alpha_k}{5} + W_i \left[3\mathbf{c}_i \cdot \mathbf{u} + \frac{9}{2}(\mathbf{c}_i \cdot \mathbf{u})^2 - \frac{3}{2}\mathbf{u}^2 \right] \right), \quad \text{for} \quad i = 1,2,3,4, \tag{7.65}$$

$$N_i^{k(e)} = \rho_k \left(\frac{1-\alpha_k}{20} + W_i \left[3\mathbf{c}_i \cdot \mathbf{u} + \frac{9}{2}(\mathbf{c}_i \cdot \mathbf{u})^2 - \frac{3}{2}\mathbf{u}^2 \right] \right), \quad \text{for} \quad i = 5,6,7,8, \tag{7.66}$$

where the weights W_i are given by equation (5.28). The stable interface assumption leads to the following density ratio, γ:

$$\gamma = \frac{\rho_r}{\rho_b} = \frac{1-\alpha_b}{1-\alpha_r}, \tag{7.67}$$

with the pressure given by:

$$p_0^k = \frac{3\rho_k\,(1-\alpha_k)}{5} = \rho_k (c_s^k)^2, \tag{7.68}$$

which satisfies an ideal equation of state.

The parameter α_k determines the speed of sound, $(c_s^k)^2$, thus controlling the hydrodynamic pressure at interfaces. It can be viewed as representing the ensemble average number of degenerate rest particles, which is needed to achieve a stable interface and achieve a density variation between the fluids. Therefore the choice of α_k is important for flows with a large density difference. To ensure that $0 < N_i^k < 1$ in a mixed region we require

$$0 < \alpha_k < 1, \tag{7.69}$$

and a little manipulation reveals that

$$\frac{\rho_r - \rho_b}{\rho_r} < \alpha_r < 1, \tag{7.70}$$

if $\rho_r > \rho_b$.

7.3.1 Two-Phase Collision Operator

The two-phase collision operator, $\left(\Omega_i^k\right)^{(2)}$, is defined in such a way as to encourage colour segregation while satisfying the conservation constraints of equations (7.56) and (7.57). A spatial colour difference, $\bar{\rho}$, is defined as

$$\bar{\rho}(\mathbf{x}) = \rho_r(\mathbf{x}) - \rho_b(\mathbf{x}). \tag{7.71}$$

The colour gradient may be calculated in terms of the colour difference using

$$\mathbf{H}(\mathbf{x}) = \nabla\bar{\rho}(\mathbf{x}).$$

A fourth-order approximation, $\mathbf{F}$, to the colour gradient, $\mathbf{H}$, is given by

$$\mathbf{F}(\mathbf{x}) = \sum_{i=1}^{8} \mathbf{c}_i \left[\rho_r\left(\mathbf{x}+\mathbf{c}_i\right) - \rho_b\left(\mathbf{x}+\mathbf{c}_i\right)\right]. \tag{7.72}$$

Since the colour gradient is perpendicular to the interface, we can define an approximate unit normal, $\mathbf{n}$, to the surface:

$$\mathbf{n} = \frac{\mathbf{F}}{|\mathbf{F}|} \simeq \frac{\nabla\bar{\rho}}{|\nabla\bar{\rho}|}.$$

An extension of the model proposed by Grunau et al. [15] to a D2Q9 lattice would give

$$\left(\Omega_i^k\right)^{(2)} = \frac{A_k}{2}|\mathbf{F}|\left[\frac{(\mathbf{F}\cdot\mathbf{c}_i)^2}{|\mathbf{F}|^2} - \frac{3}{4}\right], \quad i = 1,\ldots,8. \tag{7.73}$$

In the above equation A_k is a free parameter controlling surface tension and we note that $\mathbf{F} = 0$ in pure phases, thus $\left(\Omega_i^k\right)^{(2)}$ only contributes to mixed interfacial regions. The factor 3/4 (1/2 in [15]) in equation (7.73) is included to ensure the conservation of mass and momentum:

$$\sum_{i=1}^{8}\left(\Omega_i^k\right)^{(2)} = 0, \tag{7.74}$$

$$\sum_{i=1}^{8}\left(\Omega_i^k\right)\mathbf{c}_i^{(2)} = 0. \tag{7.75}$$

However, it can be shown using the Chapman-Enskog technique that it is not possible to derive the macroscopic continuum equations for multiphase flow when the two-phase collision operator is defined by (7.73). To obtain the correct form of the continuum equations we propose the following repre-

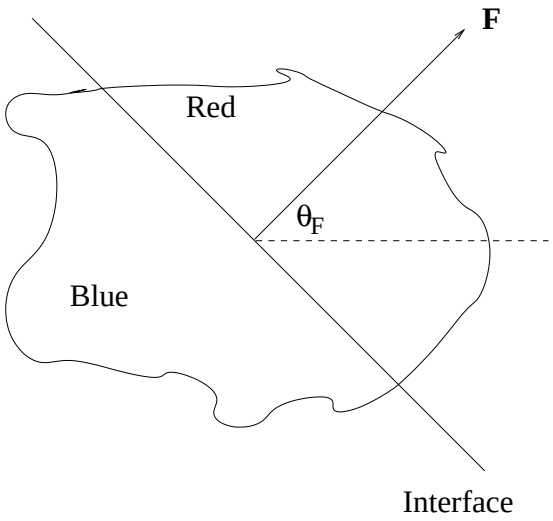

Figure 7.3: The colour gradient $\mathbf{F}$ is normal to a fluid-fluid interface.

sentation of the two-phase collision operator

$$\left(\Omega_i^k\right)^{(2)} = \frac{A_k}{2}|\mathbf{F}|\left[W_i\frac{(\mathbf{c}_i\cdot\mathbf{F})^2}{|\mathbf{F}|^2} - B_i\right], \quad i = 0,\ldots,8, \tag{7.76}$$

where

$$B_i = \begin{cases} -\dfrac{4}{27}, & i = 0 \\ \dfrac{2}{27}, & i = 1,2,3,4 \\ \dfrac{5}{108}, & i = 5,6,7,8. \end{cases} \tag{7.77}$$

The colour gradient $\mathbf{F}(\mathbf{x})$ is normal to the interface at node $\mathbf{x}$ (see Figure. 7.3) so we see that $(\Omega_i^k)^{(2)}$ in (7.73) serves to add mass to populations moving in this direction and removes mass parallel to the interface. Since this term does not conserve colour densities separately an additional step is needed to promote phase segregation and maintain surfaces between fluids. Following Gunstensen [16], we define the colour flux $\mathbf{K}(\mathbf{x})$ by

$$\mathbf{K}(\mathbf{x}) = \sum_{i=1}^{8}\left(N_i^r - N_i^b\right)\mathbf{c}_i, \tag{7.78}$$

and force this vector to align with the colour gradient (7.72) and minimise the diffusion of one colour into the other.

Re-colouring

The optimisation problem above can be written as follows: Maximise the work done W against the gradient:

$$W = \mathbf{K} \cdot \mathbf{F}, \tag{7.79}$$

subject to the constraints

$$N_i^{r\prime\prime} + N_i^{b\prime\prime} = N_i^{\prime\prime}, \tag{7.80}$$

$$\sum_i N_i^{r\prime\prime} = \rho_r, \tag{7.81}$$

where the double primes denote post two-phase collision quantities. Differentiating W with respect to $N_i^{r\prime\prime}$ and $N_i^{b\prime\prime}$ yields

$$\frac{\partial W}{\partial N_i^{r\prime\prime}} = \sum_i (\mathbf{c}_i \cdot \mathbf{F}) = 0, \tag{7.82}$$

$$\frac{\partial W}{\partial N_i^{b\prime\prime}} = -\sum_i (\mathbf{c}_i \cdot \mathbf{F}) = 0, \tag{7.83}$$

i.e, there are no turning points. Optimisation techniques such as the method of Lagrangian multipliers are therefore redundant. We continue to solve the maximisation problem in a more *ad hoc* fashion. The link vectors $\mathbf{c}_i$ are listed in descending order starting with the one nearest the colour gradient $\mathbf{F}$. The maximum amount of red particles available are sent in the directions close to $\mathbf{F}$ (i.e perpendicular to the interface) while blue particles are sent the opposite way, subject to constraints (7.80) and (7.81). Latva-Kokko and Rothman [32] point out that a potential drawback of this re-colouring technique is so called lattice pinning. This situation occurs when one of the fluids, say red, is close to or on a fluid-fluid interface but the flow is too weak to move many red particles. The interface now becomes pinned to the

lattice. Latva-Kokko and Rothamn studied this effect in the case of small bubbles concentrated around one lattice node. The authors report that such bubbles will not move unless forced very hard - a problem which can be of significance when examining the flow and separation of an initially mixed state. Alternative re-colouring schemes which reduce lattice pinning but widen the interface have been suggested by Latva-Kokko and Rothman [32], and Tölke et al. [65].

Interface relaxation parameter

The thickness of an interface will depend on an averaged relaxation parameter. When the relaxation parameters ω_k, and therefore the viscosities, of the two fluids are different, the interface width increases. To ensure a stable interface and smooth change in viscosity we define an order parameter ψ in the same fashion of Grunau [15] et al.:

$$\psi = \frac{\rho_r - \rho_b}{\rho_r + \rho_b}. \tag{7.84}$$

The relaxation parameter ω is defined as follows:

$$\omega = \begin{cases} \omega_r, & \psi > \delta, \\ f_r(\psi), & \delta \geq \psi > 0, \\ f_b(\psi), & 0 \geq \psi \geq -\delta, \\ \omega_b, & \psi < -\delta, \end{cases} \tag{7.85}$$

where

$$f_r(\psi) = \beta + \gamma\psi + \epsilon\psi^2, \tag{7.86}$$

$$f_b(\psi) = \beta + \eta\psi + \xi\psi^2, \tag{7.87}$$

and $\beta, \gamma, \epsilon, \eta$ and ξ are constants chosen so that ω and its derivative are continuous. Let $\langle\omega\rangle = 2\omega_r\omega_b/(\omega_r + \omega_b)$ be the averaged relaxation parameter across the interface and assume that $f_r(\delta) = \omega_r$, $f_b(-\delta) = \omega_b$, $\partial\omega/\partial\psi = 0$

when $\psi = \pm\delta$, and $f_r(0) = f_b(0) = \langle\omega\rangle$. Simple algebra reveals that

$$\beta = \langle\omega\rangle, \tag{7.88}$$

$$\gamma = \frac{2(\omega_r - \beta)}{\delta}, \tag{7.89}$$

$$\epsilon = -\frac{\gamma}{2\delta}, \tag{7.90}$$

$$\eta = \frac{2(\beta - \omega_b)}{\delta}, \tag{7.91}$$

$$\xi = \frac{\eta}{2\delta}, \tag{7.92}$$

where $\delta \leq 1$ is a free parameter controlling the thickness of an interface. If the relaxation parameters (and therefore viscosities) are equal the value of δ does not affect the flow. If on the other hand there is a large difference in viscosity between the two fluids the choice of δ could affect the thickness and dynamics of an interface.

7.3.2 Surface Tension

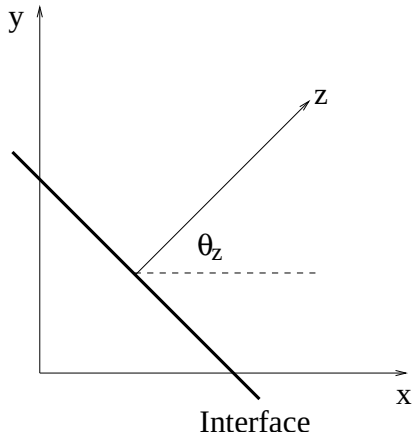

Figure 7.4: Planar interface geometry in Cartesian co-ordinates.

The mechanical definition of surface tension is

$$\sigma = \int_{-\infty}^{\infty} (P_N(z) - P_T(z))dz, \tag{7.93}$$

where P_N and P_T are the normal and tangential components of the pressure tensor and z measures the distance normal to the interface. Let θ_i be the angle between link vector $\mathbf{c}_i$ and the x-axis and let θ_z be the angle between z and the x-axis (Figure 7.4). P_N and P_T are given by

$$P_N = \sum_i N_i c_{iN}^2, \tag{7.94}$$

$$P_T = \sum_i N_i c_{iT}^2, \tag{7.95}$$

where

$$c_{iN} = |\mathbf{c}_i| \cos(\theta_i - \theta_z), \tag{7.96}$$

$$c_{iT} = |\mathbf{c}_i| \sin(\theta_i - \theta_z). \tag{7.97}$$

Consider equation (7.93) as an average over M adjacent long integration lines $y = constant$ and cast a discrete summation over lattice nodes in an area A [19]:

$$\sigma \approx \frac{\cos\theta_z}{M} \sum_{\mathbf{x}\in A} \sum_i N_i U_i = \frac{\cos\theta_z}{M} \sum_{\mathbf{x}\in A} \sum_i \left(N_i^{(e)} + N_i^{(neq)} \right) U_i, \tag{7.98}$$

where

$$U_i = \mathbf{c}_i^2 \cos[2(\theta_i - \theta_z)]. \tag{7.99}$$

Now consider the equilibrium and non-equilibrium contributions separately. After substituting equations (7.64), (7.65) and (7.66) into (7.98) a little algebraic evaluation leads us to the following relation:

$$\sum_{\mathbf{x}\in A} \sum_i N_i^{(e)} U_i = \sum_{\mathbf{x}\in A} \rho \mathbf{u}^2 \cos[2(\theta_u - \theta_z)], \tag{7.100}$$

where θ_u is defined through

$$u_x = |\mathbf{u}| \cos\theta_u(\mathbf{x}), \tag{7.101}$$

$$u_y = |\mathbf{u}| \sin\theta_u(\mathbf{x}). \tag{7.102}$$

To find the non-equilibrium contribution we note that at steady state the evolution equation is reduced to

$$N_i(\mathbf{x}+\mathbf{c}_i) = N_i(\mathbf{x}) - \omega N_i^{(neq)} + \Omega_i^{(2)}, \quad i = 0, \ldots, 8 \tag{7.103}$$

where $\Omega_i^{(2)} = (\Omega_i^r)^{(2)} + \left(\Omega_i^b\right)^{(2)}$. For a lattice with well defined boundary conditions

$$\sum_{\mathbf{x}} N_i(\mathbf{x}+\mathbf{c}_i) = \sum_{\mathbf{x}} N_i(\mathbf{x}) \tag{7.104}$$

and therefore

$$\sum_{\mathbf{x}}\sum_{i} N_i^{(neq)} U_i = \frac{A_r + A_b}{2\omega} \sum_{\mathbf{x}} |\mathbf{F}| \sum_{i} \left(W_i \frac{(\mathbf{c}_i \cdot \mathbf{F})^2}{|\mathbf{F}|^2} - B_i \right) U_i. \tag{7.105}$$

If we assume $\mathbf{F}/|\mathbf{F}|$ is constant we can write

$$U_i = \left(\frac{(\mathbf{c}_i \cdot \mathbf{F})^2}{|\mathbf{F}|^2} - \frac{(\mathbf{c}_i \cdot \mathbf{G})^2}{|\mathbf{G}|^2} \right), \tag{7.106}$$

where $\mathbf{G}$ is any vector perpendicular to $\mathbf{F}$. This then yields:

$$\sum_{\mathbf{x}}\sum_{i} N_i^{(neq)} U_i = \frac{2(A_r + A_b)}{18\omega} \sum_{\mathbf{x}} |\mathbf{F}|. \tag{7.107}$$

Combining the equilibrium and non-equilibrium contributions then gives:

$$\sigma = \frac{\cos\theta_z}{M} \left(\sum_{\mathbf{x}} \rho \mathbf{u}^2 \cos[2(\theta_u - \theta_z)] + \frac{2(A_r + A_b)}{18\omega} \sum_{\mathbf{x}} |\mathbf{F}| \right). \tag{7.108}$$

The second term in equation (7.108) is relatively straightforward since $|\mathbf{F}|$ vanishes in non-interfacial regions but there appears to be no obvious general simplification of the first term (which is second order in $\mathbf{u}$). It is however manageable in particular circumstances.

To first order in $\mathbf{u}$ we can neglect the first term in (7.108) to obtain

$$\sigma = \frac{\cos\theta_z}{M} \left(\frac{2(A_r + A_b)}{18\omega} \sum_{\mathbf{x}} |\mathbf{F}| \right) \sim \frac{A_r + A_b}{\omega}, \tag{7.109}$$

where ω determines the kinematic viscosity of the fluid through the relationship (5.52).

Plane interfaces

Consider a thin plane interface parallel to the y-axis (such that $\cos\theta_z = 1$) with colour symmetrically separated and assume there are no microcurrents ($\mathbf{u} = 0$), i.e

$$\sigma = \frac{2(A_r + A_b)\cos\theta_z}{18M\omega} \sum_{\mathbf{x}} |\mathbf{F}|. \tag{7.110}$$

The stable interface cannot be centered on a single layer and as we integrate (7.93) along the line perpendicular to the interface three nodes will contribute to the surface tension, i.e there are three nodes with non-zero $\mathbf{F}$: one lying on the line $x = x_0$ and one to both is left and right (Figure 7.5). This corresponds to a $|\mathbf{F}|$ given by

$$|\mathbf{F}| = C\left(\delta(x - x_0 + 1) + \delta(x - x_0) + \delta(x - x_0 - 1)\right), \tag{7.111}$$

where C is a constant and δ here refers to the Dirac delta function. Therefore

$$\begin{aligned} \sigma &= \frac{2C(A_r + A_b)\cos\theta_z}{18M\omega} \sum_{\forall z,x} \left(\delta(x - x_0 + 1) + \delta(x - x_0) + \delta(x - x_0 - 1)\right), \qquad (7.112) \\ &= C\frac{A_r + A_b}{3\omega}. \qquad (7.113) \end{aligned}$$

At steady state the colour gradient is constant, making it possible to estimate $|\mathbf{F}|$, and therefore C. By looking at the amount of red and blue particles at interfacial sites we find that $C = 5\rho/2$ and therefore

$$\sigma = 5\frac{A_r + A_b}{6\omega}. \tag{7.114}$$

To verify the above relation a 64×64 square lattice domain was constructed with a vertical interface through the center. Equal amounts of red and blue fluid filled the domain and for simplicity we set $\omega_r = \omega_b = 1$ and $A_r = A_b = 0.0001$. The system was allowed to evolve to a steady state be-

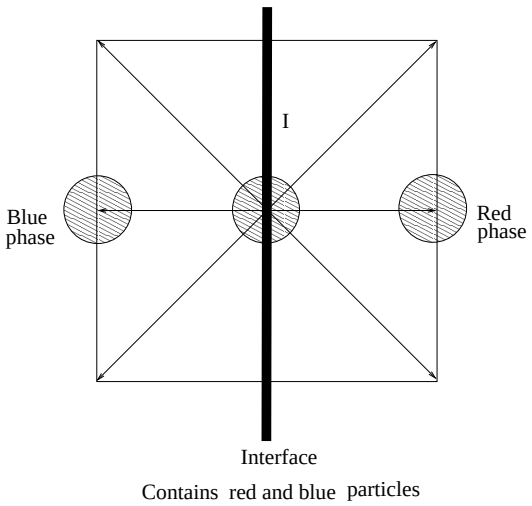

Figure 7.5: Symmetric separation about a thin interface. Circled nodes contribute to the theoretical expression for surface tension.

fore P_N and P_T were measured and the integral (7.93) approximated using a simple trapezoidal formula. Figure 7.6 shows the numerical measurements of the mechanical definition (+) and the theoretical prediction (solid line) of σ as a function of density. The theory and numerics are seen to be in good agreement, confirming the validity of the above analysis.

We also test the capability of the model to predict Laplace's law for surface tension. We construct a 128×128 domain with a bubble of red fluid centered in the middle of the geometry and measure the pressure difference inside and outside the bubble. Laplace's formula is as follows:

$$p_i - p_o = \frac{\sigma}{R}, \tag{7.115}$$

where p_i and p_o are the pressures inside and outside the bubble, respectively, R is the radius and σ the surface tension. Figure 7.7 plots the pressure difference (calculated by equation (7.68)) against $1/R$ using the following choice of parameters: $\rho_r = \rho_b = 1$, $A_r = A_b = 0.001$ $\alpha_r = 0.1$. The numerical measurements are shown by the $\diamond$ symbols and the solid line is a linear fit passing through the origin, the slope of which gives the surface tension. The straight line is seen to be an excellent fit to the predicted pressure difference,

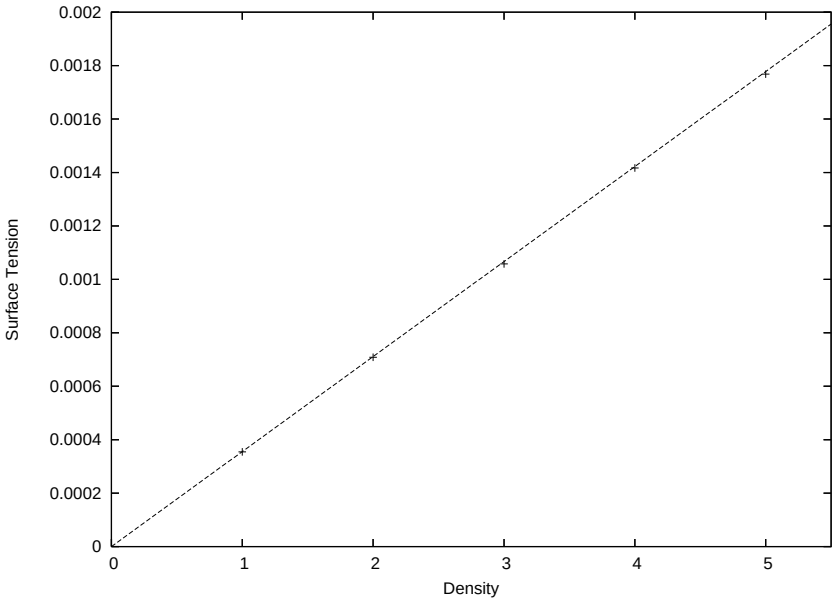

Figure 7.6: The numerical measurements (+) and theoretical predictions (solid line) of surface tension as a function of density.

thus demonstrating the models ability to predict surface tension.

7.3.3 Macroscopic Equations of Motion

Although the addition of the two-phase component of the collision operator (7.73) enables the lattice Boltzmann model to simulate some multi-phase problems [15], the validity of the operator is not well understood. More specifically, its ability to handle flows with substantially different densities is untested and the theoretical considerations are incomplete.

A collision operator of the form (7.73) or (7.76) aims at a discretisation of the term involving the distributed stress tensor because the colour gradient is an approximation of the derivative of a jump condition. However, it can be shown that equation (7.73) does not recover the correct form of the macroscopic force term after applying the Chapman-Enskog analysis. We will show, however, that a modification of the lattice Boltzmann collision operator can recover the correct form of the macroscopic equations. A single phase version of the Navier-Stokes equations are derived containing an

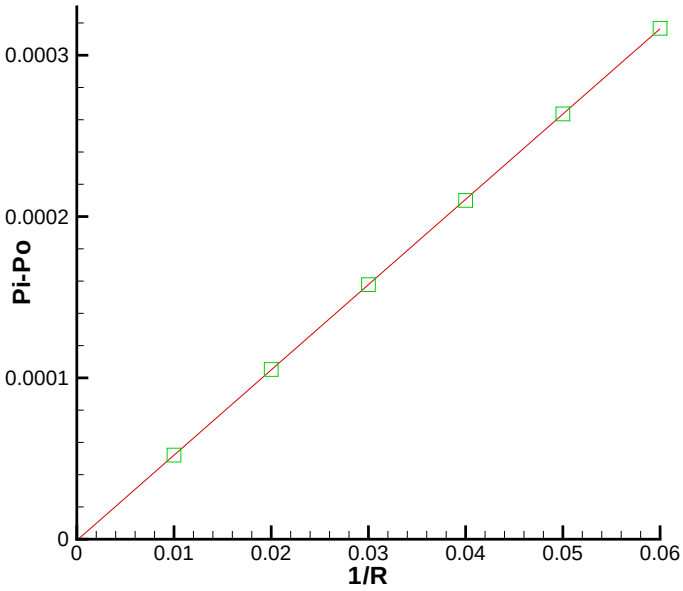

Figure 7.7: The numerical measurements $\diamond$ and theoretical predictions (solid line) of Laplace's law for surface tension.

appropriate source term, localized to the vicinity of the interface, to account for surface tension effects.

Since the two-phase collision operator $\left(\Omega_i^k\right)^{(2)}$ vanishes in regions containing just one fluid, the standard Chapman-Enskog analysis can be employed for each pure phase and the Navier-Stokes equations can be derived. At an interface the two-phase operator, $(\Omega_i^k)^{(2)}$ enters the analysis and a Taylor and Chapman-Enskog expansion of equation (7.53) yields, to first order in ϵ:

$$\partial_{t_1} N_i^{(0)} + c_{i\alpha}\partial_\alpha N_i^{(0)} = -\omega N_i^{(1)} + \Omega_i^{(2)}, \tag{7.116}$$

where we have summed the 'red' and 'blue' contributions. We note that in the above $\omega = \omega\phi$ is the averaged relaxation parameter defined in equation (7.85). The mass and momentum constraints yield:

$$\begin{aligned} \partial_{t_1}\rho + \partial_\alpha \rho u_\alpha &= 0; & (7.117)\\ \partial_{t_1}\rho u_\alpha + \partial_\alpha \Pi_{\alpha\beta} &= 0, & (7.118) \end{aligned}$$

respectively, where $\Pi_{\alpha\beta}$ is the momentum flux tensor, given by:

$$\begin{aligned} \Pi_{\alpha\beta} &= \sum_{i=0}^{9} N_i^{(e)} c_{i\alpha} c_{i\beta}, & (7.119)\\ &= p_0\delta_{\alpha\beta} + \rho u_\alpha u_\beta, & (7.120) \end{aligned}$$

where the pressure $p_0 = p_0^r + p_0^b$, is found from equation (7.68).

After the application of the mass constraint to the second order expansion of equation (7.53) we obtain:

$$\partial_{t_2}\rho = 0; \tag{7.121}$$

and combining this with the first order results shows that

$$\partial_t \rho + \nabla\cdot\rho\mathbf{u} = 0. \tag{7.122}$$

Application of the momentum constraint to the second order equation leads to the relation:

$$\partial_{t_2}\rho u_\alpha + \partial_\beta Q_{\alpha\beta} + \frac{1}{2}\partial_{t_1}\partial_\beta \Pi_{\alpha\beta} + \frac{1}{2}\partial_\beta\partial_\gamma P_{\alpha\beta\gamma} = 0, \tag{7.123}$$

where $P_{\alpha\beta\gamma} = \sum_i N_i^{(0)} c_{i\alpha}c_{i\beta}c_{i\gamma}$ and $Q_{\alpha\beta} = \sum_i N_i^{(1)} c_{i\alpha}c_{i\beta}$. The two-phase operator dictates the following form of the tensor $Q_{\alpha\beta}$:

$$Q_{\alpha\beta} = -\frac{1}{\omega}\left(\partial_{t_1}\Pi_{\alpha\beta} + \partial_\gamma P_{\alpha\beta\gamma} - \sum_i \Omega_i^{(2)} c_{i\alpha}c_{i\beta}\right), \tag{7.124}$$

and therefore we find that

$$\partial_{t_2}\rho u_\alpha + \partial_\beta\left(\frac{1}{2} - \frac{1}{\omega}\right)\left[\partial_{t_1}\Pi_{\alpha\beta} + \partial_\gamma P_{\alpha\beta\gamma}\right] + \partial_\beta \frac{1}{\omega}\sum_i \Omega_i^{(2)} c_{i\alpha}c_{i\beta} = 0. \tag{7.125}$$

Now, adding equations (7.118) and (7.125) and using vector notation we find that

$$\partial_t \rho\mathbf{u} + \nabla\cdot(\rho\mathbf{u}\mathbf{u}) = -\nabla p_0\mathbf{I} + \nu\left[\nabla^2(\rho\mathbf{u}) + \nabla\nabla\cdot(\rho\mathbf{u})\right] - \nabla\cdot\mathbf{S}, \tag{7.126}$$

where

$$\begin{aligned} S_{\alpha\beta} &= \frac{1}{\omega}\sum_i \Omega_i^{(2)} c_{i\alpha}c_{i\beta} && (7.127)\\ &= \frac{A|\mathbf{F}|}{\omega}\left(\frac{1}{|\mathbf{F}|^2}\sum_i W_i(\mathbf{c}_i\cdot\mathbf{F})^2 c_{i\alpha}c_{i\beta} - \sum_i B_i c_{i\alpha}c_{i\beta}\right) && (7.128)\\ &= \frac{A|\mathbf{F}|}{\omega}\left(\frac{1}{9|\mathbf{F}|^2}F_\gamma F_\delta(\delta_{\alpha\beta}\delta_{\gamma\delta} + \delta_{\alpha\gamma}\delta_{\beta\delta} + \delta_{\alpha\delta}\delta_{\beta\gamma}) - \frac{1}{3}\delta_{\alpha\beta}\right) && (7.129) \end{aligned}$$

which can be written as

$$\mathbf{S} = \frac{2A}{9\omega|\mathbf{F}|}\begin{pmatrix} -F_y^2 & F_xF_y \\ F_xF_y & -F_x^2 \end{pmatrix}. \tag{7.130}$$

The additional term in the Navier-Stokes equation viz. $\nabla \cdot \mathbf{S}$, arises from the effect of surface tension and can be expressed in terms of the fluid composition. The fluid composition is modelled using the colour difference, $\bar{\rho}$, which plays the role of an order parameter.

In the lattice Boltzmann model for immiscible fluids described here and elsewhere there are three fluid regions: homogeneous red and blue regions and a thin region near the interface where the two fluids mix. The method will not recover a sharp interface, i.e. one of zero thickness, but instead produce what is known as a 'diffuse' interface. Diffuse interface ideas were developed by Rayleigh [34] and by van der Waals [66], who proposed gradient theories for the interface based on the principles of thermodynamics. In diffuse interface models [1] a capillary stress tensor is used to model the interface between the two fluids. In this way a theory of the interface based on continuum mechanics may be developed and a modified Navier-Stokes equation can be derived with an additional term that accounts for surface tension (see Anderson et al. [1], for example). The capillary tensor, $\mathbf{\Gamma}$, has the following form in terms of the colour difference:

$$\mathbf{\Gamma} \sim |\nabla\bar{\rho}|^2\mathbf{I} - \nabla\bar{\rho} \otimes \nabla\bar{\rho} \simeq |\mathbf{F}|^2\mathbf{I} - \mathbf{F} \otimes \mathbf{F}, \tag{7.131}$$

where $\otimes$ denotes the outer product between two vectors.

Suppose that ρ_r and ρ_b are smooth functions that decay rapidly to zero in the interfacial region. Since $\bar{\rho}$ approximates a jump function, the surface delta distribution δ_s, defined by

$$\langle \delta_s, \phi \rangle = \int_s \phi \ \ ds,$$

where s is the interface between the two phases, satisfies $\delta_s \approx C|\mathbf{F}|$ where C is the inverse of the jump height. The surface distribution δ_s is only non-zero within a finite thickness transitional region near the interface since $\mathbf{F} = \mathbf{0}$ in

pure phases. Therefore we can express the tensor $\mathbf{S}$ in the form

$$\begin{aligned}\mathbf{S} &= \frac{2A}{9\omega}\left(\mathbf{I} - \frac{\mathbf{F}\otimes\mathbf{F}}{|\mathbf{F}|^2}\right)|\mathbf{F}| \\ &= \frac{2A}{9\omega C}(\mathbf{I} - \mathbf{n}\otimes\mathbf{n})\delta_s\end{aligned}$$

To first order in $\mathbf{u}$, A/ω is approximately proportional to σ, and therefore we have

$$\mathbf{S} = B\sigma(\mathbf{I} - \mathbf{n}\otimes\mathbf{n})\delta_s, \tag{7.132}$$

where B is a constant. We note that

$$\nabla_s \cdot (\mathbf{I} - \mathbf{n}\otimes\mathbf{n})\delta_s = \kappa\mathbf{n}\delta_s,$$

where κ is the mean radius of curvature of the interface defined by

$$\kappa = -\nabla_s \cdot \mathbf{n}.$$

Note that the constant B in (7.132) can be replaced with unity by scaling the two-phase collision operator (7.76) by an appropriate factor.

7.4 Numerical Simulations

Poiseuille Flow

We first verify our model for Poiseuille flow of layered immiscible fluids. Consider two incompressible immiscible fluids moving under the influence of a pressure gradient G in the x-direction. If the flow is sufficiently small so that no instabilities occur with the interface remaining in the center of the channel at all times then the analytic solutions for the steady flow are found

to be

$$u^r = \frac{Gh^2}{2\mu_r}\left[-\left(\frac{y}{h}\right)^2 + \frac{y}{b}\left(\frac{\mu_r-\mu_b}{\mu_r+\mu_b}\right) + \frac{2\mu_r}{\mu_r+\mu_b}\right], \quad -h \le y \le 0, \tag{7.133}$$

$$u^b = \frac{Gh^2}{2\mu_b}\left[-\left(\frac{y}{h}\right)^2 + \frac{y}{b}\left(\frac{\mu_r-\mu_b}{\mu_r+\mu_b}\right) + \frac{2\mu_b}{\mu_r+\mu_b}\right], \quad 0 \le y \le h, \tag{7.134}$$

where h is the half channel width and μ_r and μ_b are the shear viscosities for red and blue fluids, respectively.

A horizontally periodic 128×65 lattice with a no-slip condition on the upper and lower walls was initialised with the upper half of the channel consisting of pure red fluid and the lower half pure blue. The centre line initially contained an equal number of each particle type. Both fluids were of unit density with $\omega_b = 0.795229$, $\omega_r = 0.360685$ (corresponding to viscosities $\mu_b = 0.2525$, $\mu_r = 0.75775$). We also set $\alpha_r = 0.1$, $\delta = 0.1$, $A_r = A_b = 0$. Initially the system was at rest and a small force G was used to mimic the pressure gradient and drive the flow based on the velocity u_I at the center:

$$u_I = \frac{gh^2}{\mu_r + \mu_b} = 0.045 \tag{7.135}$$

Figure 7.8 plots the analytic solution (solid line) and lattice Boltzmann prediction (+) of the velocity profile. We see a very good agreement between the numerical and analytical predictions.

To demonstrate the role of the relaxation parameter, δ, we perform the layered Poiseuille flow simulation as outlined above with δ=0.01, 0.3, 0.5, 0.7, and 0.9. Figure 7.9 plots the velocity profile when $\delta = 0.9$. Compared with Figure 7.8, we see a smoother curve in the neighbourhood of the interface and a further departure from the analytical solution in this region. Table 7.1 shows the computed value of velocity at the points $y = -h/2$, $y = 0$ and $y = h/2$ for each value of δ alongside the relative error between these and the

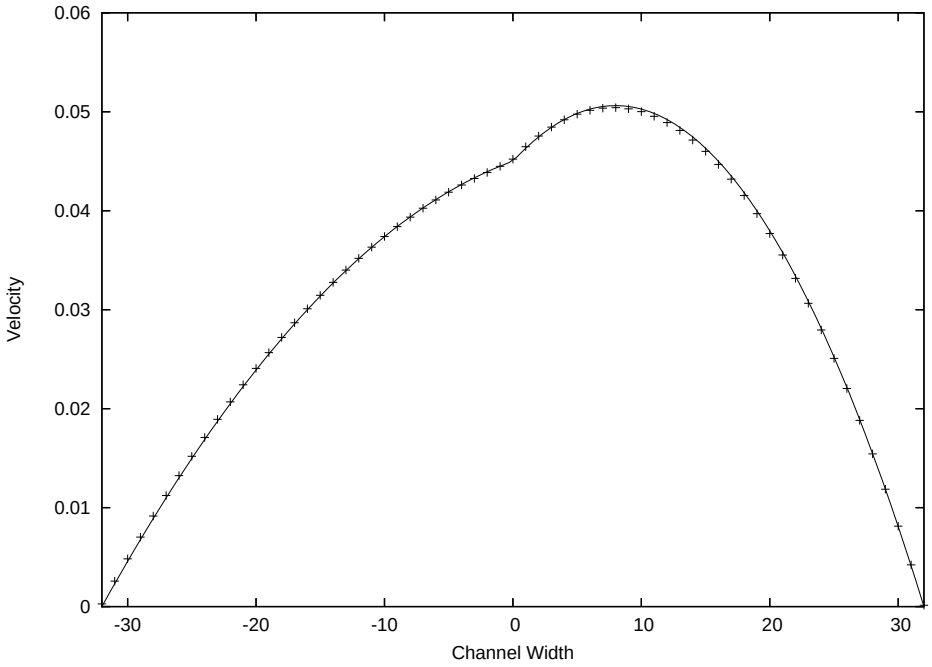

Figure 7.8: Analytic and numeric (+) measurements of velocity of two adjacent immiscible fluids.

analytical values. It is clear that as δ increases the relative error increases, hence our choice of $\delta = 0.1$ in the simulations that follow.

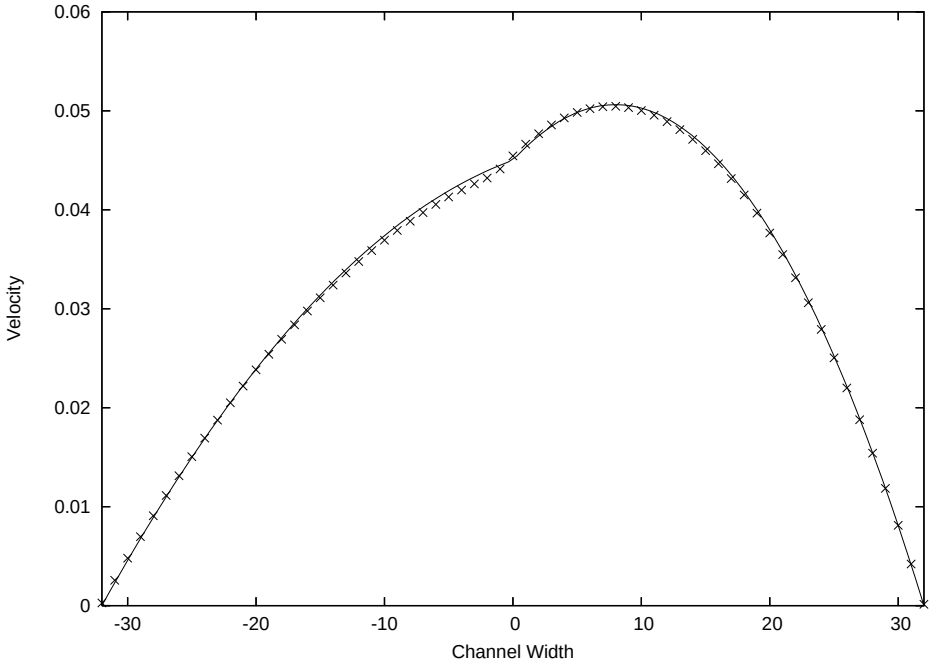

Figure 7.9: Analytic and numeric (+) measurements of velocity of two adjacent immiscible fluids when $\delta = 0.9$.

To demonstrate the effect the domain size has on the numerical calculations increased the number of lattice points in the transverse direction and ran the Poiseuille flow simulation as described above and measured the velocity at three different positions, $y = -h/2$, $y = 0$ and $y = h/2$. Table 7.2 shows the computed value of velocity at these points for the original mesh (as used above) and the six refined meshes, alongside the relative error between these and the analytical values. We notice the velocity in the lower half of the channel (which contains the slower moving, more viscous fluid) is less dependent on the mesh dimensions then the velocity in the upper half and maintains a value of 0.03021 for all tested domains with $nx > 128$. The less viscous fluid does not appear to be overly sensitive to the mesh dimensions but it is important to note that an increase in the number of lattice points in the transverse direction has a positive effect on the accuracy of the

δ	$u(-h/2)$	$u(0)$	$u(h/2)$
0.01	0.03020	0.0451	0.04490
error (%)	0.5	0.2	0.2
0.1	0.03021	0.0451	0.04490
error (%)	0.5	0.2	0.2
0.3	0.0306	0.04520	0.0457
error (%)	2	0.4	1.56
0.5	0.0306	0.0454	0.0457
error (%)	2	0.89	1.56
0.7	0.0306	0.0458	0.0457
error (%)	2	1.78	1.56
0.9	0.0297	0.0459	0.0458
error (%)	1	2	1.78

Table 7.1: Comparison of velocity for 2-layer Poiseuille flow using different values of δ. The exact values are (to three significant figures): $u(-h/2) = 0.03$; $u(0) = u(h/2) = 0.045$.

simulations.

Using the same value for the force g we measure the velocity of a flow that has one fluid sandwiched between another less viscous fluid (Figure 7.2). Apart from the initial configuration this lattice Boltzmann simulation is identical to one described above. The analytic solutions to this flow are given by

$$\begin{aligned} u^b &= \frac{G}{8}\left(\frac{3h^2}{\mu_r} + \frac{h^2 - 4y^2}{\mu_b}\right), \quad -h \le y \le -\frac{h}{2}, \\ u^r &= \frac{G}{2\mu_r}\left(h^2 - y^2\right), \quad -\frac{h}{2} \le y \le \frac{h}{2}, \\ u^b &= \frac{G}{8}\left(\frac{3h^2}{\mu_r} + \frac{h^2 - 4y^2}{\mu_b}\right), \quad \frac{h}{2} \le y \le h \end{aligned}$$

and in Figure 7.10 we plot the velocity predicted by the analysis (solid line) and the numerics (+). Once again we see the results to be in good agreement.

Mesh Dimensions	$u(-h/2)$	$u(0)$	$u(h/2)$
128×65	0.03021	0.0451	0.04490
error (%)	0.5	0.2	0.2
128×85	0.03023	0.0452	0.0457
error (%)	0.77	0.4	1.56
168×85	0.03021	0.0454	0.0437
error (%)	0.5	0.89	2.9
168×105	0.03021	0.0447	0.0445
error (%)	0.5	0.67	< 0.1
208×105	0.03021	0.0452	0.0448
error (%)	0.5	0.4	0.4
208×125	0.03021	0.0451	0.0449
error (%)	0.5	0.2	0.2
248×125	0.03021	0.0451	0.0449
error (%)	0.5	0.2	0.2

Table 7.2: Comparison of velocity on different meshes for 2-layer Poiseuille flow. The exact values are (to three significant figures): $u(-h/2) = 0.03$; $u(0) = u(h/2) = 0.045$.

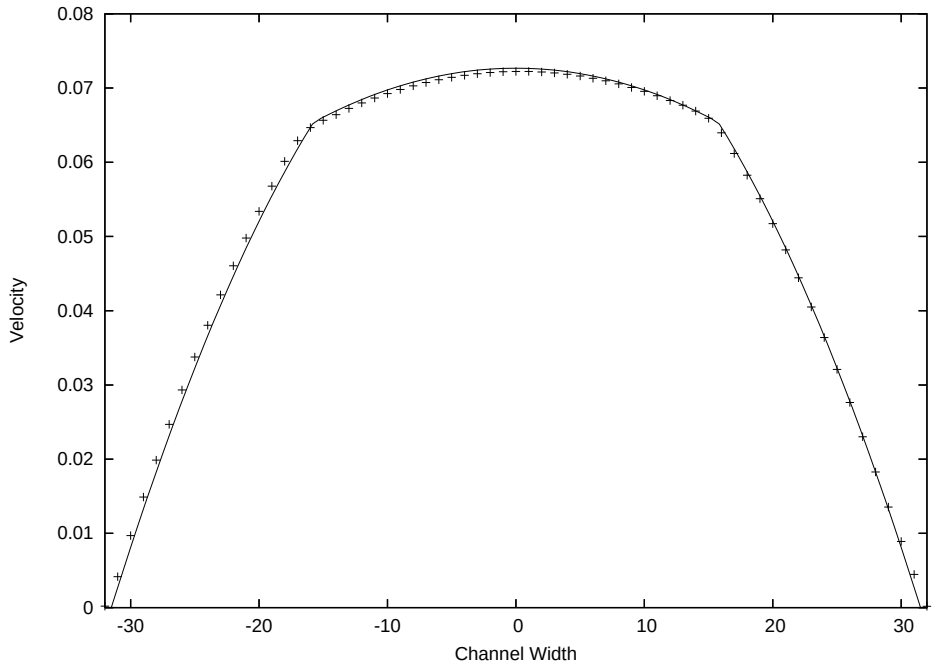

Figure 7.10: Analytic (solid line) and numeric (+) measurements of velocity in a three-layer Poiseuille flow.

Spinodal Decomposition

Our next test is for spinodal decomposition. A 64×64 lattice domain with a no-slip condition on the horizontal walls and periodic conditions on the vertical boundaries was initialised with red and blue particles randomly distributed. The density ratio, ρ_r/ρ_b, was set to $2/3$ with $\omega_r = \omega_b = 1$. The other input parameters were: $A = 0.0001$; $\alpha_r = 0.1$ and $\delta = 0.1$. There was no body force driving the flow. Figures 7.11 to 7.14 plot distribution of colour mass using white to represent the more dense fluid and black the less dense. Any grey area signify interfacial regions containing both particle types. In Figure 7.11 we see how layers of fluid emerge and join to form larger, more distinct areas of different phases. Figure 7.12 shows bubble-like features developing due to the random internal motion of particles caused by the local density gradient. The snapshots at times $t = 5000$ and $t = 7000$ show how some of these 'bubbles' collide or break free to form larger areas and Figure 7.13 shows the system in its equilibrium state. Two distinct phases are observed here and snapshots taken after $t = 10000$ show no visible difference in the configuration of fluids.

The theoretical problem of finding the position of a fluid-fluid interface has non-unique solutions. However, experimental observations show immiscible fluids of the same density form spheres of one fluid within another. A stability analysis along with a study of the dynamics of rotating binary mixtures predicts the same phenomenon [28]. We test our model against these findings by adjusting the material parameters of the spinodal decomposition simulation discussed above. Starting with a random mixture of fluid in a fully periodic 64×64 domain with $\rho_r = \rho_b = 1$, $\omega_r = 0.360685$, $\omega_b = 0.795229$ (corresponding to viscosities $\nu_r = 0.7575$, $\nu_b = 0.2525$), $A = 0.0001$, and $\alpha_r = 0.1$ we view the fluid configuration at various time steps. It is important to note that the mass of each species did not change throughout this experiment. In Figure 7.15 we see how a mixture of two liquids of different viscosities evolves into a stationary configuration with one large low viscous bubble immersed in a more viscous fluid. This result seems to agree with the ideas of Renardy and Joseph [28]:

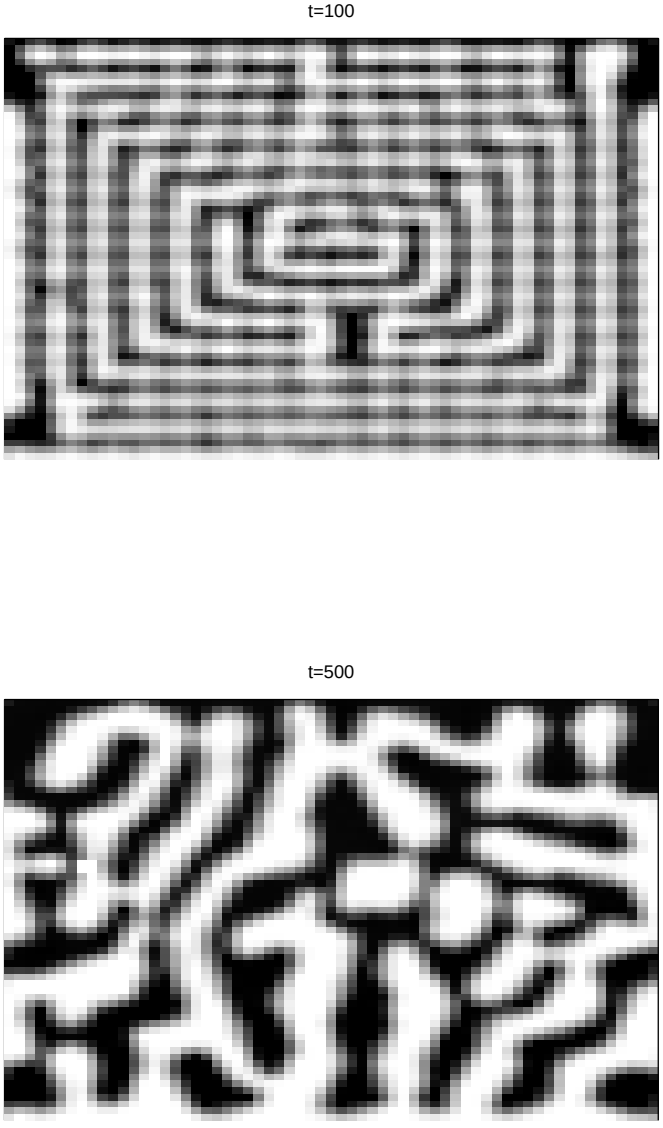

Figure 7.11: Distribution of colour at times $t = 100$ and $t = 500$.

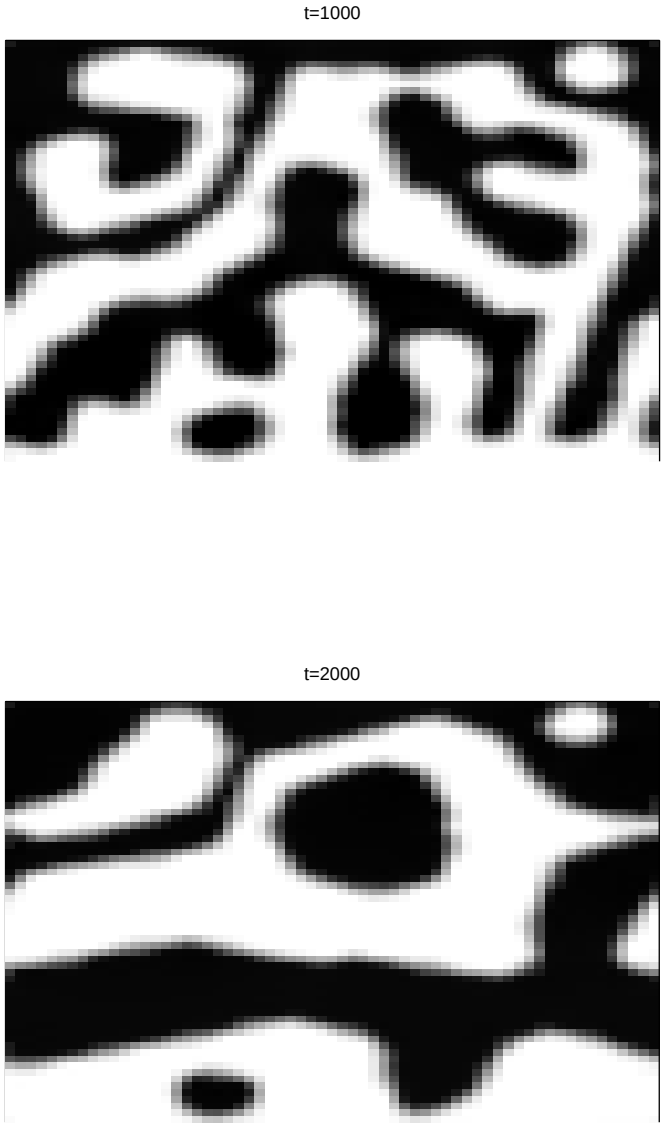

Figure 7.12: Distribution of colour at times $t = 1000$ and $t = 2000$.

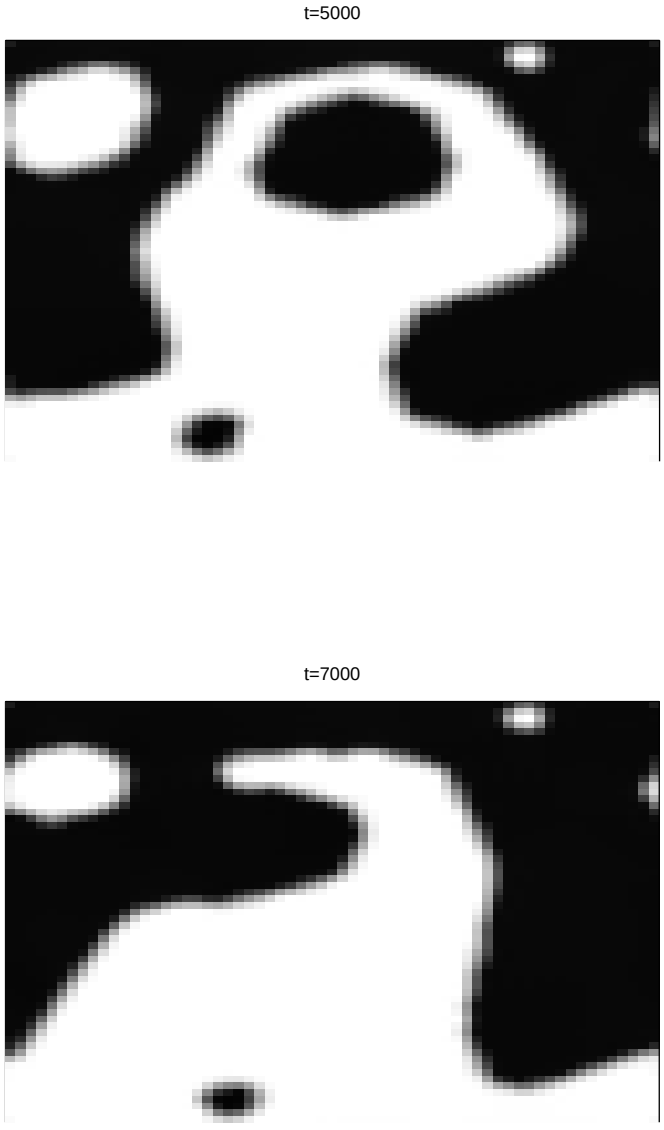

Figure 7.13: Distribution of colour at times $t = 5000$ and $t = 7000$.

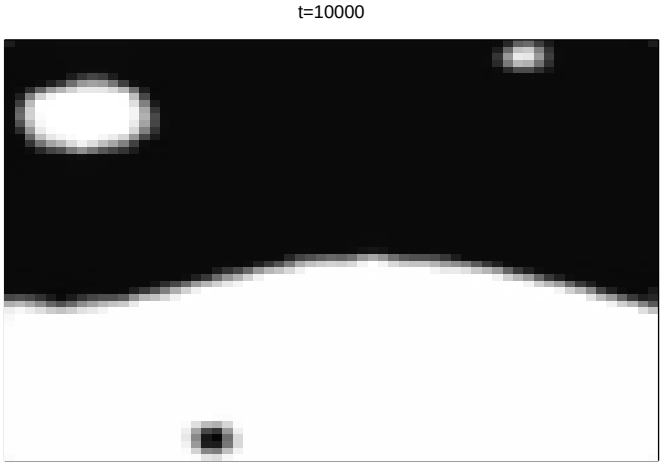

Figure 7.14: Distribution of colour at time $t = 10000$. The system is now in equilibrium.

> Perhaps there is a selection mechanism based on the stability to large disturbances, in which the stable configuration is the one that minimizes the surface area. This type of criterion would lead to large bubbles, even one large bubble, rather than many small ones.

Non-equilibrium Rod

When a rod or cylindrical drop of one fluid is immersed in another, surface tension causes it to deform and capillary waves are induced that make the drops surface oscillate about its equilibrium shape. This behaviour can be observed in numerical calculations by surrounding an initially square droplet of one fluid with another and monitoring its response. To perform this test with our model we let a 32×32 square of red fluid centered in a 64×64 grid evolve in time. The parameters chosen for this flow were:

$$\begin{aligned} \rho_r &= 2, \\ \rho_b &= 1, \\ \nu_r = \nu_b &= 1, \\ A_r = A_b &= 0.01, \\ \alpha_r &= 0.5, \\ \delta &= 0.1. \end{aligned}$$

The initial configuration is shown in Figure 7.17 and we take snapshots of the flow at different time-steps. After 140 time-steps surface tension has caused the corners (which are the areas of high curvature) to collapse, which in turn pushes the center of the vertices outward, resulting in diamond-like formation (as in Figure 7.18). Surface forces are then strong in these new areas of high curvature, thus setting the drop into oscillation. This behaviour is observed in Figures 7.19 and 7.20 which show the red drop collapsing back to a smoothed square ($t = 300$) before returning to a smoothed "diamond" shape. The frequency of this oscillation decreases in time and Figure 7.21

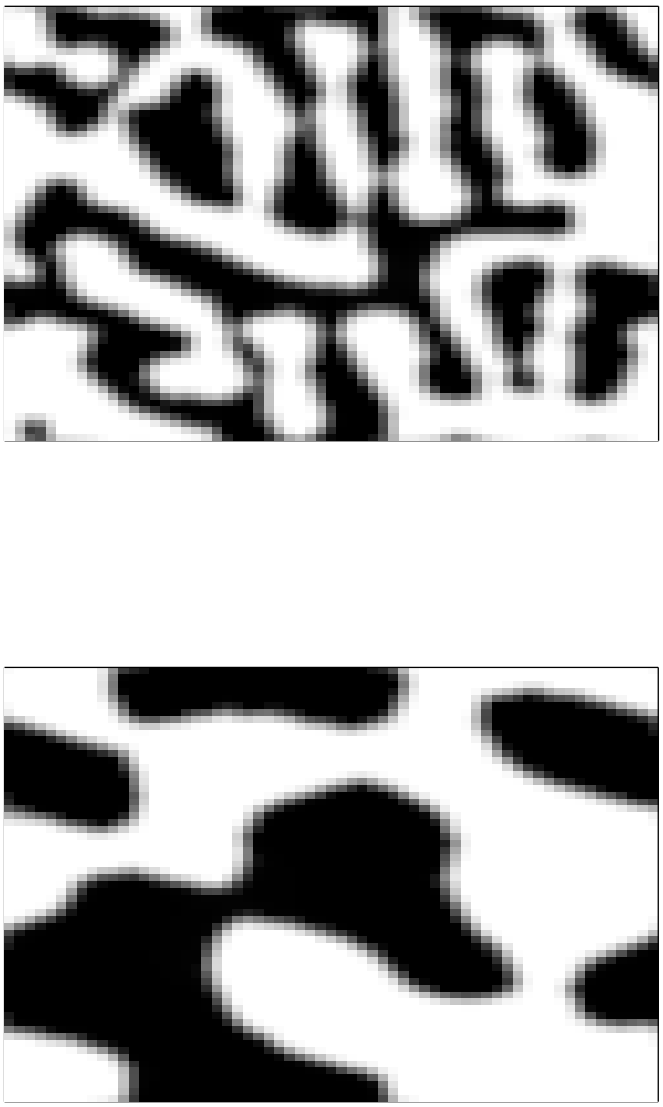

Figure 7.15: Distribution of colour at times $t = 1000$ and $t = 3000$. The white fluid is the more viscous.

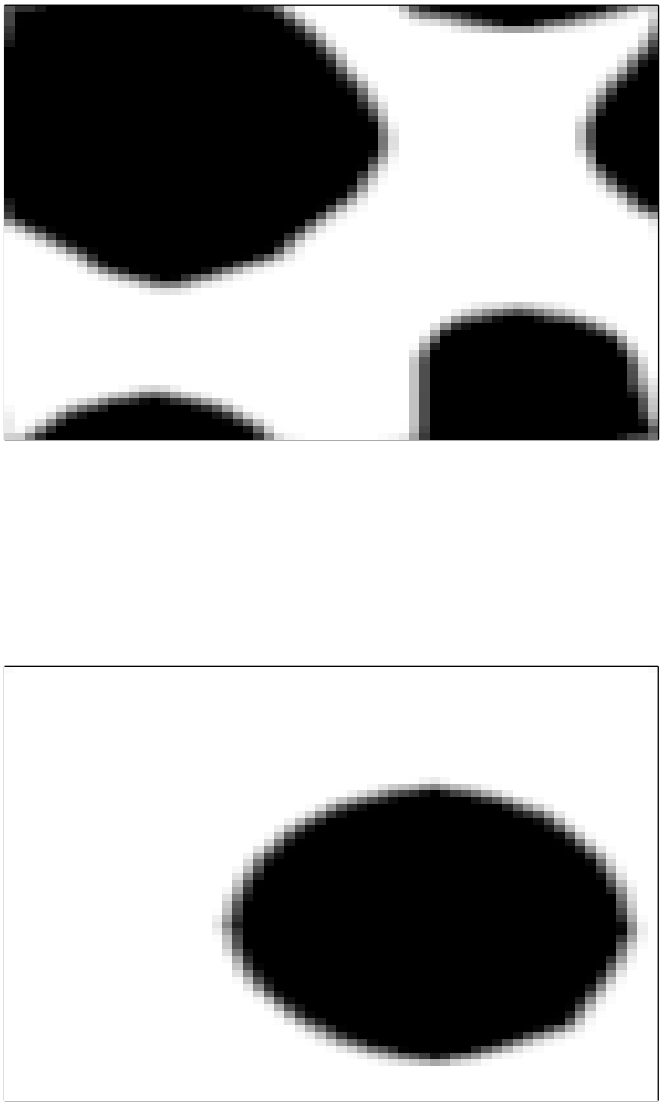

Figure 7.16: Distribution of colour at times $t = 15000$ and $t = 30000$. The black fluid has been encapsulated by the white.

shows that by 800 time-steps the red fluid has found its equilibrium spherical shape. The final radius of the bubble is approximately 18.061, which shows its area is almost identical to the initial square configuration.

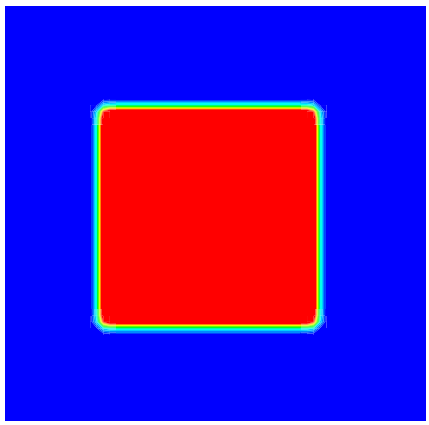

Figure 7.17: Initial configuration for the non-equilibrium rod test.

To demonstrate mesh convergence we construct three additional meshes, one coarser and two finer than the one mentioned above. The coarse grid, $M0$, has dimensions 32×32 lattice units, $M1$ is the original grid (64×64) and the finer meshes, $M2$ and $M3$ have dimensions 128×128, and 256×256, respectively. The initial square droplet is half the size of the mesh and placed in the center of the domain in each case. Table 7.3 shows the number of degrees of freedom (DF) on each mesh and area of the initial square configuration. The column titled "Radius" gives the value of the final bubble radius required to preserve the area identically and "Error" refers to the relative error between this value and the measured radius. We see a excellent agreement between the required and measured radii on meshes $M1$, $M2$ and $M3$ showing that our 2 phase operator produces the desired surface tension effects while conserving mass. Mesh $M0$ was too coarse to produce any meaningful results. Although the initial square droplet began to deform in the expected manor the equilibrium state, which is shown in Figure 7.22,

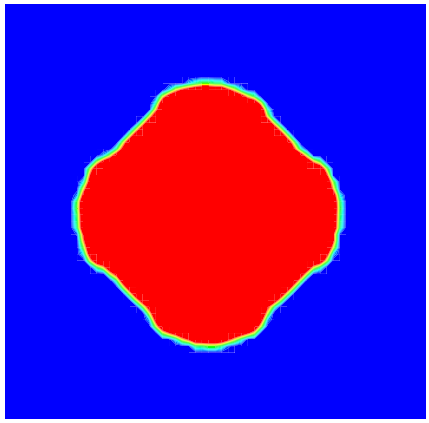

Figure 7.18: Configuration at time $t = 140$ for the non-equilibrium rod test.

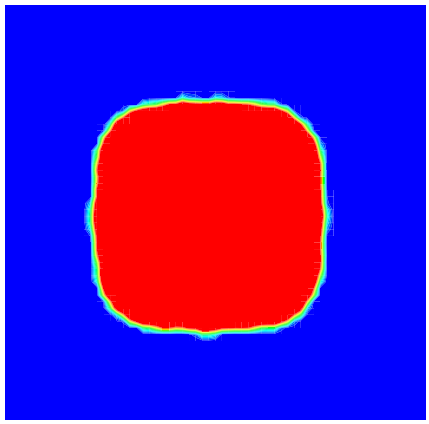

Figure 7.19: Configuration at time $t = 300$ for the non-equilibrium rod test.

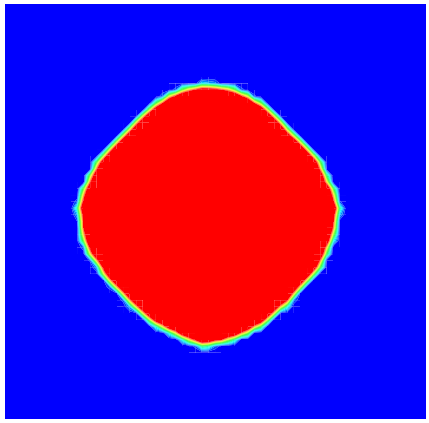

Figure 7.20: Configuration at time $t = 440$ for the non-equilibrium rod test.

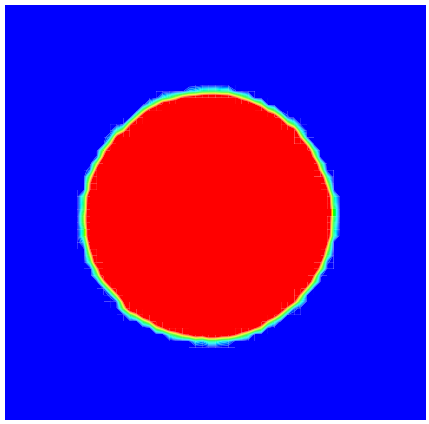

Figure 7.21: Configuration at time $t = 800$ for the non-equilibrium rod test.

Mesh	DF	Area	Radius	Measured Radius	Error (%)
$M0$	1024	256	9.027	/	/
$M1$	4096	1024	18.054	18.061	0.061
$M2$	16384	4096	36.108	36.117	0.025
$M3$	65536	16384	72.216	72.59	0.5

Table 7.3: Comparison of measured radius on different meshes for the non-equilibrium rod test.

was not a perfect circle, thus making it difficult to calculate the final area.

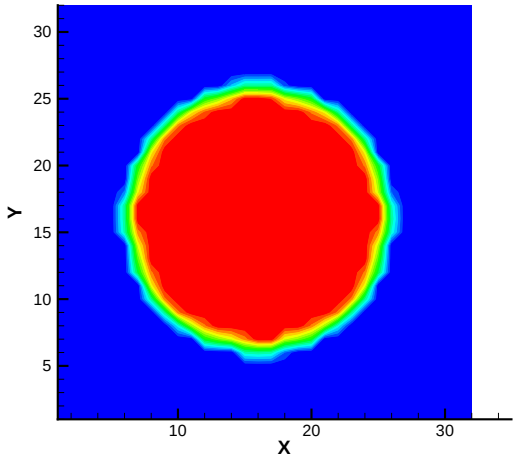

Figure 7.22: Final configuration of the non-equilibrium rod test on mesh $M0$.

Coalescence of Two Bubbles

For a large density ratio test we look at the coalescence of two identical circular droplets. Two red bubbles of radius $R = 18.2$ and density $\rho_r = 2.261$ are placed very close together in the center of a 100×100 computational domain. The surrounding fluid is blue with density $\rho_b = 0.122$, giving a density ratio of $\gamma = 18.5$. To unsure a stable interface we set $\alpha_r = 0.95$ and the other parameters are: $\nu_r = \nu_b = 1$ and $A_r = A_b = 0.008$. The initial configuration is shown in Figure 7.23 and as soon as the simulation

starts inter-molecular forces cause the bubbles to coalesce and we see in Figures 7.24 and 7.25 how the two droplets merge together. Like the non-equilibrium rod test, tension forces send the surface into oscillations before it reaches its equilibrium, as shown in Figures 7.26-7.29. The symmetries about the $x = nx/2$ and $y = ny/2$ are preserved and in agreement with other researchers' results [72]. The oscillation is clearly visible in Figure 7.30 which plots the droplet radius at $y = ny/2$ against time t. It is important to note that the relation $R_f = \sqrt{2}R_I$, where R_f is the final radius of the bubble and R_I the initial radius, is satisfied.

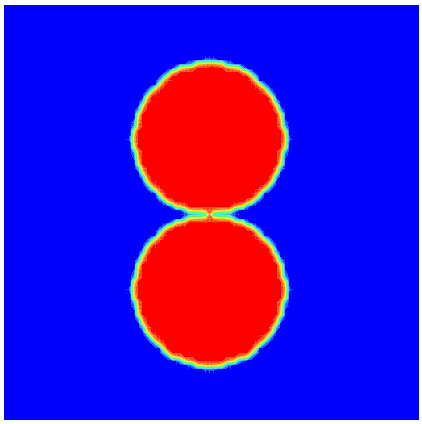

Figure 7.23: Initial configuration for the coalescence test.

To demonstrate mesh convergence we again construct three additional meshes, one coarser and two finer than the one mentioned above. The coarse grid, $M0$, has dimensions 50×50 lattice units, $M1$ is the original grid (100×100) and the finer meshes, $M2$ and $M3$ have dimensions 150×150, and 200×200, respectively. Table 7.4 shows the number of degrees of freedom (DF) on each mesh and the initial bubbles radius, R_I. The column titled "R_f" gives the value of the final bubble radius from the relationship $R_f = \sqrt{2}R_I$ and "Error" refers to the relative error between these two values. An improved accuracy with an increase in degrees of freedom is clearly seen.

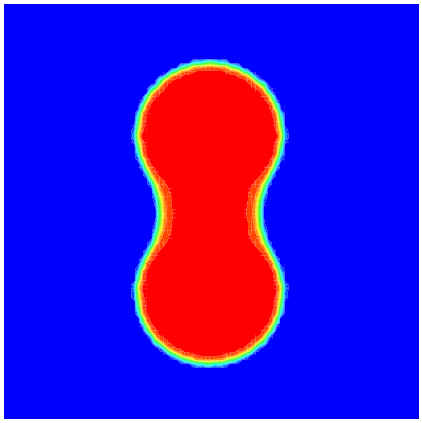

Figure 7.24: Configuration at time $t = 40$ for the coalescence test.

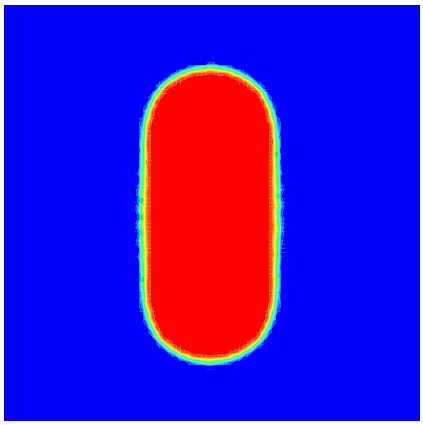

Figure 7.25: Configuration at time $t = 80$ for the coalescence test.

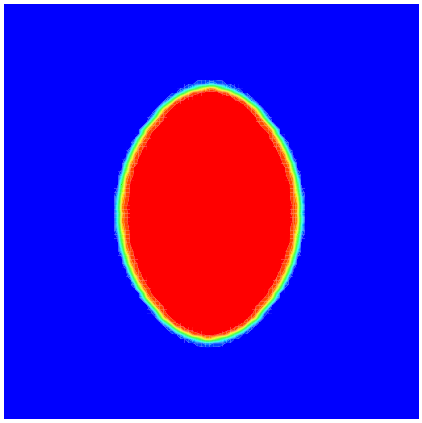

Figure 7.26: Configuration at time $t = 160$ for the coalescence test.

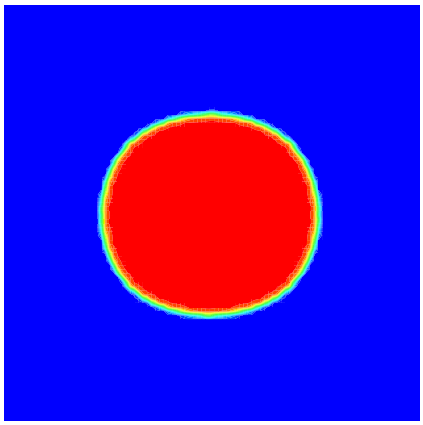

Figure 7.27: Configuration at time $t = 240$ for the coalescence test.

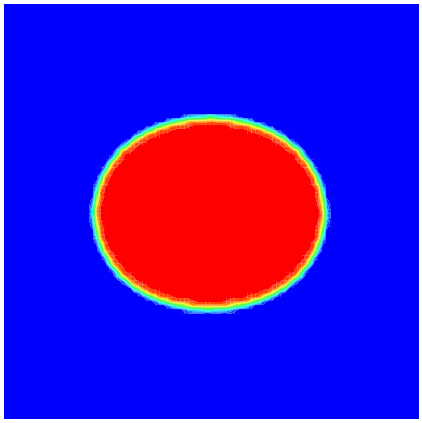

Figure 7.28: Configuration at time $t = 400$ for the non-equilibrium rod test.

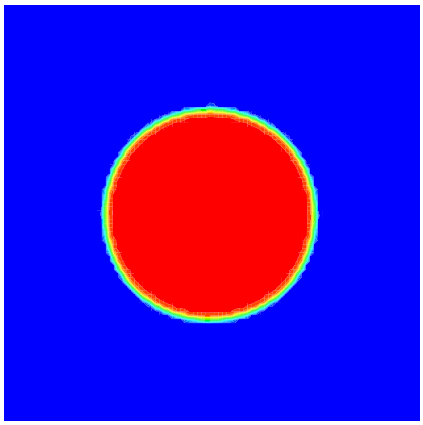

Figure 7.29: Configuration at time $t = 800$ for the non-equilibrium rod test.

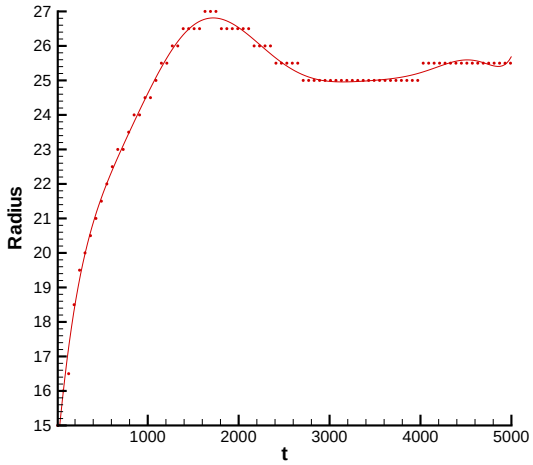

Figure 7.30: The radius of the coalescing bubble at $y = ny/2$ as a function of time. The solid line is a polynomial fit through the data points.

Mesh	DF	R_I	R_f	Measured Radius	Error (%)
$M0$	2500	9.1	12.87	12.73	1.1
$M1$	10000	18.2	25.74	25.69	0.19
$M2$	22500	27.3	38.61	38.59	0.05
$M3$	40000	36.4	51.48	51.5	0.04

Table 7.4: Comparison of measured radius on different meshes for the bubble coalescence test.

7.5 Axisymmetric Multi-Phase Flow

In Chapter 6 we showed how the single relaxation time lattice Boltzmann model in a two-dimensional Cartesian coordinate system can be extended by adding suitable source terms to recover the axisymmetric Navier-Stokes equations in the macroscopic limit. We now combine this with our two-phase model to give a lattice Boltzmann model for axisymmetric binary fluid flow.

From our arguments in Chapter 6 we know that the addition of a source term $S_i = \epsilon S_i^{(1)} + \epsilon^2 S_i^{(2)}$, where $S_i^{(1)}$ and $S_i^{(2)}$ are given by equations (6.41) and (6.42), respectively, to the LBGK equation accounts for axisymmetric effects in the model, and the addition of a two-phase collision operator, $\Omega_i^{k(2)}$, as defined in equation (7.76) incorporates surface tension effects into the LBE. Therefore, we propose a lattice Boltzmann equation of the form:

$$N_i^k\left(\mathbf{x}+\mathbf{c}_i, t+1\right) = N_i^k\left(\mathbf{x}, t\right) - \omega\left(N_i^k - N_i^{k(e)}\right) + \Omega_i^{k(2)} + S_i^k + T_i^k, \quad (7.136)$$

where S_i^k is the axisymmetric source term for fluid k and T_i^k is a new term that will be chosen to recover the additional two-component terms that arise in a cylindrical coordinate system.

From equation (7.126) we see the two-phase term in the momentum equation is $\nabla \cdot \mathbf{S}$. In axisymmetric cylindrical coordinates the divergence of a tensor $\mathbf{S}$ in component form is:

$$\left(\nabla \cdot \mathbf{S}\right)_r = \partial_r S_{rr} + \partial_z S_{rz} + \frac{S_{rr}}{r}, \quad (7.137)$$

$$\left(\nabla \cdot \mathbf{S}\right)_z = \partial_r S_{rz} + \partial_z S_{zz} + \frac{S_{rz}}{r}, \quad (7.138)$$

and if we perform the coordinate transformation $(r, z) \mapsto (y, x)$ we see that $T_i = T_i^{(r)} + T_i^{(b)}$ must be chosen such that in the macroscopic limit it recovers the following x and y components, respectively:

$$\frac{S_{xy}}{y} = \frac{2AF_xF_y}{9\omega y|\mathbf{F}|}, \quad (7.139)$$

$$\frac{S_{yy}}{y} = \frac{-2AF_x^2}{9\omega y|\mathbf{F}|}. \quad (7.140)$$

These terms are of order $O(\epsilon^2)$ so we see that $T_i = \epsilon^2 T_i^{(2)}$.

If the Chapman-Enskog expansion is applied to equation (7.136) then at $O(\epsilon)$ the mass and momentum constraints yield:

$$\partial_{t_2}\rho + \partial_\alpha \rho u_\alpha = \sum_i S_i^{(1)}; \tag{7.141}$$

$$\partial_{t_1}\rho u_\alpha + \partial_\beta \Pi_{\alpha\beta} = \sum_i S_i^{(1)} c_{i\alpha}, \tag{7.142}$$

which are identical to equations (6.13) and (6.14), respectively.

The second order mass equation is found to be

$$\partial_{t_2}\rho + \frac{1}{2}\partial_{t_1}\sum_i S_i^{(1)} = \sum_i S_i^{(2)} + \sum_i T_i^{(2)}. \tag{7.143}$$

Since surface tension effects do not alter the general form of the continuity equation we set $\sum_i T_i^{(2)} = 0$.

When the momentum conservation constraint is applied to the second order expansion of equation (7.136) the following relation is obtained:

$$\partial_{t_2}\rho u_\alpha + \partial_\beta Q_{\alpha\beta} + \frac{1}{2}\partial_{t_1}\partial_{t_1}\rho u_\alpha + \partial_{t_1}\partial_\beta \Pi_{\alpha\beta} + \frac{1}{2}\partial_\beta\partial_\gamma P_{\alpha\beta\gamma} = \sum_{i=0}^{8} S_i^{(2)} c_{i\alpha} + \sum_{i=0}^{8} T_i^{(2)} c_{i\alpha}, \tag{7.144}$$

where $\Pi_{\alpha\beta}$ and $P_{\alpha\beta\gamma}$ are as in Chapter 6 and

$$\begin{aligned} Q_{\alpha\beta} &= \sum_i N_i^{(1)} c_{i\alpha} c_{i\beta} \qquad (7.145) \\ &= -\frac{1}{\omega}\left[\partial_{t_1}\Pi_{\alpha\beta} + \partial_\gamma P_{\alpha\beta\gamma} - \sum_i \left(S_i^{(1)} - \Omega_i^{(2)} - T_i^{(2)}\right) c_{i\alpha} c_{i\beta}\right]. \end{aligned}$$

Since the required additional multi-phase components for axisymmetric flow do not include any derivatives we set $\sum_i T_i^{(2)} c_{i\alpha} c_{i\beta} = 0$. Therefore, there are

four necessary conditions that $T_i^{(2)}$ must satisfy:

$$\sum_i T_i^{(2)} = 0; \tag{7.146}$$

$$\sum_i T_i^{(2)} c_{ix} = \frac{2AF_xF_y}{9\omega y|\mathbf{F}|}; \tag{7.147}$$

$$\sum_i T_i^{(2)} c_{iy} = \frac{-2AF_x^2}{9\omega y|\mathbf{F}|}; \tag{7.148}$$

$$\sum_i T_i^{(2)} c_{i\alpha} c_{i\beta} = 0. \tag{7.149}$$

and one possible choice for $T_i^{(2)}$ that satisfies these conditions is

$$T_i^{(2)} = \frac{\Omega_i^{(2)} c_{iy}}{\omega y}. \tag{7.150}$$

We note that choosing $T_i^{(2)}$ in this way is consistent with the role of the two-phase lattice Boltzmann operator, i.e it serves to add mass to populations moving normal to an interface and remove mass parallel to it, and is also computationally efficient since the multi-phase terms can be conveniently written as $\Omega_i^{(2)}\left(1 + c_{iy}/(y\omega)\right)$. On the line $y = 0$, $|\mathbf{F}| = 0$ by the symmetry condition and therefore $\lim_{y\to 0} T_i^{(2)} = 0/0$. We evaluate this expression using L'Hôpital's rule and find $\partial_y|\mathbf{F}(x,0)| \simeq (|\mathbf{F}(x,-1)| - |\mathbf{F}(x,1)|)/2 = 0$ by symmetry, so that $T_i^{(2)} = 0$ when $y = 0$.

Adding the first and second order mass equations (equations (7.141) and (7.143)), and the first and second order momentum equations (equations (7.142) and (7.144)) yields the equations of motion for axisymmetric multi-phase flow:

$$\partial_\alpha u_\alpha = -\frac{u_y}{y}, \tag{7.151}$$

$$\begin{aligned} \frac{D\rho u_\alpha}{Dt} + \partial_\alpha P - \nu\rho\nabla^2 u_\alpha &= \frac{\nu\rho}{y}\partial_y u_\alpha - \frac{\nu\rho u_\alpha}{y^2}\delta_{\alpha y} \\ &+ \left(\nabla\cdot\mathbf{S}\right)_\alpha + \frac{S_{y\alpha}}{y}, \end{aligned} \tag{7.152}$$

where we have used the definitions of $S_i^{(1)}$, $S_i^{(2)}$, $\Omega_i^{(2)}$, and $T_i^{(2)}$ given by equations (6.41), (6.42), (7.76) and (7.150), respectively.

7.5.1 Laplace's Law

We apply our axisymmetric multi-phase lattice Boltzmann equation to verify Laplace's law (equation (7.115)) for surface tension. A 256×128 D2Q9 lattice domain is defined with periodic conditions applied to the vertical boundaries, the bounce-back scheme applied to the north wall and symmetry conditions on the south boundary. Axisymmetric drops of 6 different radii $R = 16.667, 20, 25, 33.333, 50, 100$ are centered on the line of symmetry and the following values for the flow parameters are used: $A_r = A_b = 0.0005$, $\omega_r = \omega_b = 1$, $\rho_r = \rho_b = 1$, $\alpha_r = \alpha_b = 0.1$, and $\delta = 0.1$. Figure 7.31 plots the pressure difference as a function of $1/R$. The numerical measurements are shown by the $\diamond$ symbols and the solid line is a linear fit passing through the origin, the slope of which gives the surface tension. The straight line is seen to be a good fit to the predicted pressure difference, thus demonstrating the model's ability to predict surface tension.

7.5.2 Non-Equilibrium Rod Test

The three dimensional extension of the non-equilibrium rod test, as described in Section 7.4, is performed. We construct an axisymmetric pipe of radius $r_1 = 64$ and height $h_1 = 128$. A cylindrical droplet of red fluid with radius $r_2 = 32$ and height $h_2 = 64$ is placed in the center and is surrounded by a blue fluid. The densities of the two species are: $\rho_r = 3$ and $\rho_b = 1$. The other flow parameters are $\omega_r = \omega_b = 1$, $A_r = A_b = 0.0005$, $\alpha_r = 0.9$ and $\delta = 0.1$. The initial configuration is shown in Figure 7.32. As in the two-dimensional case we expect surface tension forces to act at the areas of high curvature and cause the droplet to find its equilibrium shape, i.e. a sphere. Figure 7.33 shows the final droplet configuration, which we see to be a cross-section of a sphere. It is important to note that the final radius is $r_f \simeq 36.6$, showing that volume has been preserved.

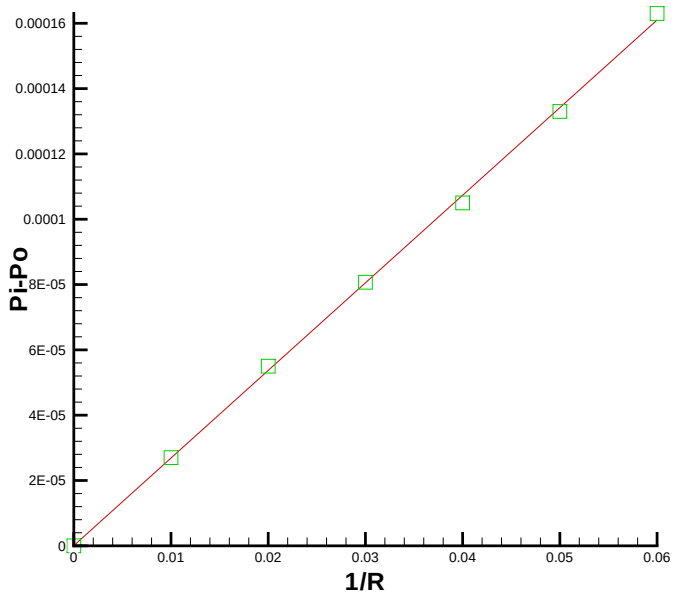

Figure 7.31: Plot of pressure difference as a function of the reciprocal of the radius of an axisymmetric droplet. The numerical predictions are denoted by the symbols.

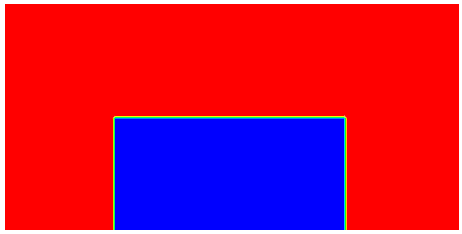

Figure 7.32: Initial configuration for the axisymmetric non-equilibrium rod test.

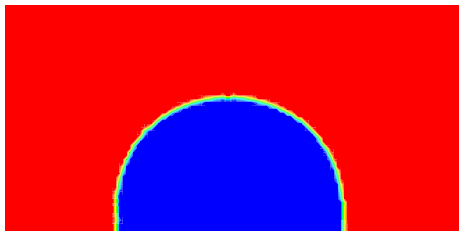

Figure 7.33: Final configuration for the axisymmetric non-equilibrium rod test.

Mesh	DF	Volume	Radius	Measured Radius	Error (%)
$M0$	2048	25736	18.315	/	/
$M1$	8192	205887	36.631	36.590	0.1
$M2$	32768	1647099	73.260	72.99	0.35
$M3$	131072	13176794	146.52	146.67	0.1

Table 7.5: Comparison of measured radius on different meshes for the non-equilibrium rod test.

To demonstrate mesh convergence we construct three additional meshes, one coarser and two finer than the one mentioned above. The coarse grid, $M0$, has dimensions 64×32 lattice units, $M1$ is the original grid (128×64) and the finer meshes, $M2$ and $M3$ have dimensions 256×128, and 512×256, respectively. The initial square droplet is half the size of the mesh and placed in the center of the domain in each case. Table 7.5 shows the number of degrees of freedom (DF) on each mesh and volume of the initial cylindrical configuration. The column titled "Radius" gives the value of the final bubble radius required to preserve the volume identically and "Error" refers to the relative error between this value and the measured radius. We see a excellent agreement between the required and measured radii on meshes $M1$, $M2$ and $M3$ showing that our axisymmetric 2 phase operator produces the desired surface tension effects while conserving mass. Mesh $M0$ was too coarse to produce any meaningful results.

7.5.3 Rising Bubble

We now present a preliminary simulation of a bubble of one fluid rising in a denser medium. A 128×64 D2Q9 mesh is constructed with a line of axisymmetry at $y = 1$. A bubble of blue fluid with density $\rho_b = 1$ and radius $r = 32$ is initially centered at $(50, 1)$. The surrounding red fluid has a density $\rho_r = 2$. Following Tölke et al. [65], a gravitational force $F_i = -gc_{iy}$ where $g = 1 \times 10^{-5}$ is the gravity acceleration is added to the LBE to induce the motion. No-slip conditions are applied to all boundaries other than the line of axi-symmetry.

Figure 7.34 plots the motion of the bubble at different time-steps. By

$t = 2500$ the bubble has lost its spherical shape and departed from its initial position. The shape is further deformed as the simulation proceeds and at $t = 10000$ the radial symmetry is clearly lost and the bubble has risen up the pipe. These are only preliminary results to shown qualitatively that this model can produce the desired effects under gravity. Further, more in-depth studies should be conducted to show if the proposed LBE can predict more detailed features such as the bubbles terminal velocity and final shape which can be characterised by the viscosity ratio, Eötvös number, Morton number and Reynolds number [65].

7.6 Discussion

In this chapter, a Rothman-Keller type lattice Boltzmann model has been developed for immiscible binary fluids using a D2Q9 lattice. An equilibrium function and collision operator for each phase has been derived, allowing each fluid to have to have its own density and viscosity while at the same time satisfying the necessary conservation laws and symmetry conditions. A Chapman-Enskog analysis shows that our modified two-phase collision operator recovers the correct form of the Navier-Stokes equations for binary fluids in the macroscopic limit. A theoretical expression for surface tension has been derived from this model and shown to be in excellent agreement with numerical measurements. The macroscopic governing equations are satisfied by the mesoscopic evolution of each phase.

The model was first used to study Poiseuille flow in a two-dimensional channel for two and three layer configurations of immiscible fluids. Good agreement with the analytical solution was obtained in both cases and a greater accuracy was obtained when the number of lattice nodes in the transverse direction was increased. The three layer configuration maximises the mass flux for a given pressure gradient [28]. Using a body force of the same magnitude a greater maximum velocity is obtained than in the two layer configuration.

The thickness of the interface between the two fluids is controlled by the value of the free parameter, δ. Sharp interfaces are achieved by choosing small

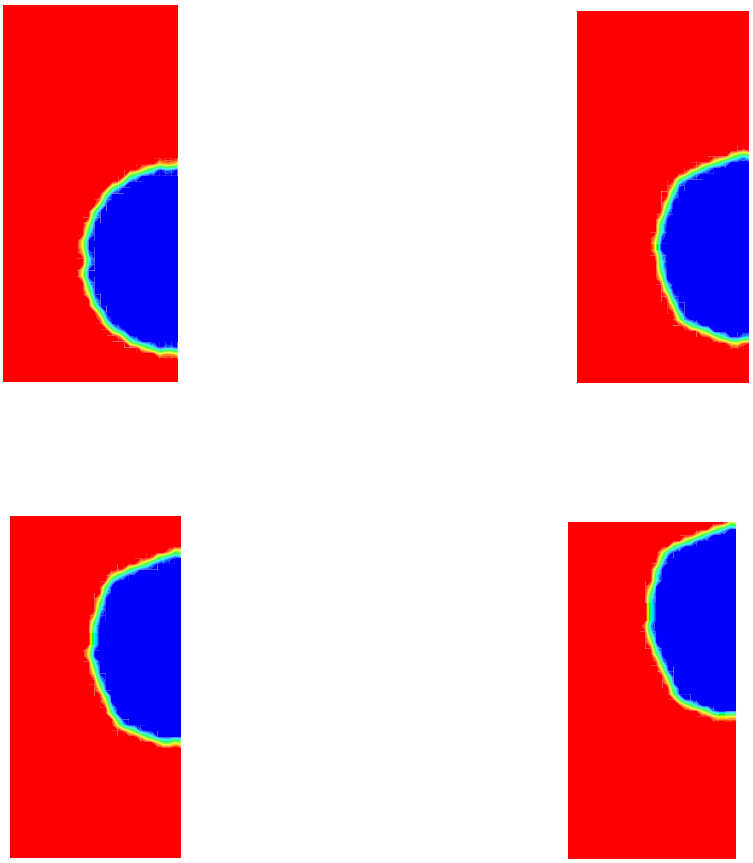

Figure 7.34: Motion of a bubble under the influence of gravity at times $t = 100$ (top left) $t = 2500$ (top right), $t = 5000$ (bottom left), and $t = 10000$. The surrounding fluid is the more dense.

values of δ while values close to unity lead to the interface being spread over several lattice cells. The results here were generated using $\delta = 0.1$. Larger values caused too much smearing of the interface and resulted in a less accurate prediction of the velocity profile near an interface. The model was then used to simulate the spinodal decomposition of a binary mixtures. In the case of a mixture of two fluids with the same density but different viscosities the model predicts that, in equilibrium, one large low viscous bubble is surrounded by the more viscous fluid. This prediction agrees with the analysis of Joseph and Renardy [28] who show, using rigorous mathematical arguments, that stable solutions to the equations for rigid motions of two liquids can be framed as a minimisation of energy problem, the only global solution to which is one large sphere.

We have also performed simulations to demonstrate that this model can predict binary flows with much larger density ratios than other R-K type LBM's. When the two fluids have different densities interface stability is maintained by the free parameter, α_r. Large density variation can be obtained provided the bounds on α_r are respected. Both the non-equilibrium rod test and the coalescence of two identical bubbles test were completed successfully and the results have led us to believe that our modified collision operator can capture qualitative and qualitative two-phase flow phenomena. We have written a journal article containing all this material and it has been published in the Journal of Physics A: Mathematical and Theoretical [54]. Finally, an axisymmetric multiphase lattice Boltzmann model has been proposed. This model is easy to implement and two test cases have been performed to demonstrate its capabilities.

Chapter 8

Viscoelasticity

All models so far have been concerned with Newtonian fluids, that is purely viscous fluids which have a simple micro-structure and thus can be characterised by the Navier-Stokes equation (5.53). Fluids with complex microstructures exhibit more complicated behaviour which the Navier-Stokes equations fail to capture. Such non-Newtonian fluids may have complex constitutive relations for stress and in this chapter we focus on models for viscoelasticity.

8.1 Rheology and Constitutive Equations

Rheology is defined as the the science of deformation and flow. The classical extremes of a materials behaviour are Hooke's law of elastic solids and Newton's law of viscous fluids. Hooke proposed that the stress, σ, in an elastic body is proportional to the strain, γ:

$$\sigma = G_R \gamma, \tag{8.1}$$

where G_R is referred to as the rigidity modulus. Newton postulated that the stress in a liquid is proportional to the rate of strain, $\dot{\gamma}$:

$$\sigma = \eta \dot{\gamma}, \tag{8.2}$$

where the constant of proportionality, η, is called the viscosity and $\dot{\gamma} = \partial_t \gamma$.

Many materials do not fall neatly into either of these two categories but instead show solid-like or fluid-like behaviour at different timescales or in different circumstances. For example, glass is generally thought of as solid but over sufficiently long times is observed to flow under the force of gravity. The two most important properties in material classification are the viscosity and timescale. Some rheological phenomena include: shear-rate dependent viscosity; non-zero normal stress difference; Weissenburg rod-climbing effect and die swell. A detailed discussion of such behaviour can be found in Barnes et al. [2] and Tanner [64].

8.1.1 Linear Viscoelasticity

For an incompressible fluid in a bounded domain D of $\mathbb{R}^3$ there exists a symmetric stress tensor, $\boldsymbol{\sigma}$, so that from the conservation of momentum:

$$\rho \frac{D\mathbf{u}}{Dt} = \nabla \cdot \boldsymbol{\sigma}, \tag{8.3}$$

and we have assumed there is no body force. A proof of the above can be found in Phillips and Owens [48]. The stress $\boldsymbol{\sigma}$ can be decomposed to

$$\sigma_{\alpha\beta} = -P\delta_{\alpha\beta} + T_{\alpha\beta}, \tag{8.4}$$

where P is the pressure and $\mathbf{T}$ is referred to as the extra stress tensor. The constitutive relation for the extra stress tensor for a Newtonian fluid is given by equations (7.17) and (7.18). An equation for the stress in a purely elastic body can also be derived but here we concentrate on linear viscoelastic behaviour.

Many features of linear viscoelasticity can be deduced from small amplitude oscillatory shear motion. The stress can be shown to be [64]:

$$T_{\alpha\beta}(t) = \int_{-\infty}^{t} G(t-t') A^{(1)}_{\alpha\beta}(t') dt', \tag{8.5}$$

where $A^{(1)}_{\alpha\beta}$ is the first Rivlin-Ericksen tensor which can be interpreted as the

rate of strain. In what follows the tensor quantities defined above are written without Cartesian subscripts to denote one-dimensional shearing motions.

Let

$$\gamma(t) = \gamma_0 \exp(i\omega t), \tag{8.6}$$

where $i = \sqrt{-1}$, ω is the frequency and γ_0 is the strain amplitude, which is assumed to be small. Then

$$\dot{\gamma} = i\omega\gamma_0 \exp(i\omega t), \tag{8.7}$$

and substituting this into (8.5) yields:

$$T = i\omega\gamma_0 e^{-i\omega t} \int_{-\infty}^{t} G(t-t')e^{i\omega t'} dt'. \tag{8.8}$$

Defining the complex modulus $G^\star$ as T/γ gives

$$G^\star = i\omega \int_0^\infty G(s)e^{-i\omega s} ds, \tag{8.9}$$

where $s = t - t'$. Equation (8.9) can be separated into real and imaginary components:

$$G^\star = G' + iG'' = \int_0^\infty \omega G(s)\sin(\omega s)ds + i\int_0^\infty \omega G(s)\cos(\omega s)ds, \tag{8.10}$$

where G' and G'' are called the storage modulus and loss modulus, respectively. The complex viscosity, $\eta^\star$, is defined to be $T/\dot{\gamma}$, hence

$$\eta^\star = \eta' - i\eta'' = \frac{G''}{\omega} - i\frac{G'}{\omega}. \tag{8.11}$$

The detailed form of $\eta^\star$ depends on the constitutive relation for stress. Two important models are the Maxwell and Jeffreys models which are given by the following equations, respectively:

$$T + \tau_1\dot{T} = \eta\dot{\gamma}, \tag{8.12}$$

$$T + \tau_1\dot{T} = \eta(\dot{\gamma} + \tau_2\ddot{\gamma}), \tag{8.13}$$

where τ_1 is a relaxation time and τ_2 is retardation time. Details of the derivation of these equations can be found in Barnes et al. [2] and Phan-Thien [47]. For the Jeffreys model (8.13) the components of the complex shear viscosity are found to be

$$\eta' = \eta_\infty + \frac{\eta_0 - \eta_\infty}{1 + (\omega\tau)^2}, \tag{8.14}$$

$$\eta'' = \frac{(\eta_0 - \eta_\infty)\omega\tau}{1 + (\omega\tau)^2}, \tag{8.15}$$

where η_0 and $\eta_\infty > 0$ are the zero and infinite frequency viscosities, respectively [64], and τ is a relaxation time. The special case $\eta_\infty = 0$ gives the Maxwell model.

When extending equations such as (8.12) and (8.13) to more than one dimension one must consider the principles which govern formulation of constitutive equations. These are: coordinate invariance, determinism and local action; and the principle of material objectivity. Details of these general rules can be found in the books of Phan-Thien [47] but here we merely state that extending equation (8.12) to higher dimensions gives, using contravariant tensors, the Upper Convected Maxwell (UCM) model for stress:

$$\mathbf{T} + \tau_1 \overset{\nabla}{\mathbf{T}} = \eta\dot{\boldsymbol{\gamma}} \tag{8.16}$$

where $\dot{\boldsymbol{\gamma}}$ is defined by equation (7.18) and $\overset{\nabla}{\mathbf{T}}$ denotes the upper convected derivative of $\mathbf{T}$:

$$\overset{\nabla}{\mathbf{T}} = \frac{D\mathbf{T}}{Dt} - (\nabla\mathbf{u})\mathbf{T} - \mathbf{T}(\nabla\mathbf{u})^\dagger, \tag{8.17}$$

and $\dagger$ denotes the matrix transpose.

8.1.2 The Fokker-Planck Equation

Viscoelastic phenomena are primarily due to molecular forces which arise from the orientation of polymer chains in the liquid. The polymers immersed in a solvent can be modeled as elastic dumbbells consisting of two beads and an interconnecting spring. Suppose that the beads have mass m_1 and m_2

and position vectors $\mathbf{x}_1$ and $\mathbf{x}_2$. The equations of motion for the beads can be written as [48]:

$$m_i \frac{d^2\mathbf{x}_i}{dt^2} = -\xi_i \left(\frac{d\mathbf{x}_i}{dt} - (\mathbf{u}_0 + (\nabla \mathbf{u})^\dagger \mathbf{x}_i) \right) + \mathbf{B}_i + \mathbf{F}_i, \quad i = 1, 2, \tag{8.18}$$

where $\mathbf{B}_i$ are the Brownian forces due to the impact on the beads of the solvent molecules, $\mathbf{F}_i$ are the forces on the beads exerted by the spring and ξ_i are the friction coefficients. Let $\mathbf{Q} = \mathbf{x}_2 - \mathbf{x}_1$ be the end-to-end vector of a dumbbell and suppose $\psi(\mathbf{Q}, t)d\mathbf{Q}$ is the probability a dumbbell in the range $\mathbf{Q}$ to $\mathbf{Q} + d\mathbf{Q}$ at time t has end-to-end vector $\mathbf{Q}$. It can be shown [48] that ψ satisfies the Smoluchowski equation:

$$\frac{\partial \psi}{\partial t} + \frac{\partial}{\partial \mathbf{Q}} \cdot \left[(\nabla \mathbf{u})^\dagger \mathbf{Q} \psi - k\xi_{12} \frac{\partial \psi}{\partial \mathbf{Q}} - \psi \xi_{12} \mathbf{F} \right] = 0, \tag{8.19}$$

where $\xi_{12} = 1/\xi_1 + 1/\xi_2$, k is a constant and $\mathbf{F} = \mathbf{F}_1 = -\mathbf{F}_2$. Since

$$\frac{\partial}{\partial \mathbf{Q}} \cdot ((\nabla \mathbf{u})^\dagger \mathbf{Q} \psi) = ((\nabla \mathbf{u})^\dagger \mathbf{Q}) \cdot \frac{\partial \psi}{\partial \mathbf{Q}}, \tag{8.20}$$

the diffusion equation for the probability density function, ψ, known as the Fokker-Planck equation, is:

$$\frac{\partial \psi}{\partial t} + ((\nabla \mathbf{u})^\dagger \mathbf{Q}) \cdot \frac{\partial \psi}{\partial \mathbf{Q}} - k\xi_{12} \frac{\partial^2 \psi}{\partial \mathbf{Q}^2} - \xi_{12} \frac{\partial}{\partial \mathbf{Q}} \cdot (\psi \mathbf{F}). \tag{8.21}$$

Multiplying equation (8.21) by $\mathbf{QQ}$ and integrating over $\mathbb{R}^3$ yields:

$$\langle \overset{\nabla}{\mathbf{QQ}} \rangle = 2k\xi_{12}\mathbf{I} - 2\xi_{12}\langle \mathbf{QF} \rangle, \tag{8.22}$$

where

$$\langle f(\mathbf{Q}) \rangle = \int_{\mathbb{R}^3} f(\mathbf{Q}) \psi(\mathbf{Q}, t) d\mathbf{Q}, \tag{8.23}$$

is the ensemble average of any function f of $\mathbf{Q}$ and we have used the divergence theorem and the fact that $\psi \to 0$ as $|\mathbf{Q}|$ tends to its maximum possible length.

The Kramers expression for the extra stress tells us that

$$\mathbf{T} = -nk\mathbf{I} + \eta_s\dot{\boldsymbol{\gamma}} + n\langle\mathbf{QF}\rangle, \tag{8.24}$$

where n is the number density of the dumbbells. Substituting equation (8.22) into the above for $\langle\mathbf{QF}\rangle$ yields the Giesekus expression for the extra stress tensor:

$$\mathbf{T} = \eta_s\dot{\boldsymbol{\gamma}} - \frac{n}{2\xi_{12}}\langle\overset{\nabla}{\mathbf{Q}}\mathbf{Q}\rangle. \tag{8.25}$$

If the connecting spring is Hookean the force law for $\mathbf{F}$ is

$$\mathbf{F} = H\mathbf{Q}, \tag{8.26}$$

for some positive parameter H, and equation (8.24) becomes

$$\mathbf{T} = -nk\mathbf{I} + \eta_s\dot{\boldsymbol{\gamma}}nH\langle\mathbf{QQ}\rangle. \tag{8.27}$$

Using the fact that

$$\overset{\nabla}{\mathbf{I}} = -\dot{\boldsymbol{\gamma}}, \tag{8.28}$$

we can eliminate $\langle\mathbf{QQ}\rangle$ between equations (8.27) and (8.25) by taking the upper convected derivative of (8.24) to give:

$$\mathbf{T} + \tau_1\overset{\nabla}{\mathbf{T}} = \eta_1\left(\dot{\boldsymbol{\gamma}} + \tau_2\overset{\nabla}{\dot{\boldsymbol{\gamma}}}\right), \tag{8.29}$$

where

$$\begin{aligned}
\eta_1 &= \eta_s + \eta_p, \\
\eta_p &= \frac{nk}{2H\xi_{12}}, \\
\tau_1 &= \frac{1}{2H\xi_{12}}, \\
\tau_2 &= \frac{\eta_s\tau_1}{\eta_1}.
\end{aligned}$$

Equation (8.29) is the Oldroyd B constitutive equation. The solvent and

polymeric contributions to the stress can be separated as

$$\mathbf{T} = \eta_s \dot{\boldsymbol{\gamma}} + \mathbf{s}, \tag{8.30}$$

where $\mathbf{s}$ is the elastic stress, and substituting into (8.29) yields the UCM equation for the extra stress $\mathbf{T}$ as $\eta_s \to 0$:

$$\mathbf{s} + \tau_1 \overset{\nabla}{\mathbf{s}} = \eta_p \dot{\boldsymbol{\gamma}}. \tag{8.31}$$

8.2 Viscoelastic Lattice Boltzmann Models

The equations governing the flow of viscoelastic fluids are, in general, a set of complicated nonlinear partial differential equations of mixed type. For example, if the the fluid is incompressible one must solve the system of equations:

$$\nabla \cdot \mathbf{u} = 0, \tag{8.32}$$

$$\rho \frac{D\mathbf{u}}{Dt} = \nabla \cdot \boldsymbol{\sigma}, \tag{8.33}$$

where $\boldsymbol{\sigma}$ is given by equation (8.4) and the extra stress tensor, $\mathbf{T}$, is given by an appropriate constitutive equation, such as (8.16). Analytical solutions to such equations are limited to a number of special cases (such as the so-called viscometric flows), and experiments on industrial fluids that may be described mathematically by the above equations are often expensive and time-consuming. Therefore, accurate and efficient numerical algorithms for solving non-Newtonian flow problems are considered highly desirable by rheologists. A detailed description of computational rheology is given in [48].

Traditional approaches to the numerical simulation of complex fluids involve the discretisation of the (macroscopic) governing partial differential equations using either finite difference, finite volume or finite element methods (which are local methods) or spectral elements (a global method). Despite their successes there are a number of difficulties associated with these methods. For example, irregular geometries are not easily incorporated into

the discretisation framework (particularly using finite difference approximations), unresolved theoretical problems concerning compatibility conditions to ensure a well-posed discrete problem, and difficulties in dealing with the convective term, $\mathbf{u} \cdot \nabla \mathbf{T}$.

The macroscopic models for viscoelasticity do not always give results that are in quantitative agreement with experimental data. Therefore, it is necessary to look to more sophisticated models based on a finer level of description, such as the Fokker-Planck equation in Section 8.1.2. Numerical methods for solving these equations generally involve a computationally intensive procedure and only in recent years has this become a feasible task. Since the lattice Boltzmann algorithm is based on discrete mesoscopic dynamics and has the computational advantages of: natural parallelisation; and suitability for flows in complex geometries (c.f. Section 5.5), it is considered a promising computational tool for viscoelastic flows.

8.2.1 A LBE for the Jeffreys Model

The first attempt to extend the lattice Boltzmann equation to represent viscoelastic effects was by Giraud et al. [13] who incorporated Jeffreys' complex shear viscosity (8.13) into the original LBE framework. They considered the linearised LBE with a full collision matrix, i.e.

$$N_i(\mathbf{x} + \mathbf{c}_i, t + 1) = N_i(\mathbf{x}, t) - \sum_i \Omega_{ij}(N_j - N_j^{(e)}), \tag{8.34}$$

and first defined the model on a thirteen velocity (D2Q13) lattice, as shown in Figure. 8.1. We explained in Section 5.1 that the elements of $\mathbf{\Omega}$ can be chosen arbitrarily, subject to the conservation laws and laws of symmetry. We also remarked in Section 5.4 that the macroscopic equations depend on the eigenvectors of the collision matrix. The normalised eigenvectors of this model were chosen to be

$$
\begin{aligned}
\boldsymbol{\psi}_0 &= (1,1,1,1,1,1,1,1,1,1,1,1,1,1)/\sqrt{13},\\
\boldsymbol{\psi}_1 &= (0,1,0,-1,0,1,-1,-1,1,2,0,-2,0)/\sqrt{14},\\
\boldsymbol{\psi}_2 &= (0,0,1,0,-1,1,1,-1,-1,0,2,0,-2)/\sqrt{14},\\
\boldsymbol{\psi}_3 &= (28,15,15,15,15,2,2,2,2,-24,-24,-24,-24)/2\sqrt{1001},\\
\boldsymbol{\psi}_4 &= (0,1,-1,1,-1,0,0,0,0,4,-4,4,-4)/2\sqrt{17},\\
\boldsymbol{\psi}_5 &= (0,0,0,0,0,1,-1,1,-1,0,0,0,0)/2,\\
\boldsymbol{\psi}_6 &= (4,-2,-2,-2,-2,1,1,1,1,0,0,0,0)/6,\\
\boldsymbol{\psi}_7 &= (28,4,4,4,4,-20,-20,-20,-20,9,9,9,9)/6\sqrt{77},\\
\boldsymbol{\psi}_8 &= (0,-2,0,2,0,1,-1,-1,1,0,0,0,0)/2\sqrt{3},\\
\boldsymbol{\psi}_9 &= (0,0,-2,0,2,1,1,-1,-1,0,0,0,0)/2\sqrt{3},\\
\boldsymbol{\psi}_{10} &= (0,-2,0,2,0,-2,2,2,-2,3,0,-3,0)/\sqrt{42},\\
\boldsymbol{\psi}_{11} &= (0,0,-2,0,2,-2,-2,2,2,0,3,0,-3)/\sqrt{42},\\
\boldsymbol{\psi}_{12} &= (0,-4,4,-4,4,0,0,0,0,1,-1,1,-1)/2\sqrt{17},
\end{aligned}
$$

corresponding to the eigenvalues

$$[0,0,0,\lambda_e,\lambda_\nu,\lambda'_\nu,\lambda_S,\lambda_S,\lambda_\chi,\lambda_\chi,\lambda'_\chi,\lambda'_\chi,\lambda_z]. \tag{8.35}$$

In Section 5.4 we showed how the LBE can be expressed in an alternative dual basis based on the moments $m_i = \mathbf{c}_i \cdot \boldsymbol{\psi}$. The macroscopic equations for this model were derived via the Chapman-Enskog analysis in this new basis and the expansion yields:

$$\partial_{t_1}\mathbf{m}^{(0)} + \hat{S}_\alpha \partial_\alpha \mathbf{m}^{(0)} = -\hat{\boldsymbol{\Omega}}\mathbf{m}^{(0)}, \tag{8.36}$$

$$\partial_{t_2}\mathbf{m}^{(0)} + \left(\mathbf{I} - \frac{\hat{\boldsymbol{\Omega}}}{2}\right)\partial_{t_1}\mathbf{m}^{(1)} + \hat{S}_\alpha\left(\mathbf{I} - \frac{\hat{\boldsymbol{\Omega}}}{2}\right)\partial_\alpha \mathbf{m}^{(1)} = -\hat{\boldsymbol{\Omega}}\mathbf{m}^{(2)}, \tag{8.37}$$

where $(\hat{S}_\alpha)_{ij} = \delta_{ij}c_{i\alpha}$. From the above expansion, Giraud et al. [13] were able to recover isotropic Navier-Stokes equations.

To incorporate viscoelastic effects into the model the authors coupled the

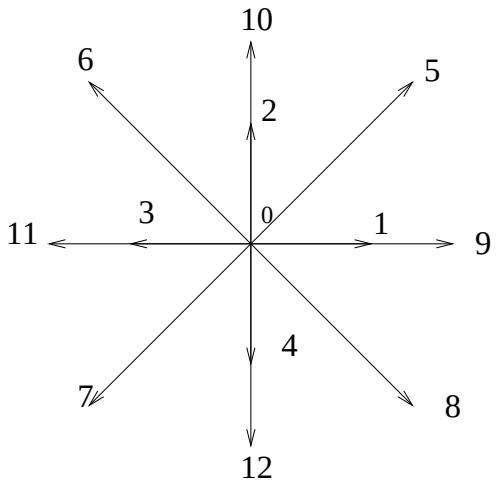

Figure 8.1: The D2Q13 lattice.

symmetric viscous stress tensor (which is related to the moments m_4 and m_5) to some new quantity which evolves slowly in time, leading to memory effects. To achieve this they added two non-propagating quantities that behave like the viscous stress tensor. The new model is a 15 velocity model with $\boldsymbol{\psi}_4$ and $\boldsymbol{\psi}_5$ replaced by

$$\boldsymbol{\psi}_4 = (a, 0, 0, 1, -1, 1, -1, 0, 0, 0, 0, 4, -4, 4, -4), \tag{8.38}$$

$$\boldsymbol{\psi}_5 = (0, b, 0, 0, 0, 0, 0, 1, -1, 1, -1, 0, 0, 0, 0), \tag{8.39}$$

where a and b are coupling constants, and two new eigenvectors

$$\boldsymbol{\psi}_{13} = (-68/a, 0, 0, 1, -1, 1, -1, 0, 0, 0, 0, 4, -4, 4, -4), \tag{8.40}$$

$$\boldsymbol{\psi}_{14} = (0, -4/b, 0, 0, 0, 0, 0, 1, -1, 1, -1, 0, 0, 0, 0), \tag{8.41}$$

which have not been normalised for legibility. The corresponding eigenvalues are denoted by $[\lambda_\gamma, \lambda_\gamma]$ and the additional lattice velocities $\mathbf{c}_{13}$ and $\mathbf{c}_{14}$ are in the rest particle position. The other 11 eigenvectors are derived from the vectors $\boldsymbol{\psi}_0$ to $\boldsymbol{\psi}_3$ and $\boldsymbol{\psi}_6$ to $\boldsymbol{\psi}_{12}$ with two components equal to zero in front of them.

When $\lambda_\gamma = 0$, the moments m_{13} and m_{14} are conserved and the following

macroscopic equations are obtained:

$$\partial_t \rho + \partial_x j_x + \partial_y j_y = 0, \tag{8.42}$$

$$\begin{aligned}\partial_t j_x + \left(\partial_x \tfrac{j_x^2}{\rho} + \partial_y \tfrac{j_x j_y}{\rho}\right) + \partial_x P + \tfrac{c_\perp}{\kappa}(\partial_x m_{13} + \partial_y m_{14}) \\ = \nu_\infty \triangle j_x + \xi_\infty \partial_x(\partial_x j_x + \partial_y j_y),\end{aligned} \tag{8.43}$$

$$\begin{aligned}\partial_t j_y + \left(\partial_y \tfrac{j_y^2}{\rho} + \partial_x \tfrac{j_x j_y}{\rho}\right) + \partial_y P + \tfrac{c_\perp}{\kappa}(\partial_x m_{14} - \partial_y m_{13}) \\ = \nu_\infty \triangle j_y + \xi_\infty \partial_y(\partial_x j_x + \partial_y j_y),\end{aligned} \tag{8.44}$$

$$\partial_t m_{13} + \kappa(\partial_x j_x - \partial_y j_y) = D_\infty \triangle m_{13}, \tag{8.45}$$

$$\partial_t m_{14} + \kappa(\partial_x j_y + \partial_y j_x) = D_\infty \triangle m_{14}, \tag{8.46}$$

where $\mathbf{j}$ is the momentum, and κ and $c_\perp$ are free parameters such that $0 < \kappa < 749/442$ and $c_\perp^2 < \kappa/2 < 749/884$. The viscosities and pressure are given by:

$$\nu_\infty = \left(\frac{\kappa}{2} - c_\perp^2\right)\left(\frac{1}{\lambda_\nu} - \frac{1}{2}\right), \tag{8.47}$$

$$\xi_\infty = \left(\frac{3\kappa}{2} - c_s^2\right)\left(\frac{1}{\lambda_e} - \frac{1}{2}\right), \tag{8.48}$$

$$D_\infty = c_\perp^2 \frac{845 - 1383\kappa + 442\kappa^2}{\kappa(749 - 442\kappa)}\left(\frac{1}{\lambda_\xi} - \frac{1}{2}\right), \tag{8.49}$$

$$P = c_s^2 \rho, \tag{8.50}$$

where the sound speed, c_s, is considered a free parameter.

When λ_γ is non-zero, m_{13} and m_{14} are no longer conserved quantities and must have equilibrium values. For simplicity, both these values are set to zero in [13]. If λ_γ is of the same order of magnitude as the other eigenvalues the Navier-Stokes equations can be derived from the Chapman-Enskog analysis with a shear viscosity

$$\nu_0 = \left(\frac{\kappa}{2} - c_\perp^2\right)\left(\frac{1}{\lambda_\nu} - \frac{1}{2}\right) + c_\perp^2\left(\frac{1}{\lambda_\gamma} - \frac{1}{2}\right). \tag{8.51}$$

When λ_γ is a non-zero but very small the fluid should behave as a viscous one for time scales much longer than $1/\lambda_\gamma$ and as an elastic one for time

scales much shorter. To study this, Giraud et al [13] examined the roots of the dispersion equation (5.84), which were obtained numerically. We note briefly that no analytical expressions for the determinant were given and the model is not generalised in the sense of Section 5.4. The authors plot the real and imaginary parts of the roots, z, of the dispersion equation and observe three distinct regimes: three hydrodynamic modes with $z \to 1$ as $k \to 0$; two "quasi-hydrodynamic" modes with $z \sim 1$ when $k \to 0$; and the non-hydrodynamic ones with $|z| < 1$ when $k \to 0$. A coupling between a hydrodynamic (shear) mode and one of the quasi-hydrodynamic modes for $k > kc \sim \lambda_\gamma/(2c_\perp)$ was observed; a signature of a Jeffreys/Maxwell complex viscosity.

Giraud et al. [13] appear to have built the first viscoelastic LBE and their model was able to demonstrate some non-Newtonian behaviour. Although most encouraging, the results are only qualitative and the amount of numerical evidence presented for viscoelasticity is small. Also, the authors were not able to derive the macroscopic equations of motion since the Chapman-Enskog analysis assumes the time scales are much larger than the inverse of the smallest non-zero eigenvalue, which is not necessarily true in this case. Moreover, the (linear) dispersion approach is not valid for the convected Jeffreys, or Oldroyd B equation (8.29), since this model contains nonlinear terms in velocity gradients.

This model was improved by the same authors [14] by reducing the lattice to a D2Q11 model, shown in Figure 8.2. As well as simplifying the model they also argued that the collision matrix, $\mathbf{\Omega}$, can be perturbed in the same manner as the distribution functions in the Chapman-Enskog analysis, i.e:

$$\mathbf{\Omega} = \mathbf{\Omega}^{(0)} + \epsilon\mathbf{\Omega}^{(1)} + \epsilon^2\mathbf{\Omega}^{(2)}, \tag{8.52}$$

where the matrices are assumed to have the same eigenvectors which are split into three groups: the conserved ones with zero eigenvalues; the quasi-conserved ones with zero eigenvalues for the zeroth order matrix; and the non-conserved ones with zero eigenvalues only for the first and second order

matrices. These eigenvectors are similar to the 15 velocity model:

$$
\begin{aligned}
\boldsymbol{\psi}_0 &= (1,1,1,1,1,1,1,1,1,0,0),\\
\boldsymbol{\psi}_1 &= (0,1,0,-1,0,1,-1,-1,1,0,0),\\
\boldsymbol{\psi}_2 &= (0,0,1,0,-1,1,1,-1,-1,0,0),\\
\boldsymbol{\psi}_3 &= (4,1,1,1,1,-2,-2,-2,-2,0,0),\\
\boldsymbol{\psi}_4 &= (0,1,-1,1,-1,0,0,0,0,0,0),\\
\boldsymbol{\psi}_5 &= (0,0,0,0,0,1,-1,1,-1,0,0),\\
\boldsymbol{\psi}_6 &= (4,-2,-2,-2,-2,1,1,1,1,0,0),\\
\boldsymbol{\psi}_7 &= (0,4,0,-4,0,-2,2,2,-2,0,0),\\
\boldsymbol{\psi}_8 &= (0,0,4,0,-4,-2,-2,2,2,0,0),\\
\boldsymbol{\psi}_9 &= (0,2,-2,2,-2,0,0,0,0,-4/a,0)\\
\boldsymbol{\psi}_{10} &= (0,0,0,0,0,2,-2,2,-2,0,-4/b),
\end{aligned}
$$

which have not been normalised. The obtained macroscopic equations for viscoelasticity are then:

$$\partial_t\rho + \partial_x j_x + \partial_y j_y = 0, \tag{8.53}$$

$$
\begin{aligned}
&\partial_t j_x + \partial_x P + c_\perp \left(1-\tfrac{\lambda_\gamma}{2}\right)(\partial_x m_9 + \partial_y m_{10})\\
&\quad = \nu_\infty \triangle j_x + \xi_\infty \partial_x(\partial_x j_x + \partial_y j_y),
\end{aligned} \tag{8.54}
$$

$$
\begin{aligned}
&\partial_t j_y + \partial_y P + c_\perp \left(1-\tfrac{\lambda_\gamma}{2}\right)(\partial_x m_{10} - \partial_y m_9)\\
&\quad = \nu_\infty \triangle j_y + \xi_\infty \partial_y(\partial_x j_x + \partial_y j_y),
\end{aligned} \tag{8.55}
$$

$$\left(1-\tfrac{\lambda_\gamma}{2}\right)\partial_t m_9 + \lambda_\gamma m_{10} + \partial_x j_x - \partial_y j_y = D_\infty \triangle m_9, \tag{8.56}$$

$$\left(1-\tfrac{\lambda_\gamma}{2}\right)\partial_t m_{10} + \lambda_\gamma m_9 + \partial_x j_y + \partial_y j_x = D_\infty \triangle m_{10}, \tag{8.57}$$

where the transport coefficients now read:

$$\nu_\infty = \frac{1-4c_\perp^2}{4}\left(\frac{1}{\lambda_\nu}-\frac{1}{2}\right), \tag{8.58}$$

$$\xi_\infty = \left(\frac{3}{4}-c_s^2\right)\left(\frac{1}{\lambda_e}-\frac{1}{2}\right), \tag{8.59}$$

$$D_\infty = c_\perp^2\left(\frac{1}{\lambda_\xi}-\frac{1}{2}\right). \tag{8.60}$$

The three conservation equations can be written in the equivalent mechanical formulation:

$$\partial_t\rho + \partial_x j_x + \partial_y j_y = 0, \tag{8.61}$$

$$\partial_t j_\alpha = \partial_\beta \sigma_{\alpha\beta}, \tag{8.62}$$

where the stress tensor $\sigma_{\alpha\beta} = -P\delta_{\alpha\beta} + \sigma_{\alpha\beta}^{(v)} + \sigma_{\alpha\beta}^{(N)}$ contains a viscous (v) and non-Newtonian (N) contribution:

$$\sigma_{\alpha\beta}^{(v)} = \nu_\infty(\partial_\alpha j_\beta + \partial_\beta j_\alpha - \partial_\gamma j_\gamma \delta_{\alpha\beta}) + \xi_\infty \partial_\gamma j_\gamma \delta_{\alpha\beta}, \tag{8.63}$$

$$\sigma_{\alpha\beta}^{(N)} = c_\perp\left(1-\frac{\lambda_\gamma}{2}\right)m_{\alpha\beta}, \tag{8.64}$$

where $m_{xx} = m_{yy} = m_9$ and $m_{xy} = m_{yx} = m_{10}$. Equation (8.64) is a solution of

$$\sigma_{\alpha\beta}^{(N)} + \tau(\partial_t \sigma_{\alpha\beta}^{(N)} + D_\infty \triangle \sigma_{\alpha\beta}^{(N)}) = (\nu_0 - \nu_\infty)(\partial_\alpha j_\beta + \partial_\beta j_\alpha - \partial_\gamma j_\gamma \delta_{\alpha\beta}), \tag{8.65}$$

where $\tau = (1/\lambda_\gamma) - 1/2$. Equation (8.65) is claimed to be the Jeffreys constitutive equation, plus a stress diffusion term $D_\infty \triangle \sigma_{\alpha\beta}^{(N)}$, which becomes negligible when $D_\infty \tau \sim 1$.

To verify the model Giraud et al. [14] simulated a pulsed Couette flow between two parallel plates, where the plate at height $h = 0$ oscillates in time with pulsation ω. The vertical boundaries were periodic while the plate at $h = H$ was assigned the bounce-back condition. Their results for the amplitude of the flow velocity are in excellent agreement with theoretical

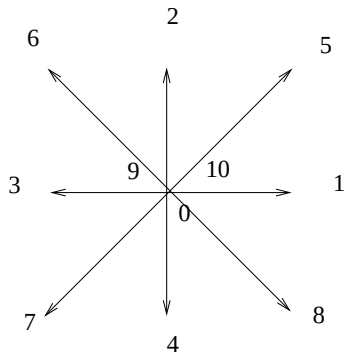

Figure 8.2: The D2Q11 lattice.

predictions but errors in the second harmonic are observed. Although the authors are not able to explain this discrepancy they do offer some potential causes. They suggest it may be due to the approximations used to compute the theoretical results (details of which are not given in [14]) and/or to a small error in the localisation of the effective walls associated with the bounce-back scheme.

As with the original model [13] there is little numerical verification for the viscoelastic LBE described above. Moreover, the constitutive equation (8.65) does not contain any time derivatives on the right-hand side which should be present in a Jeffreys model (8.13). Another limitation is equation (8.65), despite being given in tensor notation, does not satisfy the principles of objectivity of continuum mechanics (cf. [47] for a review of this subject and the references therein) and thus is not frame invariant and may only be valid for simple shear flows (with $\alpha = x$ and $\beta = y$ in (8.65)). A satisfactory dimensional extension of (8.13) is the upper-convected Jeffreys model, also known as the Oldroyd B model (8.29), which this lattice Boltzmann model cannot recover in the macroscopic limit.

8.2.2 A LBE for the Maxwell Model

A Maxwell model for viscoelastic media links the elastic part of the stress tensor, $\Pi^{(el)}_{\alpha\beta}$, to the rate of strain $\dot{\gamma}_{\alpha\beta} = \partial_\alpha u_\beta + \partial_\beta u_\alpha$ via the equation

$$\lambda \partial_t \Pi^{(el)}_{\alpha\beta} = -\Pi^{(el)}_{\alpha\beta} + \mu \dot{\gamma}_{\alpha\beta} \tag{8.66}$$

where μ is an elastic coefficient and λ is a relaxation time. Then the viscoelasticity of the fluid can be taken into account by adding the Maxwell body force $\mathbf{F}^{(el)}$ to the right hand side of the Navier-Stokes momentum equation (5.53):

$$\mathbf{F}^{(el)}(\mathbf{x}, \tau) = \frac{\mu}{\lambda} \int_{-\infty}^{\tau} \exp\left[-(\tau - \tau')/\lambda\right] \Delta\mathbf{u}(\mathbf{x}, \tau') d\tau'. \tag{8.67}$$

Grant et al. [27] proposed adding the lattice equivalent of (8.67) to the lattice BGK equation (5.12):

$$N_i(\mathbf{x} + \mathbf{c}_i, t+1) = N_i(\mathbf{x}, t) + \omega \left[N_i^{(e)} - N_i(\mathbf{x}, t)\right] + \chi \left(\mathbf{G}(\mathbf{x}, t)\mathbf{c}_i\right), \tag{8.68}$$

where χ is a constant depending on the lattice and $\mathbf{G}$ is the time discretisation form of (8.67), i.e.

$$\mathbf{G}(\mathbf{x}, t+1) = \mathbf{G}(\mathbf{x}, t) \left[1 - \frac{1}{\lambda}\right] + \frac{\mu}{\lambda} \Delta\mathbf{u}(\mathbf{x}, t). \tag{8.69}$$

Here, Δ is the discrete Laplace operator

$$\Delta(\mathbf{x}, t) = \zeta \sum_i \left[\mathbf{u}(\mathbf{x} + \mathbf{c}_i, t) - \mathbf{u}(\mathbf{x}, t)\right], \tag{8.70}$$

and ζ is a lattice constant.

This model has been checked for viscoelastic properties on the hexagonal FHP lattice (so that $\chi = 1/3$ and $\zeta = 2/3$) by measuring the Fourier transform of the transverse velocity auto-correlation function $|\tilde{u_y}(k_x, \theta)|^2$,

where [27]

$$\tilde{u_y}(k_x,\theta) = \frac{1}{H^2T}\sum_{x=-H/2}^{H/2}\sum_{y=1}^{H}\sum_{t=1}^{T} u_y(x,y,t)e^{-jk_x x}e^{j\theta t}, \tag{8.71}$$

with $j=\sqrt{-1}$, T being the maximum number of time steps, H a height and

$$k_x = 2\pi n/H, \quad \text{for } n=-H/2,\cdots,H/2, \tag{8.72}$$

$$\theta = 2\pi m/T, \quad \text{for } m=1,\cdots,T. \tag{8.73}$$

The initial results generated by Grant et al. [27] predict two propagating shear waves, showing that their model does indeed exhibit viscoelastic properties. The simulations were only qualitative in nature however and dispersion relations needed to be derived in order to get a more quantitative insight of the model's elastic features. To achieve this, Grant et al. [27] derived dispersion relations for the continuous shear waves in the framework of the Maxwell model, i.e.

$$\partial_t V = \nu\triangle V + \mu\int_{-\infty}^{t}\exp[-(t-t')/\tau]\triangle V(t')\frac{dt'}{\tau}, \tag{8.74}$$

where

$$V(x,t) = V_0\exp(-j\omega t)\exp(jkx), \tag{8.75}$$

and from this they obtain the following equation for k:

$$k^2 = \theta\frac{j+\theta t}{\nu(1-j\theta t)+\mu}. \tag{8.76}$$

The authors were interested in propagating shear waves with sufficiently small dissipation, hence they considered parameters for which the ratio $\Im(k)/\Re(k)$ is small. Grant et al. [27] chose to simulate a periodic volume-driven fluid in a capillary and the obtained results are in fairly good agreement with the theoretical values. They conclude that their model reproduces the Maxwell viscoelasticity for incompressible fluid flow. However, they have only run

simulations over a small range of parameters. This approach has therefore only been shown to be successful in a small number of specific cases. Stability requirements have prohibited simulations in the limit of small relaxation times and it has yet to be shown if a similar method can be applied to more sophisticated viscoelastic models. Also, the extra terms needed for the elastic contribution have been added to the right-hand side of familiar LBGK equation (5.12), which was 'tuned' specifically for Newtonian flows, without considering how they effect the macroscopic equations. No effort has been made to check if the correct equations of motion are recovered in the macroscopic limit. It is also worth mentioning that a one-parameter LBGK equation may not be a suitable model for viscoelasticity since it assumes that all modes relax to their equilibrium state at the same rate; which may be physically unrealistic (see Section 8.2.1).

8.2.3 Lattice Fokker-Planck Equation

It has been shown by Luo [38] that the lattice Boltzmann equation can be derived from a direct numerical discretisation of the continuous Boltzmann equation (1.16). A lattice Boltzmann-type equation for the Fokker-Planck equation seems to have been derived independently by Succi et al. [62] and Onishi et al. [45] who used the ideas of Luo to discretise the Fokker-Planck equation on a lattice.

Succi et al. [62] considered the Fokker-Planck equation (8.21) in a concise, one-dimensional form:

$$\partial_t f + v\partial_x f = C = \partial_v[R(v) + D\partial_v f], \tag{8.77}$$

where f is the one-body particle distribution function and C is the rate of change due to collisions, which consists of a drag term R and a diffusion coefficient D. Succi et al. [62] begin in the same fashion of Luo [38] by projecting the distribution function upon a Hermite basis set:

$$f = \sum_{k=0}^{M} F_k(x,t)w(v)h_k(v), \tag{8.78}$$

where

$$w(v) = (2\pi)^{-1/2} e^{-v^2/2}, \tag{8.79}$$

is the Gaussian weight of the discrete Hermite polynomials $h_k(v)$. Equation (8.77) can now be written as the following system of PDEs:

$$\partial_t F_k + \partial_x \Phi_k = C_k, \quad k = 0, 1, \ldots, M, \tag{8.80}$$

where

$$F_k = \langle f, h_k \rangle, \tag{8.81}$$

$$\Phi_k = \langle vf, h_k \rangle, \tag{8.82}$$

$$C_k = \langle C, h_k \rangle, \tag{8.83}$$

are the generalised densities, fluxes and collision rates, respectively, and

$$\langle f, g \rangle = \int w(v) f(v) g(v) dv, \tag{8.84}$$

is the scalar product in Hilbert space. These scalar products are evaluated by means of a Hermite-Gauss quadrature to yield:

$$F_k = \sum_{i=0}^{G} h_{ki} f_i, \tag{8.85}$$

$$\Phi_k = \sum_{i=0}^{G} h_{ki} v_i f_i, \tag{8.86}$$

$$C_k = \sum_{i=0}^{G} c_i, \tag{8.87}$$

where v_i are a set of $G+1$ Gaussian nodes, w_l are the corresponding weights, and

$$f_i = \frac{f w_i}{w(v_i)}, \tag{8.88}$$

$$c_i = \frac{C w_i}{w(v_i)}. \tag{8.89}$$

After a little algebra and using a first-order Euler scheme for the time discretisation, Succi et al. [62] obtained:

$$f_i(x + c_i, t + 1) - f_i(x, t) = c_i(x, t), \tag{8.90}$$

which is the desired lattice Fokker-Planck equation. The specific form of the collision term, c_i, is needed to make equation (8.90) operational, and this can be obtained once the moments C_k are computed from $C_k = \langle h_k \partial_v [R(v)f + D\partial_v f] \rangle$. The form of R and D depends on the problem of interest.

To relate equation (8.90) to the lattice Boltzmann equation, Succi et al. [62] write the function C_k as the result of an operator $\hat{C}$ acting upon f:

$$C_k = \langle h_k, \hat{C} f \rangle = \sum_m C_{km} F_m, \tag{8.91}$$

where the coefficients

$$C_{km} = \langle h_k, \hat{C} w(v) h_m \rangle \tag{8.92}$$

provide the matrix representation of the collision operator $\hat{C}$ in the discrete Hermite basis set [62]. Substituting the above two equations into (8.89) shows, after some algebra

$$c_{ij} = w_i \sum_{k,m} A_{k,i} C_{k,m} A_{m,l}, \tag{8.93}$$

where $A_{m,n} = h_m(v_n)/H_m$ are orthonormal eigenvectors. To ensure Galilean invariance and include hydrodynamic effects, $w(v)$ in equation (8.92) needs to be treated appropriately. Succi et al. [62] consider an expansion about a small mean flow speed, u, and find the following lattice Fokker-Planck equation for hydrodynamics [62]

$$f_i(x + c_i, t + 1) - f_i(x, t) = \sum_j c_{ij} (f_j - f_j^{(e)}), \tag{8.94}$$

where $f_i^{(e)}$ is the local equilibrium function which can be constructed so as to conserve the correct quantities at the hydrodynamic scale.

The authors illustrate their model's capabilities by specifying a form of the lattice Fokker-Planck equation and performing some simple test simulations. They choose a one-dimensional charged fluid such that

$$R(v) = \gamma(v)v - a, \qquad D = \gamma(v)T, \tag{8.95}$$

where $\gamma(v)$ denotes the inverse relaxation time processes describing the dissipative interactions of particles of speed v with particles at rest. For simplicity this term is taken to be $\gamma(v) = \gamma_0 + \gamma_2 v^2$. For the linear case ($\gamma_2 = 0$) the steady flow speed u was measured and shown to agree well with Ohm's law: $u_0 = a/\gamma_0$. In the nonlinear regime, a temperature dependence is introduced and the obtained results are shown to preserve the qualitative features associated with the drift speed. As with the viscoelastic LBE's of Sections 8.2.1 and 8.2.2, the amount of numerical evidence presented is small and limited to qualitative studies. Although the derivation of the lattice Fokker-Planck equation in [62] is general, specific forms of the collision operator could be difficult to obtain, especially if the terms $R(v)$ and D contain derivatives of functions. It should be noted that this algorithm may offer some advantages over other Fokker-Planck solvers since it preserves the desirable feature of the standard lattice Boltzmann equation, i.e. the streaming operator is linear, boundary conditions can be easily implemented, and efficient parallel processing.

In the same year, Onishi et al. [45] proposed a lattice Fokker-Planck equation specifically designed for polymeric liquids, i.e. so that the UCM model can be recovered. Like Succi et al. [62] these authors take advantage of Gauss-Hermite quadrature approximations but start by introducing the distribution function, ψ, for the polymeric Fokker-Planck equation:

$$\psi(\mathbf{Q}) = \phi(\mathbf{Q})e^{-(H/2k)(\mathbf{Q}\cdot\mathbf{Q})}, \tag{8.96}$$

where $\mathbf{Q}$ is a configuration vector, k is a constant, H is the Hookean spring constant, and $\phi(\mathbf{Q})$ is a function. The moments of ψ can be found by evalu-

ating integrals of the form

$$\begin{aligned}\langle B(\mathbf{Q})\rangle &= \int B(\mathbf{Q})\psi(\mathbf{Q})d\mathbf{Q} \\ &= \left(\frac{2k}{H}\right)^{D/2}\int B(Q_c\boldsymbol{\xi})\phi(Q_c\xi)e^{\boldsymbol{\xi}\cdot\boldsymbol{\xi}},\end{aligned} \tag{8.97}$$

where $B(\mathbf{Q})$ is an arbitrary function of $\mathbf{Q}$ and $\boldsymbol{\xi} = \mathbf{Q}/Q_c$ is a non-dimensional configuration vector with $Q_c = \sqrt{2k/H}$, and D is the dimension of space. Applying the Gauss-Hermite Quadrature to equation (8.97) yields:

$$\langle B(\mathbf{Q})\rangle = \sum_{j}^{N} B(\mathbf{Q}_j)\psi_j, \tag{8.98}$$

where

$$\psi_j = w_j\left(\frac{2\pi k}{H}\right)^{D/2}\phi(\mathbf{Q}_j). \tag{8.99}$$

In equation (8.99), w_j are weight factors and $\mathbf{Q}_j$ are the discrete configuration vectors. The Fokker-Planck equation (8.21) can now be written as

$$\partial_t\psi_j = -\mathbf{u}\cdot\nabla\psi + \Omega_{\phi,j} + M_j, \tag{8.100}$$

where $\Omega_{\phi,j}$ describes the dumbbells relaxation to an equilibrium state and M_j accounts for solvent effects. Onishi et al. chose an equilibrium function in the following form:

$$\psi^{(e)} = \left(\frac{H}{2\pi k}\right)^{D/2}\exp\left(-\frac{H}{2k}\mathbf{Q}\cdot\mathbf{Q}\right), \tag{8.101}$$

and substituting equation (8.99) into the above yields:

$$\psi_j^{(e)} = w_j. \tag{8.102}$$

To keep the model simple, a one-parameter collision operator is chosen to

describe the relaxation process

$$\Omega_{\psi,j} = -\frac{1}{\tau_\psi}\left(\psi_j - \psi_j^{(e)}\right), \tag{8.103}$$

where τ_ψ is a relaxation parameter for ψ_j. We note the similarity with the BGK collision operator in the standard lattice Boltzmann equation (5.12).

To find an expression for M_j, equation (8.99) is substituted into the right-hand side of (8.21) to find

$$M_j = \psi_j \frac{H}{k}\left(\mathbf{Q}_j \cdot \mathbf{Q}_j - \frac{k}{H}\mathbf{I}\right) : (\nabla \mathbf{u})^\dagger \cdot \frac{H}{k_B}\langle \mathbf{Q}_j \mathbf{Q}_j \rangle. \tag{8.104}$$

It is readily checked that the moments of M_j are

$$\sum_j M_j = 1, \tag{8.105}$$

$$\sum_j M_j \mathbf{Q}_j = 0, \tag{8.106}$$

$$\sum_j M_j \mathbf{Q}_j \mathbf{Q}_j = (\nabla \mathbf{u})^\dagger \cdot \langle \mathbf{Q}_j \mathbf{Q}_j \rangle + \langle \mathbf{Q}_j \mathbf{Q}_j \rangle \cdot \nabla \mathbf{u}. \tag{8.107}$$

The optimal choice for the space discretisation is a D2Q9 lattice, i.e. the $\mathbf{Q}_j$'s for the lattice shown in Figure 5.1 with weights W_j given by (5.28). The time discretisation is again a first-order Euler scheme and the resulting lattice Fokker-Planck equation for polymeric liquids is

$$\begin{aligned}\psi_j(\mathbf{x}, t+1) - \psi_j(\mathbf{x}, t) = \\ \triangle\psi_j - \frac{1}{\tau_\psi + 0.5}(\psi - \psi^{(e)}) + \frac{\tau_\psi}{\tau_\psi + 0.5} M_j,\end{aligned}$$

where $\triangle\psi_j$ represents convection of dumbbells and is given in [45] by

$$\triangle\psi_j = \sum_k [-\psi_j(\mathbf{c}) Z_k(\mathbf{x}) + \psi_j(\mathbf{x} + \mathbf{c}_k) Z_{-k}(\mathbf{x} + \mathbf{c}_k)]/\bar{N}, \tag{8.108}$$

$$W_k = \frac{N_k}{\sum_i N_i}, \tag{8.109}$$

where $\bar{N}$ is a normalisation factor. The polymeric stress, $\mathbf{T}_p$ is then found from Kramers formula:

$$\mathbf{T}_p = -n_p \sum_j H\mathbf{Q}_j\psi_j + n_p \sum_j H\mathbf{Q}_j\psi_j^{(e)}, \tag{8.110}$$

where n_p is the number density of the dumbbells.

To couple equation (8.110) with the lattice Boltzmann equation (5.12), Onishi et al. [45] introduce a modified particle distribution, $N_i^{(e)}$, function to incorporate the extra stress:

$$N_i^{(e)} = \rho W_i \left[1 + 3\mathbf{c}_i\mathbf{u} - \frac{3}{2}u^2 + \frac{9}{2}\left(\mathbf{c}_i \cdot \mathbf{u}\right)^2\right] + T_i, \tag{8.111}$$

$$T_i = \frac{9}{2}\left(\mathbf{c}_i\mathbf{c}_i - \frac{1}{3}\mathbf{I}\right) : \frac{\mathbf{T}_p}{k}. \tag{8.112}$$

The zeroth and first moments of the equilibrium function give the density and momentum, showing that the additional term T_i does not effect the conservation constraints, but the second moment is

$$\sum_i N_i^{(e)} = \rho\mathbf{u}\mathbf{u} + \rho\mathbf{I} + \mathbf{T}_p. \tag{8.113}$$

The Chapman-Enskog expansion now yields the equations of motion for an Oldroyd B fluid:

$$\partial_t\rho + \nabla \cdot (\rho\mathbf{u}) = 0, \tag{8.114}$$

$$\rho\left(\partial_t\mathbf{u} + \mathbf{u} \cdot \nabla\mathbf{u}\right) = -\nabla P - \nabla \cdot \boldsymbol{\sigma}, \tag{8.115}$$

$$\boldsymbol{\sigma} = \mu_s\dot{\boldsymbol{\gamma}} + \mu_p\mathbf{T}_p, \tag{8.116}$$

where $\mu_s = \rho k\omega$ is the solvent viscosity and $\mu_p = n_p k\tau_\psi$ is the polymeric viscosity.

Onishi et al. [45] calculate shear and first normal stress difference using their proposed model and the results show how they relax to their equilibrium values at a Deborah number, $De = \tau_\psi/\dot{\gamma} = 10$. They also incorporate a FENE-P model for the dumbbells and show shear-thinning characteristics.

Moreover, the results are in good agreement with theoretical predictions for a wide range of De. The authors also investigate the validity of the model by performing simulations of small-amplitude oscillatory shear flows. The temporal evolution of the polymer stress is seen to be in-phase with the shear rate, which agrees qualitatively with the UCM model. When the oscillation has a high frequency and the flow domain is large analytical solutions for the velocity profile can be found, and the numerical results obtained in [45] agree very well with these.

8.3 Concluding Remarks

In this chapter we have discussed the significant models which have been proposed as an extension of the LBE to viscoelastic flows. The models reviewed can be classified as either multi-relaxation models which couple the viscous stress tensor with slowly decaying quantities to incorporate memory effects (cf. Section 8.2.1), forcing models which incorporate a macroscopic source term to account for viscoelastic stresses (cf. Section 8.2.2), or kinetic models which are a direct discretisation of the Fokker-Planck equation on a lattice (cf. Section 8.2.3). Although all models have demonstrated some success in predicting viscoelastic phenomena, we argue that the forcing strategy for complex fluids has least in common with the lattice Boltzmann philosophy since the additional source term is a macroscopic quantity that requires a finite difference approximation to the Laplacian term. Another severe theoretical limitation to the approach suggested by Grant et al. [27] is the assumption that the viscous and viscoelastic properties have the same relaxation times - a characteristic not observed in Maxwell-type fluids.

The multi-relaxation models for non-Newtonian LBE's proposed by Giraud et al. [13] [14] take advantage of the lattice Boltzmann framework by incorporating viscoelastic effects into the collision operator. This means the characteristic quantities of complex fluids are given purely in terms of lattice moments. Although the numerical verification is limited, the ability to 'tune' the collision matrix gives these models the potential to recover the constitutive equation of choice without having to resort to additional numer-

ical differentiation of macroscopic quantities. This theoretical advantage has yet to be demonstrated correctly in practise and the relation between lattice moments and viscoelastic properties is not well understood at present. The lattice Fokker-Planck models one the other hand have a firm mathematical basis as they are shown to be a direct discretisation of a continuous kinetic equation. Despite being a new and therefore little tested technique, the current numerical evidence to support these models is very encouraging and the algorithm is simple compared to other models for polymeric melts. Therefore, future emphasis in non-Newtonian lattice Boltzmann models is likely to fall on these kinetic models which promise to be a competitive alternative to macroscopic numerical models for polymeric fluids.

Chapter 9

Conclusions and Future Work

The lattice Boltzmann method is a relatively new CFD technique based on the resolution of physics at a mesoscopic level whose governing equations are linear in phase space. It is often promoted as a numerical simulation tool that is particularly suitable for predicting complex flows and this thesis has attempted to justify the above statement.

A common benchmark test in computational fluid dynamics is the flow over a cylinder. A lattice Boltzmann algorithm with advanced boundary condition treatment was written to simulate this well known problem and calculate the drag coefficient, lift coefficient and Strouhal number. The simple case of flow over an unconfined cylinder was used to verify the code and excellent agreement between the lattice Boltzmann prediction and the benchmark value for the drag was observed. The flow over a confined cylinder was then considered and for the first time the influence of the Reynolds number and aspect ratio were systematically studied using the LBE. The three aforementioned characteristics were measured and compared with results recently obtained using a stylised finite volume method. The two data sets were seen to be in close agreement for a large range of Reynolds numbers and aspect ratios. A study of the velocity field clearly showed the onset of von Karman streets in the cylinder wake and a series of mesh refinements demonstrated convergence. A journal article containing this work is currently in preparation [52]. However, a number of our results are somewhat puzzling

and counter-intuitive. In some situations the relative difference is below 1% where as in others it is closer to 5% and at this stage there appears to be no obvious relation between the error and the flow parameters. A possible explanation as to why the error is larger for high Re and high Λ is that the number of degrees of freedom decreases as the aspect ratio increases. Also, the distance between the centre of the cylinder and the outlet (and inlet) was not constant in these simulations but was in those of Sahin [59]. To increase the blockage ratio, we increased the radius of the cylinder while keeping the grid size constant. Therefore, the inflow and outflow conditions may influence the flow differently for different blockage ratios; a problem that does not occur in [59]. We suggest two further studies which may shed some light on the matter. Firstly, the multi-relaxation time LBE, as described in Section 5.4 and in our article [51] can be applied to study this flow and the optimised equation could possibly predict more accurate results for the drag, lift and Strouhal number. More specifically, the generalised model can be used to determine stability requirements and wave vector and streaming velocity dependence of the LBE. Successful 'tuning' of the adjustable parameters can reduce these effects which are likely to influence the flow and higher Reynolds numbers. Secondly, a non-uniform mesh can be constructed and refined in the vicinity of the cylinder. This should capture the flow characteristics in the areas of high gradients and produce more accurate results. Details of mesh refinement techniques for lattice Boltzmann methods can be found in the papers of Bouzidi et al. [4] and Filippova et al. [10]. We note also that the results obtain by Sahin [59], which were used for comparison in this thesis, are themselves approximations for the drag, lift and Strouhal number and are subject to discretisation errors.

In the next project an axisymmetric lattice Boltzmann equation was developed and shown to be a second-order approximation to the axisymmetric Navier-Stokes equations. Unlike previous models this one correctly applies the Chapman-Enskog analysis to LBE and fully exposes the coupling between the two additional source terms through the non-equilibrium contribution to the D2Q9 distribution function, therefore recovering the correct spatial derivatives in the macroscopic limit. These source terms are geo-

metric forces which are consistent with the general form for additional LBE forces as found by Guo et al. [17]. Moreover, the source terms derived here are more local than those of Halliday et al [18] since they are given mainly in terms of moments of the non-equilibrium distribution function. This has the practical advantage of reducing the amount of numerical differentiation which is not only more sympathetic to the general lattice Boltzmann philosophy but is also likely to improve computational efficiency and stability. This last point is as yet unproven but a local stability analysis could be conducted using a Fourier-space formulation (cf Section 5.4). We applied our equation to Stokes' flow over a sphere and found an excellent agreement between the analytical and numerical approximations for the drag coefficient for all $Re < 1$ (i.e when Stokes' law is valid). At higher Reynolds numbers our results agree with an empirical formula for the drag based on experimental evidence. The theoretical development of the model has been published in Physical Review E [55] and a further article on the numerical evaluation of the model is currently in preparation [53]. An extension of this model would be to develop a multi-relaxation time formulation. This could be achieved either by adding the source terms to the right-hand side of equation (5.79), or by defining the moments of the generalised LBE such that the source terms are satisfied. Both procedures would be beneficial as they would enable the stability properties of the axisymmetric LBE to be analysed in detail and allow the model to be extended to non-isothermal flows. However, it should be pointed out that both suggestions could prove problematic since for the first case the dispersion equation may be difficult to obtain in the presence of additional forcing terms, and for the second case the moments for the axisymmetric contributions may be difficult to incorporate into the collision matrix since, at present, they are given in terms of the non-equilibrium part of the distribution. Also, if non-isothermal flows are to be studied a more complicated lattice (with additional velocities) may be needed if all the desired macroscopic properties dictate more than 9 eigenvectors of the collision matrix.

A lattice Boltzmann model for immiscible binary fluids with different viscosities and densities has been developed. In the macroscopic limit this

model was shown to recover the Navier-Stokes equations for two phase flow. This was achieved by constructing an operator that induces the appropriate surface tension term in the macroscopic equations. A theoretical expression for surface tension has been derived from this model and shown to be in excellent agreement with numerical measurements. The model was first used to study Poiseuille flow in a two-dimensional channel for two and three layer configurations of immiscible fluids. Good agreement with the analytical solution was obtained in both cases and a greater accuracy was obtained when the number of lattice nodes in the transverse direction was increased. The three layer configuration maximises the mass flux for a given pressure gradient. Spinodal decomposition of a binary mixtures has been studied. In the case of a mixture of two fluids with the same density but different viscosities the model predicts that, in equilibrium, one large low viscous bubble is surrounded by the more viscous fluid. This prediction agrees with the analysis of Joseph and Renardy [28] who show, using rigorous mathematical arguments, that stable solutions to the equations for rigid motions of two liquids can be framed as a minimisation of energy problem, the only global solution to which is one large sphere. We have also performed simulations to demonstrate that this model can predict binary flows with much larger density ratios than other R-K type LBM's. When the two fluids have different densities, interface stability is maintained by the free parameter, α_r. Large density variation can be obtained provided the bounds on α_r are respected. Both the non-equilibrium rod test and the coalescence of two identical bubbles test were completed successfully and the results have led us to believe that our modified collision operator can capture qualitative and quantitative two-phase flow phenomena. Finally, an axisymmetric multiphase lattice Boltzmann model has been proposed. This model is easy to implement and some test cases have been performed to demonstrate its capabilities. This material has been published in the Journal of Physics A: Mathematical and Theoretical [54]. The most computationally intensive routine in the multi-phase lattice Boltzmann algorithm is the re-colouring step and we have mentioned another of its shortcomings, namely lattice pinning. Other re-colouring procedures have been suggested ([32], [19], [65]) and it

would be interesting to investigate if these alternative routines improve the proposed model. Although this binary fluid LBE, in contrast to others, has been shown to recover the correct form of the Navier-Stokes equation in the macroscopic limit (in a manner consistent with the Chapman-Enskog analysis), it does have a number of limitations, in particular an ideal equation of state and an inability to simulate fluids with very large density ratios. Therefore, another worthwhile study would be to analyse the alternative models reviewed in Chapter 7 to see, as we have done with the R-K model, if it is possible to modify them so that the macroscopic equations are furnished.

A review of the extension of the lattice Boltzmann equation to viscoelasticity has also been presented. The significant steps in the theoretical development of the models have been described and the pros and cons of each highlighted. The state-of-the-art LBE's for non-Newtonian fluids appear to have the potential to offer a promising alternative to traditional continuum-based numerical methods for viscoelasticity, but this is still a contemporary topic and further study is clearly needed if such models are to seriously compete with existing numerical techniques.

Bibliography

[1] D. M. Anderson, G. B. McFadden, and A. A. Wheeler. Diffuse-interface methods in fluid mechanics. *Annu. Rev. Fluid. Mech.*, 30:139–165, 1998.

[2] H.A. Barnes, J.F. Hutton, and K. Walters. *An Introduction to Rheology*. Elsevier Science, Amsterdam, 1989.

[3] R.B. Bird, W.E. Stewart, and E.N. Lightfoot. *Transport Phenomena*. John Wiley, New York, 2002.

[4] M. Bouzidi, D. d'Humières, and L. Luo. Lattice Boltzmann equation on a two dimensional regtangular grid. *J. Comp. Phys*, 172:704–717, 2001.

[5] M. Bouzidi, M. Firdaouss, and P. Lallemand. Momentum transfer of a lattice Boltzmann fluid with boundaries. *Phys. Fluids*, 13:3452–3459, 2001.

[6] H. Chen and X. Shan. Lattice Boltzmann model for simulating flows with multiphase components. *Phys. Rev. E*, 47:1815, 1993.

[7] H. Chen and X. Shan. Simulation of nonideal gases and liquid-gas phase transitions by the lattice Boltzmann equation. *Phys. Rev. E*, 49:2941–2948, 1994.

[8] D. d'Humières, I. Ginzburg, M. Krafczyk, P. Lallemand, and L. Luo. Multiple-relaxation-time lattice Boltzmann models in three dimensions. *Phil. Trans. R. Soc. Lond. A*, 360:437–451, 2001.

[9] F.Higuera, S.Succi, and R.Benzi. Lattice gas dynamics with enhanced collisions. *Euro. Phys. Lett*, 9:345–349, 1989.

[10] O. Filippova and D. Hanel. Grid refinement for lattice-BGK models. *J. Compit. Phys*, 147:218–228, 1998.

[11] B. Fornberg. Steady incompressible flow past a row of circular cylinder. *J. Fluid Mechanics*, 225:655–671, 1991.

[12] U. Frisch, B. Hasslacher, and Y. Pomeau. Lattice gas automata for the Navier-Stokes equations. *Phys. Rev. Lett*, 56:1505–1508, 1986.

[13] L. Giraud, D. d'Humières, and P. Lalleemand. A lattice Boltzmann model for viscoelasticity. *Int. J. Mod. Phys. C*, 8:805–815, 1997.

[14] L. Giraud, D. d'Humières, and P. Lallemand. A lattice Boltzmann method for Jeffreys viscoelastic fluid. *Europhys. Lett*, 42:625–630, 1998.

[15] D. Grunau, S. Chen, and K. Eggert. A lattice Boltzmann model for multiphase fluid flows. *Phys. Fluids. A*, 5:2557–2562, 1993.

[16] A. Gunstensen and D. Rothman. Lattice Boltzmann studies of immiscible two phase flows through porous media. *Phys. Rev. A*, 43:4320, 1991.

[17] Z. Guo, C. Zheng, and B. Shi. Discrete lattice effects on the forcing term in the lattice Boltzmann method. *Phys. Rev. E*, 65:046308, 2002.

[18] I. Halliday, L. A. Hammond, C. M. Care, K. Good, and A. Stevens. Lattice Boltzmann equation hydrodynamics. *Phys. Rev. E*, 64:011208, 2001.

[19] I. Halliday, S.P. Thompson, and C.M Care. Macroscopic surface tension in a lattice Bhatnagar-Gross-Krook model of two immiscible fluids. *Phys. Rev. E*, 57:514–523, 1998.

[20] J. Hardy, O. Pazzis, and Y. Pomeau. Molecular dynamics of a classical lattice gas transport properties and time correlation functions. *Phys. Rev. A*, 13:1949–1961, 1973.

[21] X. He and G. Doolen. Lattice Boltzmann method on curvilinear coordinates: Flow around a circular cylinder. *J. Comput. Phys*, 134:306–315, 1997.

[22] X. He and G. Doolen. Lattice Boltzmann method on curvilinear coordinates: Vortex shedding behind a circular cylinder. *Phys. Rev. E*, 56:434–440, 1997.

[23] F. Higuera and J. Jimenez. Boltzmann approach to lattice gas simulations. *Europhys. Lett*, 9:663–668, 1986.

[24] F. Higuera, S. Succi, and R. Benzi. Lattice gas dynamics with enhanced collisions. *Europhys. Lett*, 9:345–349, 1989.

[25] K. Huang. *Statistical Mechanics*. John Wiley, London, 1965.

[26] T. Inamuro, N. Konishi, and F. Ogino. A Galilean invariant model of the lattice Boltzmann method for multiphase fluid flows using free energy appraoch. *Comp. Phys. Comm*, 129:32–45, 2000.

[27] I. Ispolatov and M. Grant. Lattice Boltzmann method for viscoelastic fluids. *Phys. Rev. E*, 65:056704, 2002.

[28] D.D Joseph and Y.Y Renardy. *Fundamentals of Two-Fluid Dynamics*. Springer-Verlag, New York, 1993.

[29] A.J.C Ladd and R. Verberg. Lattice Boltzmann simulations of particle-fluid suspensions. *Phys. Rev. E*, 64:011208, 2001.

[30] P. Lallemand and L. Luo. Theory of the lattice Boltzmann method: Dispersion, dissipation, isotropy, Galilean invariance, and stabilty. *Phys. Rev. E*, 61:6546–6562, 1999.

[31] H. Lamb. *Hydrodynamics*. Dover Publications, New York, 1945.

[32] M. Latva-Kokko and D.H. Rothman. Diffusion properties of gradient-based lattice Boltzmann models of immiscible fluids. Review copy. Not published at time of writting.

[33] S.V. Lishchuk, C.M. Care, and I. Halliday. Lattice Boltzmann algorithm for surface tension with greatly reduced microcurrents. *Phys. Rev. E*, 67:036701, 2003.

[34] Lord Rayleigh. On the theory of surface forces–II. Compressible fluids. *Phil. Mag.*, 30:209–220, 1892.

[35] L. Luo. Unified theory of lattice Boltzmann models for nonideal gases. *Phys. Rev. Lett*, 81:1618–1621, 1998.

[36] L. Luo. Theory of the lattice Boltzmann method: Lattice Boltzmann models for nonideal gases. *Phys. Rev. E*, 62:4982–4996, 2000.

[37] L. Luo and S.S Girimanji. Theory of the lattice Boltzmann method: Two-fluid model for binary mixtures. *Phys. Rev. E*, 67:036302, 2003.

[38] L. Luo and X. He. Theory of the lattice Boltzmann method: From the Boltzmann equation to the lattice Boltzmann equation. *Phys. Rev. E*, 56:6811–6817, 1997.

[39] L.S. Luo. Lattice gas and lattice Boltzmann methods: past, present and future. In *International Conference on Applied Computational Fluid Dynamics*, 2000.

[40] M.E. McCraken and J. Abraham. Multiple relaxation-time lattice-Boltzmann model for multiphase flow. *Phys. Rev. E*, 71:036701, 2005.

[41] G. McNamara and G. Zanetti. Use of the Boltzmann equation to simulate lattice gas automata. *Phys. Rev. Lett*, 761:2332–2335, 1988.

[42] R. Mei, L-S. Luo, and W. Shyy. An accurate curved boundary treatment in the lattice Boltzmann method. *J. Comput. Phys*, 155:307–330, 1999.

[43] R. Mei and W. Shyy. On the finite difference-based lattice Boltzmann method in curvilinear coordinates. *J. Comput. Phys*, 143:426–448, 1998.

[44] R.R. Nourgaliev, T.N. Dinh, T.G. Theofanous, and D. Joesph. The lattice Boltzmann equation method: Theoretical interpretation, numerics and implications. *Int. J. Multipase Flow*, 29:117–169, 2003.

[45] J. Onishi, Y. Chen, and H. Ohashi. A lattice Boltzmann model for polymeric liquids. *Prog. Comp. Fluid Dynamics*, 5:75–84, 2005.

[46] O. Penrose. *Foundations of Statistical Mechanics: A deductive treatment*. Pergamon Press, London, 1970.

[47] N. Phan-Thien. *Understanding Viscoelasticity*. Springer, Berlin, 2002.

[48] T.N. Phillips and R.G. Owens. *Computational Rheology*. Imperial College Press, London, 2002.

[49] K.N. Premnath and J. Abraham. Lattice Boltzmann model for axisymmetric multiphase flows. *Phys. Rev. E*, 71:056706, 2005.

[50] T. Reis. The lattice Boltzmann method for fluid flow. Master's thesis, University of Wales Aberystwyth, 2003.

[51] T. Reis and T.N. Phillips. An alternative approach to the solution of the dispersion relation of a generalized lattice Boltzmann equation. Submitted to Phys. Rev. E (2007).

[52] T. Reis and T.N. Phillips. A lattice Boltzmann study of flow over a cylinder. In preparation.

[53] T. Reis and T.N. Phillips. Numerical validation of a consistent axisymmetric lattice Boltzmann model. In preparation.

[54] T. Reis and T.N. Phillips. Lattice Boltzmann model for simulating immiscible two-phase flows. *J. Phys. A: Math. Theor*, 40:4033–4053, 2007.

[55] T. Reis and T.N. Phillips. Modified lattice Boltzmann model for axisymmetric flows. *Phys. Rev. E*, 75:056703, 2007.

[56] J.P. Rivet and J.P. Boon. *Lattice Gas Hydrodynamics*. Cambridge University Press, Cambridge, 2001.

[57] D.H Rothman and J.M Keller. Immiscible cellular-automaton fluids. *J. Stat. Phys*, 52:1119–1127, 1988.

[58] D.H. Rothmann and S. Zaleski. *Lattice Gas Cellular Automata. Simple Models of Complex Hydrodynamics*. Cambridge University Press, Cambridge, 1997.

[59] M. Sahin. *A numerical investigation using a novel finite volume method of some flow instabilities*. PhD thesis, École Polytechnique Fédérale De Lausanne, 2004.

[60] K. Sankaranarayanan and S. Sundaresan. Lift force in bubbly suspensions. *Chem. Eng. Sci*, 57:3521–3542, 2002.

[61] S. Succi. *The Lattice Boltzmann Equation for Fluid Dynamics and Beyond*. Oxford University Press, Oxford, 2001.

[62] S. Succi, S. Melchionna, and J.P. Hansen. Lattice Fokker-Planck equation. *Int. J. Mod. Phys. C*, 17:459–470, 2006.

[63] M. Swift, W. Osbourne, and J. Yeomans. Lattice Boltzmann simulations for non-ideal fluids. *Phys. Rev. Lett*, 75:830, 1995.

[64] R.I. Tanner. *Engineering Rheology*. Oxford University Press, Oxford, 2002.

[65] J. Tölke, M. Krafczyk, M. Schulz, and E. Rank. Lattice Boltzmann simulations of binary fluid flow through porous media. *Phil. Trans. R. Soc. Lond. A*, 360:535–545, 2002.

[66] J. D. van der Waals. The thermodynamic theory of capillarity under the hypothesis of a continuous density variation. *Translation in J. Stat. Phys. 20 (1979), 197-244, by J. S. Rowlinson*, 1893.

[67] D.A. Wolf-Gladrow. *Lattice Gas Cellular Automata and Lattice Boltzmann Models - An Introduction*. Springer, Germany, 2000.

[68] S. Wolfram. Cellular automaton fluids 1: Basic theory. *J. Stat. Phys*, 45:471–526, 1986.

[69] A. Xu, G. Gonnella, and A. Lamura. Phase seperation of incompressible binary fluids with lattice Boltzmann methods. *Physica A*, 331:10–22, 2004.

[70] D. Yu, R. Mei, L. Luo, and W. Shyy. Viscous flow computation with the method of lattice Boltzmann equation. *Prog. Aero. Science*, 39:329–367, 2003.

[71] D. Yu, R. Mei, and W. Shyy. A unified boundary treatment in lattice Boltzmann method. *AIAA*, 2003-953:2003, 2003.

[72] P Yuan. *Thermal lattice Boltzmann two-phase flow model for fluid dynamics*. PhD thesis, University of Pittsburgh, 2005.

[73] D. P. Ziegler. Boundary conditions for lattice Boltzmann simulations. *J. Stat. Phys*, 71:1171–1177, 1993.